IN SITU TEM INVESTIGATION OF DEFORMATION AND FRACTURE MECHANISMS OF CERAMICS AND ALLOYS

BY

YANG HU

DISSERTATION

Submitted in partial fulfillment of the requirements
for the degree of Doctor of Philosophy in Materials Science and Engineering
in the Graduate College of the
University of Illinois at Urbana-Champaign, 2017

Urbana, Illinois

Doctoral Committee:

Professor Jian-Min Zuo, Chair, Director of Research
Professor Karin A. Dahmen
Assistant Professor Jessica Anne Krogstad
Assistant Professor Christoph Robert Eduard Maass

ABSTRACT

The mechanical properties of any materials are highly dependent on defects and defect interactions. To improve the mechanical performance and design better materials, it is critical to understand the way defects influence the mechanical properties fundamentally. Transmission electron microscope (TEM) is a powerful tool for the characterization of defects, and thus there is a long history of studying defects using TEM. In situ TEM straining stages were first developed in 1950s, for example, to enable direct observations of dislocations and their interactions with other defects such as twins, grain boundaries (GBs), and materials interfaces. With the recent development of load sensors, in situ TEM mechanical testing combines the power of TEM imaging and diffraction with quantitative load and displacement measurements to provide quantitative understanding of the deformation and fracture mechanisms in various materials. Here, we used in situ TEM to study the deformation and fracture mechanisms of ceramics and alloys.

Firstly, we demonstrated a novel method to evaluate the conditional fracture toughness of thin films and to correlate with in-situ study of fracture mechanisms. Nanocrystalline TiN thin films were investigated using this method. In-situ TEM bright field imaging reveals three crack propagation pathways, namely bridging, intergranular fracture and a mixed mode of transgranular and intergranular fracture. Our methodology is universal and can be applied to other ceramic material systems to evaluate the fracture toughness and study the deformation and failure mechanisms. To further understand the deformation mechanisms of nanocrystalline ceramics, we conducted in situ TEM compression testing on nanocrystalline TiN nanopillars. Grain rotation is

detected during the deformation of nanocrystalline ceramics, which effectively alleviates the lattice strain.

Next, we studied the deformation mechanisms of a new type of alloy, high-entropy alloys (HEAs), with the help of in situ TEM and focused ion beam (FIB) fabrication. The deformation mechanism of HEA nanopillar is revealed by simultaneous measurement of mechanical response and dislocation dynamics. By observing dislocation activities leading to dislocation slip on a single slip plane in HEA nanopillars using in-situ TEM, a series of yielding events are revealed, including activation/deactivation of dislocation sources, intermittent propagation of dislocation arrays, collective dislocation jumps, and finally slip avalanches with large stress drops. The experimentally-obtained stress-dependent slip-size distributions and the spatial properties of the slips in the HEA nanopillars agree with the MFT-model predictions. We obtained a scaling collapse of the slip-avalanche size distributions as function of applied stress and dislocation activities that confirm MFT-scaling predictions and indicate that the applied stress is a critical tuning parameter.

Lastly, we studied the soliton-like dislocation waves in HEA nanopillars. The waves propagate initially smoothly with rise and falls in the wave width, followed by intermittent jumps. We show that the waves were formed by the operation of multiple Frank-Read dislocation sources. The propagation of dislocation waves is accompanied by intermittent bursts of dislocation activities over a large area of the nanopillars. Thus, the correlation study of mesoscopic mechanic testing and nm-scale dislocation imaging here provides unprecedented insights into the less observable

dislocation processes during the quiescent periods between large avalanches and collective dislocation dynamics.

To my mother Yanqing Yang and father Jie Hu.

ACKNOWLEDGEMENTS

First of foremost, I own my deepest appreciation to my advisor, Professor Jian-Min Zuo, for his constant support and encouragement, and for his enthusiasm about science and his challenge to help me grow as a scientist. I am very grateful for his valuable guidance and patience with me when I was exploring for a breakthrough in my research. It has been a privilege for me to work with him during my Ph.D. study at the University of Illinois at Urbana-Champaign.

I would like to thank other members of my thesis committee, Professor Karin Dahmen, Professor Robert Maass and Professor Jessica Krogstad, for their helpful discussions and encouragements during my course of study. I would also like to thank Prof. Jia-Hong Huang from National Tsinghua University for his guidance.

I wish to thank all Zuo's current and past members, Dr. Hefei Hu, Dr. Honggyu Kim, Dr. Wenpei Gao, Dr. Yifei Meng, Dr. Qun Yang, Yu-Tsun Shao, Aram Yoon, Renliang Yuan, Haw-Wen Hsiao and Jocelyn Lai. They helped me in many ways along these years and made my life at this small town enjoyable. I would also like to thank Li Shu, Tommy Song, and Hengyu Zhou for their collaboration. I benefited a lot from interactions and inspiring conversations with them.

Last but not least, I want to express my thankfulness and love to my parents. They have supported me all the time, no matter which direction I chose to go, even when it meant a long separation between them and their only child. I wouldn't be the same without them. My gratefulness also extends to my grandparents, my aunts, my cousin Huimin and all my families.

TABLE OF CONTENTS

CHAPTER 1

INTRODUCTION

The mechanical properties of any materials are highly dependent on defects and defect interactions[1]. To improve the mechanical performance and design better materials, it is critical to understand the way defects influence the mechanical properties fundamentally. Transmission electron microscope (TEM) is a powerful tool for the characterization of defects, and thus there is a long history of studying defects using TEM and defect interactions using in situ TEM. In situ TEM straining stages were first developed in 1950s, for example, to enable direct observations of dislocations and their interactions with other defects such as twins, grain boundaries (GBs), and materials interfaces. With the recent development of load sensors[2], in situ TEM mechanical testing combines the power of TEM imaging and diffraction with quantitative load and displacement measurements to provide quantitative understanding of the deformation and fracture mechanisms in various materials[2-9].

This chapter introduces the motivations for studying the deformation and fracture mechanisms of ceramics and alloys using in situ TEM. The chapter is organized as follows. The first section reviews dislocation plasticity, while the second and third sections review the two material systems studied in this thesis, namely nanocrystalline titanium nitride thin films and high-entropy alloys (HEAs). The fourth section describes the toughness measurement methods of thin

films and the last section discusses the need to study fracture and deformation using in situ TEM and thus the motivation of this thesis.

1.1. Dislocation Plasticity

1.1.1. Deformation of Single Crystals

Under stress, crystalline materials undergo irreversible and plastic deformations. The crystal slips when the resolved shear stress on the incipient slip plane and direction reaches a threshold value called critical resolved shear stress (CRSS). The resolved shear stress τ_{RSS} is related to the geometric relationship between the applied normal stress σ, slip plane normal **n** and slip direction **b**, as shown in Fig. 1.1.

$$\tau_{RSS} = \sigma \cos\lambda \cos\phi = \sigma\mu \qquad (1.1)$$

where λ is the angle between σ and **b**, ϕ is the angle between σ and **n**. The product $\cos\lambda \cos\phi$ is defined as Schmid factor. The slip system with the highest Schmid factor will be activated first. Single slip occurs when only one slip system with the highest Schmid factor is activated, while multiple slip occurs when two or multiple slip systems with similar Schmid factor are activated simultaneously.

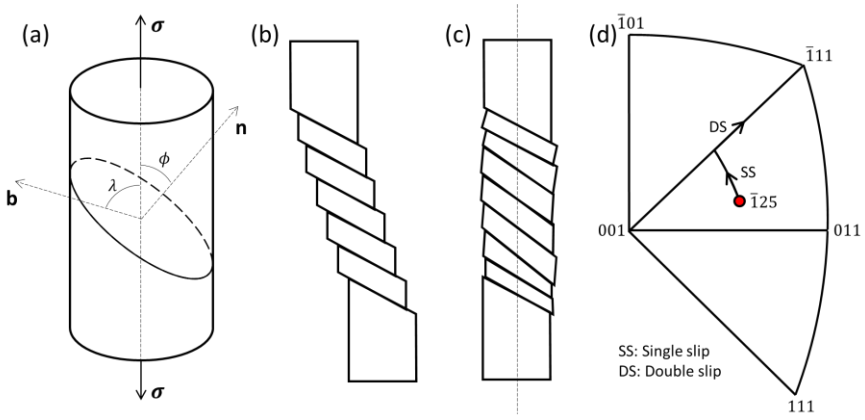

Figure 1.1. *Deformation of single crystal. a) the geometric relationship between loading direction, slip plane and slip direction. b) the crystal free slip without constraint and c) crystal rotation and slip with constraint. d) shows an example of loading axis rotation in tension experiment.*

Mechanical testing on single crystal specimens are usually performed with uniaxial tension or compression. The experiment in general constrains the movement of the two ends of the specimen along the uniaxial loading direction. Thus, the specimen is not able to slip freely [Fig. 1.1(b)], but bends and rotates due to the constraint [Fig. 1.1(c)]. Previous experimental studies [11-13] have shown that the loading axis tends to rotate towards slip direction under tension experiments. Figure 1.1(d) shows the rotation of a face centered cubic (FCC) sample under tension. The starting loading axis of specimen is [-125], which is a single slip direction. As the tension continues, the loading axis gradually rotates towards [-101] slip direction. Double slip begins once the loading axis moves to the connecting line between [001] and [-111] in the pole figure.

1.1.2. Dislocations in Face Centered Cubic Crystal

The deformation of crystalline materials is controlled by dislocations or deformation twinning. Dislocations are line defects, formed by a crystal plane terminating inside the crystal along a line of atoms in the form of an edge dislocation or a shear between two halves of a crystal with the dislocation line marking the end of the shear for a screw dislocation. The Burgers vector **b** of dislocations defines the magnitude and direction of slip direction. The Burgers vector of edge dislocations is normal to dislocation line, while a screw dislocations' Burgers vector is parallel to the dislocation line. However, in most cases, dislocation lines are rarely straight and curved dislocations have both screw and edge components, which are called mixed dislocations. Edge dislocations can move by gliding and climbing. The dislocation glide is the motion of dislocation on its slip plane. When a single dislocation glide through the entire slip plane, the crystal slips by one magnitude of its Burgers vector. Both edge and screw dislocations move in planes parallel to their Burgers vector. This means an edge dislocation moves in directions parallel to **b** and screw dislocations move in directions perpendicular to **b**. At high temperatures when atomic diffusion is promoted, edge dislocations are able to climb. Dislocation climb is realized by atoms on the dislocation line diffusing away, or when surrounding atoms diffuse to the dislocation core, resulting a shrinkage or expansion of the extra half plane of edge dislocations. On the other hand, screw dislocations cannot climb since there is no extra half plane, but it can glide and cross-slip. For example, when a screw dislocation meets an obstacle on its original slip plane, it can cross-

slip to an intersecting slip plane and continue to propagate. Cross-slip is an important mechanism for dislocations to overcome barriers to their motions.

In FCC crystals, a perfect dislocation can dissociate into two partial dislocations, for example, $\frac{1}{2}[10\bar{1}] \rightarrow \frac{1}{6}[2\overline{11}] + \frac{1}{6}[11\bar{2}]$, which is energetically favorable. This dissociation creates a faulted region bounded by two partial dislocations, called stacking fault. There is an equilibrium width of the stacking fault, which is determined by the stacking fault energy. The dissociation of dislocations has a marked effect on the cross-slip behaviors. The two dissociated partial dislocations need to recombine into a perfect dislocation in order to cross-slip. If the stacking fault energy is low, then the separation of partial dislocations is large and cross-slip is less likely to happen.

Homogeneous nucleation of dislocations requires large stresses at about one tenth of the shear modulus. The generation of dislocations during plastic deformation, however, occurs at much lower stresses. This is achieved by an elongation of the length of dislocations. The common mechanisms is dislocation multiplication by Frank-Read sources, single arm sources inside crystals (which is observed in thin samples used in TEM) and the double-cross slip mechanism suggested by Koehler[14] rand Orowan[15]. The operation of Frank-Read (FR) source is shown in Fig. 1.2. FR source is formed by a dislocation pinned at two ends, P and P'. The middle dislocation line bows out when a stress is applied on the slip plane. Under stress τ, the dislocation will assume a certain diameter $l = Gb/\tau$. From this equation, the maximum stress is needed when

l is minimum, corresponding to a semicircle dislocation line. Once the stress reaches the maximum stress, the FR source will continue operating. When the loop reaches the configuration shown in Fig. 1.2(c), the dislocation segments m and n will meet and annihilate with each other due to opposite Burgers vector. Then the process repeats itself and generate multiple dislocation loops. If the front dislocation is stopped due to obstacles, the back stress exerted by the front dislocation will cease the operation of FR source. If the dislocation is not pinned at two ends but at only one ends, single arm dislocation source is formed (Fig. 1.3). Under shear stress, the mobile dislocation line will rotate around the pinning point. Once the dislocation line swipes the entire slip plane, a slip step with magnitude of Burgers vector is generated.

Double-cross slip is another dislocation generation mechanism. Its operation is shown in Fig. 1.4. The screw dislocation first glide on the slip plane until it meets obstacles impeding its motion. Then it cross slips to an intersecting slip planes and cross slips again to a plane parallel to the original slip plane to overcome the obstacle. The cross slipped segment is of length L results in two superjogs (green lines in Fig. 1.4(b)) which are immobile and act as pinning sites for segment L and the non-cross slipped segment. The segments start to multiplicated similar to Frank-Read source. In Fig. 1.4(c), the segments can pass each other only when the height of the superjogs h is larger than a critical value $h_c = \frac{\mu b}{8\pi(1-\nu)\tau}$, which is called dipole opening criterion. The ν is Poisson's ratio. Since the generated dislocation moves on a parallel plane, the slip will spread into a band, called slip band. If the height of superjog is smaller than the critical value, it will form

dislocation dipoles as shown in Fig. 1.4(d). Higher stresses are required to open the dislocation dipole.

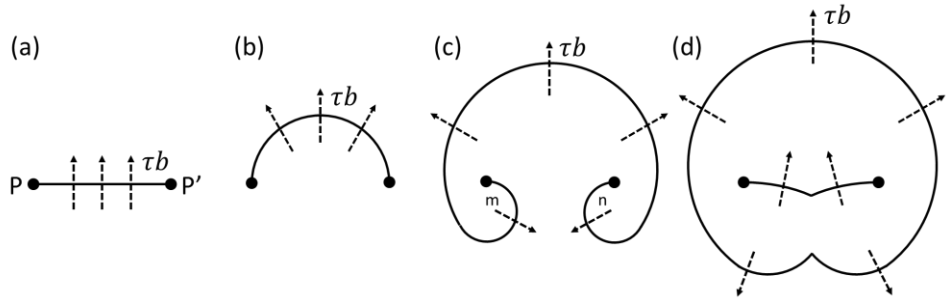

Figure 1.2. *The operation of Frank-Read dislocation source. P and P' are pinning points and PP' line is mobile dislocation line. Under shear stress* τb*, the dislocation line bows out and generates dislocation loops.*

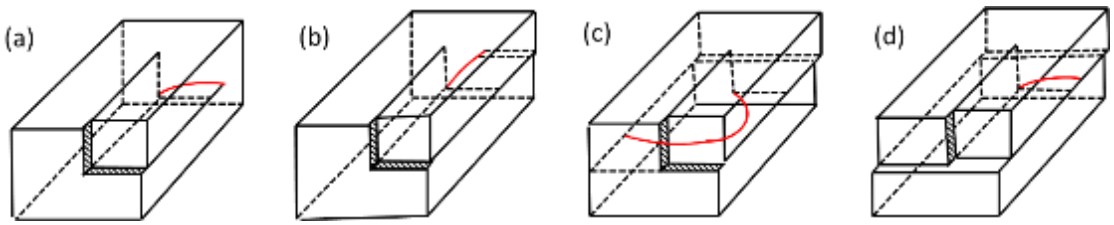

Figure 1.3. *The operation of single arm dislocation source. The red line shows the spiral motion of dislocation line.*

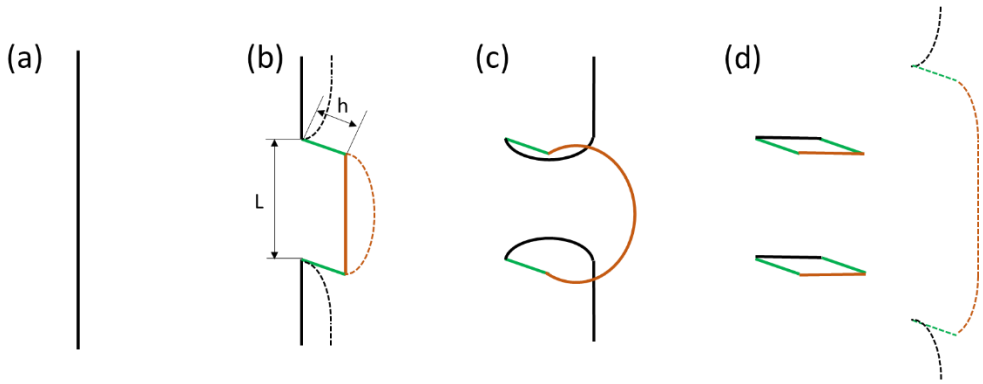

Figure 1.4. *Double-cross slip mechanism for dislocation generation[16].*

1.1.3. Dislocation Pinning Mechanisms

Dislocations interact with each other through dislocation intersections, reactions and long-range stress field. Dislocations also interact with extrinsic obstacles, including vacancies, solute atoms, precipitates and grain boundaries. These interactions always immobilize the motion of dislocations, which is called dislocation pinning.

As the dislocation density increases during deformation, dislocations entangle with each other and forms immobile dislocation structure. Figure 1.5 shows three important mechanisms for dislocation entanglement. If there are multiple dislocations on the same slip plane with same Burgers vector, once the dislocation at the head stopped by certain types of barriers, it exerts a back stress to oppose the motion of following dislocations. This often leads to dislocation pile-up against obstacles. When dislocations gliding on different slip planes encounter each other, they will intersect and produce a kink or jog. Since the dislocation kink remains in the slip plane, it can still move with dislocation. However, the motion of dislocation jog, which does not lie on the previous slip plane, may only move by dislocation climb. If the temperature is not high enough to allow significant atomic diffusion, the jog will be immobile and motion of the rest dislocation segments is impeded. Furthermore, dislocations can react with each other to produce sessile dislocations not residing on slip planes. For example, in FCC crystals, the most-widely observed sessile dislocation are Lomer-Cottrell lock. Two pairs of partial dislocations attract each other and move toward the intersection line between two slip planes. The two partial dislocations in the front

react $\frac{1}{6}[\bar{1}2\bar{1}] + \frac{1}{6}[1\bar{1}2] \rightarrow \frac{1}{6}[011]$. The production of reaction is a dislocation with Burgers vector $\frac{1}{6}[011]$ on plane (100), which are not allowable slip direction and plane in FCC crystals. Therefore, it is a sessile dislocation and the motion of additional dislocations are hindered by this sessile dislocation.

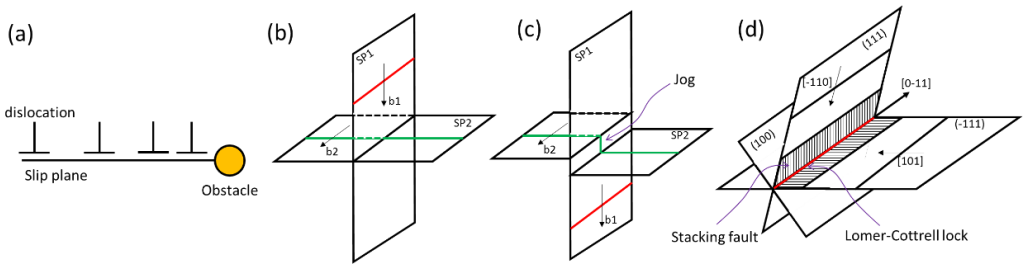

Figure 1.5. *Dislocation pinning mechanisms. a) shows the back stress between dislocations causing dislocation pile-up against obstacles. b) and c) show the intersection of dislocation which forms immobile jogs. d) shows the structure of Lomer-Cottrell lock.*

Moreover, point defects, including solute atoms and vacancies, can interact with dislocations through their elastic field. Solute atoms and vacancies tend to concentrate at the dislocation core area to reduce lattice distortion. Due to its low-energy configuration, dislocations are difficult to detach from these pinning centers. Solute atoms can also segregate to the stacking faults contained by two partial dislocations. The segregation lowers the stacking fault energy and increases the width of stacking fault. To cross-slip to an intersecting slip plane, two partial dislocations need to combine into a perfect dislocation. However, the wide-separated partial dislocations make the combination difficult and thus higher stress is required to constrict the pair of partial dislocations. Solute atoms also have tendency to arrange themselves into short-range ordering or clustering.

Dislocation pinning occurs because the movement of dislocation through short-range ordering will reduce the degree of local order, thus increase the energy. Once the stress is high enough the destruct the short-range ordering, it creates a clean path for dislocation to glide. This constrains dislocation movement onto one single slip plane, which is called planar slip behavior.

Other dislocation pinning mechanisms that operate in polycrystals and alloys arise from interactions with grain boundaries and secondary phases such as precipitates. The grain boundaries impede the motion of dislocations and, thus, harden the materials. Within one grain, microscopic yielding can occur and dislocation will pile-up against the grain boundary. The pile-up generates high stresses and initiate the plastic yielding in adjacent grains by emitting dislocations from grain boundary or dislocation nucleation within adjacent grains. The obstruction of dislocations by grain boundary leads to the Hall-Petch relationship $\sigma_y = \sigma_0 + k_y d^{-\frac{1}{2}}$, where σ_y is the yield strength, σ_0 is the intrinsic resistance stress to dislocation motion, k_y is a Hall-Petch coefficient, and d is the grain size. Thus, smaller grain size is preferred to achieve high strength. For example, the yield strength of nanocrystalline materials is greater than that of their large grain size polycrystalline counterparts. Second phases such as precipitates particles can also strengthen the materials. If the precipitate lattice is coherent with the matrix lattice, the difference in the lattice constant leads to an internal lattice strain field, which will interact with dislocations and result in an increase in the yield strength. Further, the formation of precipitates within matrix introduces an interface energy. If a dislocation cuts through the precipitate, the interface energy increases. The cut-through of

dislocation also reshuffles the bonding within the precipitate and increase the bonding energy. As a result, dislocation cannot easily cut through the precipitates without higher driving force.

1.1.4. Work Hardening of Single Crystal

The plastic deformation of metals is characterized by the fact that increased stress is often required to further the deformation. The increase in the required deformation stress as a function of strain is called work hardening, or strain hardening. The ratio between the shear stress increase $d\tau$ and the shear strain increase $d\gamma$ is defined as strain hardening rate (SHR). Strain hardening is caused by dislocations interacting with each other or with obstacles. In a single crystalline specimen at a low symmetry orientation, the deformation is usually divided into three regimes, or stages, based on the difference in SHR. A schematic of three stages in stress-strain curve is shown in Fig. 1.6.

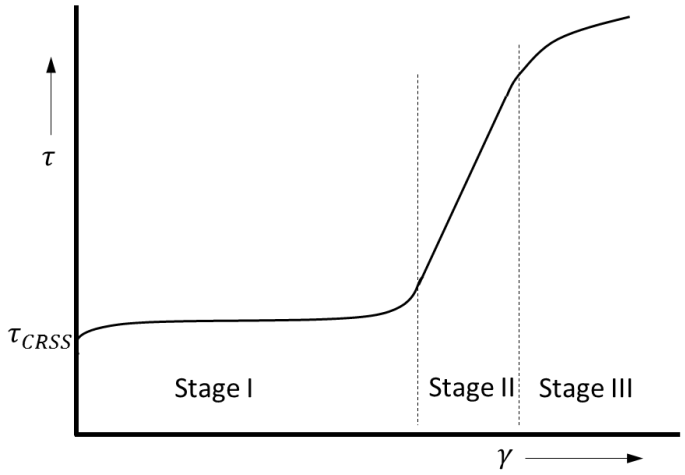

Figure 1.6. *Schematic of shear stress-strain curve of a single-slip oriented single crystal.*

Stage I, the region of easy glide, is characterized by small SHR. The SHR is ~10^{-4} G, where G is the shear modulus. In this stage, dislocations glide on the preferential slip plane with little opposing stress. The crystal slip changes the loading axis of specimen due to the constraint at two ends. When the sample reaches the double slip orientation, the SHR increases rapidly, which is called stage II. In stage II, the stress increases linearly with strain. The SHR is ~3×10^{-3} G. Since the motion of dislocations is not confined to one slip plane, dislocations on intersecting slip planes will intersect with each other and produce immobile junctions, such Lomer-Cottrell lock and jogs. These junctions act as strong barriers for following dislocations to pass through. Therefore, dislocations are stored in the specimen, resulting an increase in dislocation density. An empirical relationship between work hardening and dislocation density was proposed by Taylor[17], which relates the flow stress with the dislocation density by

$$\tau = \tau_0 + \alpha G b \rho^{1/2} \qquad (1.2)$$

where τ_0 is the shear stress required to move a dislocation without the influence of other dislocations and α is the constant. For FCC and BCC metals, α varies from 0.3 to 0.6. Stage III is a region of decreasing rate of strain hardening. In this region, the stress is high enough to allow dislocation to cross-slip obstacles and release the internal stress accumulated in stage II.

1.2. Nanocrystalline Materials and TiN Thin Films

Nanocrystalline materials is a type of materials whose grain size ranges from ~1 nm to few hundreds nm. Due to the small grain sizes, nanocrystalline materials have a large volume fraction of grain boundaries (GBs), which greatly influence their mechanical properties. Based on dislocation interactions with grain boundaries, Hall-Petch relationship dictates that the yield strength of materials is inversely proportional to the grain size. This has been the incentive for research in the nanocrystalline materials in the pursuit of high strength[1, 18-29]. However, nanocrystalline materials show low ductility at room temperature[18, 30-32], which limits their applications. In nanocrystalline metals that fail by brittle fracture, the fracture surface is characterized with dimpled structures whose sizes are larger than the grain size. Hasnaoui et al.[32] used molecular dynamics to simulate the fracture process of nanocrystalline nickel and their results suggested that the formation of local shear planes contributed to the dimpled characteristics on the fracture planes. Shan et al.[30] conducted in-situ tensile straining on nanocrystalline nickel in a TEM. Grain agglomerates were found to form rapidly and frequently ahead of an advancing crack, which was used to explain the formation of dimpled structure. Compared with nanocrystalline metals[33], the fracture mechanisms of nanocrystalline ceramics are less studied. In nanocrystalline ceramics consist of a large portion of GB atoms, it has been proposed that the mechanical properties and fracture mechanisms of nanocrystalline ceramics are mainly determined by the amorphous and soft GB phases. GBs act as a preferable place for crack nucleation and

propagation, because of their low atomic density and weak interatomic bonds. Ovid'Ko et al.[34-37] constructed theoretical models to study the deformation and fracture mechanisms of nanocrystalline ceramics. Their models suggested that stress-induced GB sliding and migration serve as the toughening mechanisms. Pozdnyakov and Glezer[38] theoretically examined the fracture toughness of a quasi-brittle nanomaterial and concluded that plastic deformation carried by GBs can significantly increase the fracture toughness of nanocrystalline ceramics. However, so far, there is a lack of experimental evidences on how GBs contribute to the fracture dynamics, and what GB-mitigated deformation mechanisms are behind nanocrystalline ceramics.

The deformation mechanisms of nanocrystalline materials are the subject of debate. The plastic deformation of materials of coarse grains is dominated by dislocation activities. However, dislocation activities are inhibited in nanocrystalline materials due to the limited grain size and large volume fraction of GBs. Thus, GB-mitigated deformation mechanisms have been suggested to play an important role in the nanocrystalline materials. This viewpoint has been forwarded based on molecular dynamics (MD) simulation results[24], however, so far there is no concrete experimental evidence to support this.

In this thesis, TiN thin films are selected as model of nanocrystalline ceramics. Nanocrystalline TiN thin films have high hardness, high thermal and chemical stability, high electrical conductivity, and high biocompatibility. The current and potential applications of TiN thin films include hard and corrosion protective coatings on mechanical tools and prosthetic

devices, anti-erosion coatings on aerospace components, conducting coatings on counter electrode of flexible dye-sensitized solar cell[39], and diffusion barriers in microelectronic components. Understanding the fracture and deformation mechanisms will greatly benefit these applications by providing fundamental knowledge of deformation process.

1.3. High-Entropy Alloys

High-entropy alloys (HEAs) are new materials that have attracted considerable interest due to their exceptional thermomechanical properties[40], especially high temperature stability[41, 42]. HEAs have relatively simple crystallographic structure, e.g. face-centered cubic (FCC)[43-45], body-centered cubic (BCC)[46-48] or hexagonal close-packed (HCP)[49-51]. Compared to conventional alloys based on a single principal component, such as Fe in steels, HEAs are composed of four or more elements of equal or near-equal molar percentage in random solution[52, 53]. Because of this, it is characterized by a high configuration entropy. The high entropy significantly reduces the Gibbs free energy at high temperatures and thus contributes to the stability of random solid solution. The atomic structure of HEAs differs from simple metals, because of the varying sizes of the constitutive elements in HEAs and thus the inevitable atomic scale lattice distortion[54]. The lattice distortion greatly influences atomic diffusion[55], creep resistance[56] and mechanical properties, including high strength and hardness[57], good wear resistance and fatigue behavior[58], and high fracture resistance at cryogenic temperatures[59].

Figure 1.7 shows the comparison of yield strength and fracture toughness of HEAs with other structural materials. These characteristics make HEAs as potential materials for various applications, such as thermal barrier coatings[60], hard facing applications[61], antibacterial coating[52], high temperature structural materials[62] and aerospace materials[63].

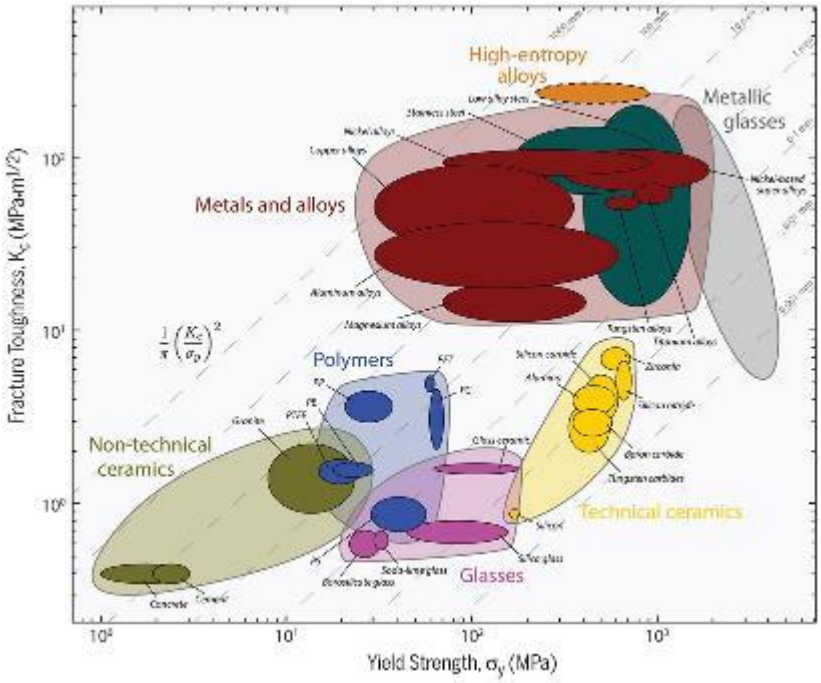

Figure 1.7. *Ashby map showing the comparison of fracture toughness and yield strength of HEAs with other material systems[59].*

However, HEAs exhibit complex, and unexplained, mechanical behaviors. In certain temperature and strain-rate regime, HEAs deform via sudden slips that are visible as stress drops or "serrations" in the stress-strain curve (see Fig. 1.8). Caroll et al.[64] presented a series of tensile deformation experiments performed at slow strain-rates on metals including both conventional alloys and HEAs. The serration phenomena are found in medium-entropy alloys (CoFeNi and

CoCrFeNi) and HEA (CoCrFeMnNi), not in low-entropy alloys (Ni and CoNi). An analysis of the observed serration statistics is consistent with simple coarse grained mean field theory (MFT) model[65] that weak spots, which slip along slip planes (when a sufficiently-large shear stress is applied) trigger other weak spots to slip, resulting in slip avalanches typically detected as sudden stress drops. During slip avalanches, the participating weak spots are weakened from their original strength to a lower strength, but they are re-strengthened during the time intervals between slip avalanches. Re-strengthening or healing of weak spots between slip avalanches is temperature-, strain-rate-, and composition-dependent. However, the underlying deformation mechanisms responsible for the observed serrations are unclear.

Initial reports on deformation mechanisms of HEAs have provided different pictures with some suggesting a similar deformation processes as the conventional alloys based on the planar dislocation gliding on the normal FCC slip systems[66, 67], others suggesting behaviors more like nanostructured metals involving nanoscale deformation twinning[68]. Zaddach et al.[69] reported that HEAs have low stacking fault energy (SFE) 20-25 mJ/m^2. The low SFE contributes to the planar slip behaviors by constraining the cross-slip of dislocations. Xu et al.[70] reported nanoscale $L1_2$ ordering phase in $Al_{0.5}$CoCrCuFeNi HEA. The short-range ordering phase in HEAs impedes the dislocation motion. When the applied stress is high enough to allow one dislocation cutting through the short-range ordering phase, it provides an easy path for other dislocations and thus leads to planar slip by confining dislocations gliding on one slip plane. Additionally, the low SFE

also contributes to the deformation twinning observed at low temperature[59, 67]. The deformation twinning considerably increase the fracture toughness of HEAs at cryogenic temperature[59]. Recently, a transformation-induced plasticity dual phase HEA (TRIP DP HEA)[71] was fabricated which breaks the trade-off between strength and ductility by increasing the tensile strength to ~900 MPa and elongation to ~80%. The mastensitic transformation from FCC phase to HCP phase in combination with deformation twinning, grain boundary strengthing and solute solution strengthing significantly increases the work hardening capacity and strength of TRIP DP HEAs. However, all the present studies on deformation mechanism of HEAs employed ex-situ characterization methods or in-situ TEM straining experiments[72], which can hardly be directly correlated with the mechanical response.

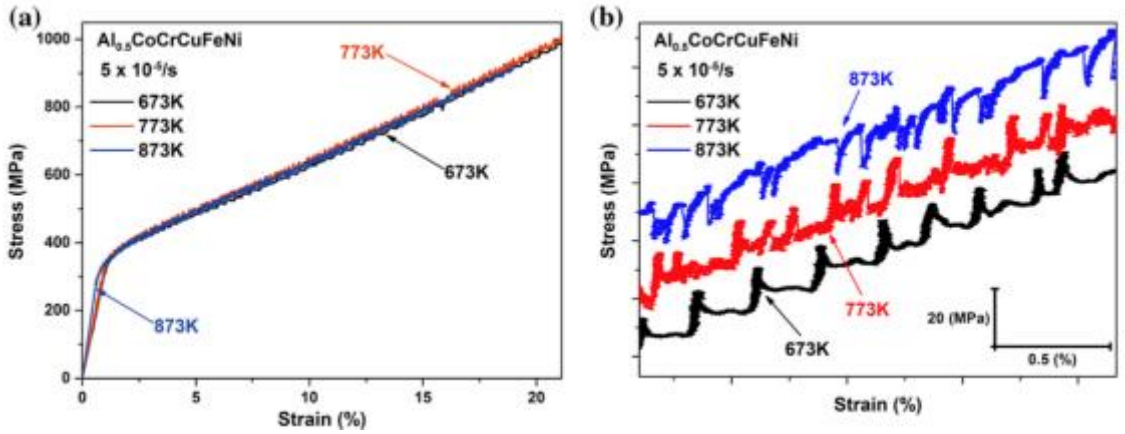

Figure 1.8. *a) Stress strain curve of $Al_{0.5}$CoCrCuFeNi HEA at different temperatures. b) a magnified view to better show the serration behaviors[73].*

1.4. Toughness Measurement of Thin Films

Materials fail by fracture. Fracture toughness in general serves as an important indicator of the reliability of structural materials. For bulk materials, the method to measure fracture toughness is well-established by following the standard ASTM procedures for three point bending test. However, these methods are not compatible with in-situ monitoring of microstructure using TEM, which requires a thin film. There has also been a lack of a universal methodology to measure the fracture toughness of thin films. Numerous techniques were applied to evaluate the fracture toughness of thin films, including indentation[74], tension[75, 76], and buckling[77, 78]. Those measurement methods for fracture toughness rely on testing thin films deposited on metallic or Si substrates. Because of substrate effect and difficulties in fabricating specimens and applying external stress, there are considerable uncertainties in the measured values[79], and the origin of these variations may be also due to different deformation and failure mechanisms of thin films. Recently, bending experiment performed in a scanning electron microscope (SEM)[80-82] avoids the subtrate effect, but the deformation and fracture mechanism were not identified. Therefore, it is necessary to measure the fracture toughness and investigate the accompanying deformation and failure mechanisms in thin film using TEMs.

1.5. Objectives

This thesis consists of two parts. In the first part of this thesis, we present the investigation of fracture and deformation mechanisms of nanocrystalline TiN films with help of in situ TEM mechanical testing and focused ion beam (FIB) sample fabrication. In the second part of this thesis, we present the investigation of deformation mechanisms of high-entropy alloys (HEAs) based on in situ TEM compression experiments.

Nanocrystalline TiN thin films were selected for study because there are few reports on the fracture and deformation mechanisms of nanocrystalline ceramics. It has been proposed that the mechanical properties and fracture mechanisms of nanocrystalline ceramics are mainly determined by the amorphous and soft GB phases. However, so far, there is a lack of experimental evidences on how GBs contribute to the fracture dynamics, and what GB-mitigated deformation mechanisms are behind nanocrystalline ceramics. TiN thin-film coatings are used in hard and corrosion protective coatings on mechanical tools and prosthetic devices, anti-erosion coatings on aerospace components, where fracture toughness is one of the most crucial properties[79, 83].

The second part of this thesis is to address the following major questions associated with HEAs using the $Al_{0.1}CoCrFeNi$ HEA of fcc structure for model study.

1) How does the microstructure of HEA affect dislocation activities?

The atomic structure of HEAs differs from simple metals, because of the varying sizes of the constitutive elements in HEAs. The unique lattice structure of HEA is expected to affect dislocation behaviors.

2) What is the origin of serration in the stress-strain curve of HEAs?

The origin of the observed sudden slips (“serrations”) in the stress-strain curve[40, 64] is unexplained. The sudden stress drops represent plastic instabilities. Plastic instabilities are observed in other alloys as well. They are detrimental to structural applications. In general, plastic instabilities are poorly understood. It is thus crucial to understand the serration behavior for better deformation control.

3) What are the work hardening mechanisms in HEAs?

Work hardening is a difficult problem that has puzzled metallurgists for centuries[84]. Significant efforts, iincluding both experimental and theoretical work, have been devoted to understand and predict the strain hardening behaviors of materials. The challenge is to link atomic scale interactions with nm scale dislocation dynamics over mesoscopic or macroscopic volumes where mechanical tests are performed. While significant progress has been made in the study of dislocations. Attempts to link dislocation dynamics with mechanic properties using Dislocation dynamics (DD) modeling, in principle, can bridge the gap. However, the modeling requires detailed atomistic and dislocation mechanisms of strain hardening, which are often missing. The

development of dislocation microstructure observed by ex situ TEM[85, 86] is critical to work hardening, however, the dynamics of their formation is still missing. Through the development of in situ TEM mechanical tests, it is possible to close the gap between experimental and computational studies of work hardening quantitatively.

1.6. Organization

The next chapter introduces the basic concepts of diffraction contrast imaging, scanning electron nanobeam diffraction (SEND), in situ TEM mechanical testing and focused ion beam (FIB) sample preparation procedure. Chapter 3 and 4 are focused on in situ TEM mechanical testing of nanocrystalline titanium nitride thin films. A novel and universal toughness measurement method is presented in Ch. 3 with the ability to measure the intrinsic fracture toughness and identify the toughening mechanisms. Chapter 4 studies the grain rotation behaviors of nanocrystalline TiN with the help of SEND and in situ diffraction. Chapter 5, 6, and 7 focus on the deformation mechanisms of HEAs. In chapter 5, we present the results on characterization of the structure of HEA and in situ dislocation imaging during deformation. Systematic experimental work was conducted to determine the best imaging condition for dislocations during in situ TEM. A series of yielding events are revealed, including activation/deactivation of dislocation sources, intermittent propagation of dislocation arrays, collective dislocation jumps, and finally slip avalanches with large stress drops. In chapter 6, a mean field theory model is applied to study the serration behaviors of HEA nanopillar, the results of which are correlated with dislocation

dynamics, providing new insights into the serration mechanism. Work hardening results of HEAs are reported in chapter 7 and conclusions and future research directions are reached in chapter 8.

1.7. References

[1] J. Schiotz, F.D. Di Tolla, K.W. Jacobsen, Softening of nanocrystalline metals at very small grain sizes, Nature 391(6667) (1998) 561-563.

[2] E.A. Stach, T. Freeman, A.M. Minor, D.K. Owen, J. Cumings, M.A. Wall, T. Chraska, R. Hull, J.W. Morris, A. Zettl, U. Dahmen, Development of a nanoindenter for in situ transmission electron microscopy, Microsc Microanal 7(6) (2001) 507-517.

[3] D. Kiener, P. Hosemann, S.A. Maloy, A.M. Minor, In situ nanocompression testing of irradiated copper, Nat Mater 10(8) (2011) 608-613.

[4] D. Kiener, A.M. Minor, Source-controlled yield and hardening of Cu(100) studied by in situ transmission electron microscopy, Acta Mater 59(4) (2011) 1328-1337.

[5] A.M. Minor, S.A.S. Asif, Z.W. Shan, E.A. Stach, E. Cyrankowski, T.J. Wyrobek, O.L. Warren, A new view of the onset of plasticity during the nanoindentation of aluminium, Nat Mater 5(9) (2006) 697-702.

[6] A.M. Minor, E.T. Lilleodden, E.A. Stach, J.W. Morris, In-situ transmission electron microscopy study of the nanoindentation behavior of Al, J Electron Mater 31(10) (2002) 958-964.

[7] A.M. Minor, J.W. Morris, E.A. Stach, Quantitative in situ nanoindentation in an electron microscope, Appl Phys Lett 79(11) (2001) 1625-1627.

[8] Z.W. Shan, G. Adesso, A. Cabot, M.P. Sherburne, S.A.S. Asif, O.L. Warren, D.C. Chrzan, A.M. Minor, A.P. Alivisatos, Ultrahigh stress and strain in hierarchically structured hollow nanoparticles, Nat Mater 7(12) (2008) 947-952.

[9] Z.W. Shan, R.K. Mishra, S.A.S. Asif, O.L. Warren, A.M. Minor, Mechanical annealing and source-limited deformation in submicrometre-diameter Ni crystals, Nat Mater 7(2) (2008) 115-119.

[10] R. Maass, In-situ Laue diffraction on deforming micropillars, (2009).

[11] G. Taylor, The distortion of crystals of aluminium under compression. Part II. Distortion by double slipping and changes in orientation of crystal axes during compression, Proceedings of the Royal Society of London A: Mathematical, Physical and Engineering Sciences, The Royal Society, 1927, pp. 16-38.

[12] G. Taylor, W. Farren, The distortion of crystals of aluminium under compression. Part I, Proceedings of the Royal Society of London. Series A, Containing Papers of a Mathematical and Physical Character 111(759) (1926) 529-551.

[13] G. Taylor, The Distortion of Crystals of Aluminium under Compression. Part III. Measurements of Stress, Proceedings of the Royal Society of London A: Mathematical, Physical and Engineering Sciences, The Royal Society, 1927, pp. 39-60.

[14] J.S. Koehler, The Nature of Work-Hardening, Phys Rev 86(1) (1952) 52-59.

[15] M. Cohen, American Institute of Mining and Metallurgical Engineers. Institute of Metals Division., Dislocations in metals, Institute of Metals Division, American Institute of Mining and Metallurgical Engineers, New York,, 1954.

[16] U. Messerschmidt, M. Bartsch, Generation of dislocations during plastic deformation, Mater Chem Phys 81(2-3) (2003) 518-523.

[17] G.I. Taylor, Plastic Strain in Metals, Journal of the Institute of Metals 62 (1938) 307-324.

[18] M.A. Meyers, A. Mishra, D.J. Benson, Mechanical properties of nanocrystalline materials, Prog Mater Sci 51(4) (2006) 427-556.

[19] H. Gleiter, NANOCRYSTALLINE MATERIALS, Prog Mater Sci 33(4) (1989) 223-315.

[20] K.S. Kumar, H. Van Swygenhoven, S. Suresh, Mechanical behavior of nanocrystalline metals and alloys, Acta Mater 51(19) (2003) 5743-5774.

[21] C. Suryanarayana, NANOCRYSTALLINE MATERIALS, International Materials Reviews 40(2) (1995) 41-64.

[22] M.W. Chen, E. Ma, K.J. Hemker, H.W. Sheng, Y.M. Wang, X.M. Cheng, Deformation twinning in nanocrystalline aluminum, Science 300(5623) (2003) 1275-1277.

[23] J. Schiotz, K.W. Jacobsen, A maximum in the strength of nanocrystalline copper, Science 301(5638) (2003) 1357-1359.

[24] I.W. Chen, X.H. Wang, Sintering dense nanocrystalline ceramics without final-stage grain growth, Nature 404(6774) (2000) 168-171.

[25] M. Dao, L. Lu, R.J. Asaro, J.T.M. De Hosson, E. Ma, Toward a quantitative understanding of mechanical behavior of nanocrystalline metals, Acta Mater 55(12) (2007) 4041-4065.

[26] S.C. Tjong, H. Chen, Nanocrystalline materials and coatings, Materials Science & Engineering R-Reports 45(1-2) (2004) 1-88.

[27] E.M. Bringa, A. Caro, Y.M. Wang, M. Victoria, J.M. McNaney, B.A. Remington, R.F. Smith, B.R. Torralva, H. Van Swygenhoven, Ultrahigh strength in nanocrystalline materials under shock loading, Science 309(5742) (2005) 1838-1841.

[28] L. Lu, M.L. Sui, K. Lu, Superplastic extensibility of nanocrystalline copper at room temperature, Science 287(5457) (2000) 1463-1466.

[29] Y. Wang, M. Chen, F. Zhou, E. Ma, High tensile ductility in a nanostructured metal, Nature 419(6910) (2002) 912-915.

[30] Z. Shan, J.A. Knapp, D.M. Follstaedt, E.A. Stach, J.M.K. Wiezorek, S.X. Mao, Inter- and intra-agglomerate fracture in nanocrystalline nickel, Physical Review Letters 100(10) (2008).

[31] D. Farkas, H. Van Swygenhoven, P.M. Derlet, Intergranular fracture in nanocrystalline metals, Physical Review B 66(6) (2002).

[32] A. Hasnaoui, H. Van Swygenhoven, P.M. Derlet, Dimples on nanocrystalline fracture surfaces as evidence for shear plane formation, Science 300(5625) (2003) 1550-1552.

[33] I. Szlufarska, A. Nakano, P. Vashishta, A crossover in the mechanical response of nanocrystalline ceramics, Science 309(5736) (2005) 911-914.

[34] I.A. Ovid'ko, A.G. Sheinerman, Special strain hardening mechanism and nanocrack generation in nanocrystalline materials, Appl Phys Lett 90(17) (2007).

[35] I.A. Ovid'ko, A.G. Sheinerman, Nanocrack generation at dislocation-disclination configurations in nanocrystalline metals and ceramics, Physical Review B 77(5) (2008).

[36] I.A. Ovid'ko, A.G. Sheinerman, E.C. Aifantis, Effect of cooperative grain boundary sliding and migration on crack growth in nanocrystalline solids, Acta Mater 59(12) (2011) 5023-5031.

[37] I.A. Ovid'ko, A.G. Sheinerman, E.C. Alfantis, Stress-driven migration of grain boundaries and fracture processes in nanocrystalline ceramics and metals, Acta Mater 56(12) (2008) 2718-2727.

[38] V.A. Pozdnyakov, A.M. Glezer, Structural mechanisms of plastic deformation in nanocrystalline materials, Phys Solid State+ 44(4) (2002) 732-737.

[39] P. Chen, W.-Y. Wu, The use of sputter deposited TiN thin film as a surface conducting layer on the counter electrode of flexible plastic dye-sensitized solar cells, Surface and Coatings Technology 231 (2013) 140-143.

[40] Y. Zhang, T.T. Zuo, Z. Tang, M.C. Gao, K.A. Dahmen, P.K. Liaw, Z.P. Lu, Microstructures and properties of high-entropy alloys, Prog Mater Sci 61 (2014) 1-93.

[41] O.N. Senkov, G.B. Wilks, J.M. Scott, D.B. Miracle, Mechanical properties of Nb25Mo25Ta25W25 and V20Nb20Mo20Ta20W20 refractory high entropy alloys, Intermetallics 19(5) (2011) 698-706.

[42] O.N. Senkov, J.M. Scott, S.V. Senkova, F. Meisenkothen, D.B. Miracle, C.F. Woodward, Microstructure and elevated temperature properties of a refractory TaNbHfZrTi alloy, J Mater Sci 47(9) (2012) 4062-4074.

[43] M.J. Yao, K.G. Pradeep, C.C. Tasan, D. Raabe, A novel, single phase, non-equiatomic FeMnNiCoCr high-entropy alloy with exceptional phase stability and tensile ductility, Scripta Mater 72-73 (2014) 5-8.

[44] N.G. Jones, J.W. Aveson, A. Bhowmik, B.D. Conduit, H.J. Stone, On the entropic stabilisation of an Al0.5CrFeCoNiCu high entropy alloy, Intermetallics 54 (2014) 148-153.

[45] M. Komarasamy, N. Kumar, R.S. Mishra, P.K. Liaw, Anomalies in the deformation mechanism and kinetics of coarse-grained high entropy alloy, Mat Sci Eng a-Struct 654 (2016) 256-263.

[46] Y. Zou, S. Maiti, W. Steurer, R. Spolenak, Size-dependent plasticity in an Nb25Mo25Ta25W25 refractory high-entropy alloy, Acta Mater 65 (2014) 85-97.

[47] O.N. Senkov, G.B. Wilks, D.B. Miracle, C.P. Chuang, P.K. Liaw, Refractory high-entropy alloys, Intermetallics 18(9) (2010) 1758-1765.

[48] S.Y. Chen, X. Yang, K.A. Dahmen, P.K. Liaw, Y. Zhang, Microstructures and Crackling Noise of AlxNbTiMoV High Entropy Alloys, Entropy-Switz 16(2) (2014) 870-884.

[49] A. Takeuchi, K. Amiya, T. Wada, K. Yubuta, W. Zhang, High-Entropy Alloys with a Hexagonal Close-Packed Structure Designed by Equi-Atomic Alloy Strategy and Binary Phase Diagrams, Jom-Us 66(10) (2014) 1984-1992.

[50] B. Cantor, I.T.H. Chang, P. Knight, A.J.B. Vincent, Microstructural development in equiatomic multicomponent alloys, Mat Sci Eng a-Struct 375 (2004) 213-218.

[51] P.K. Huang, J.W. Yeh, T.T. Shun, S.K. Chen, Multi-principal-element alloys with improved oxidation and wear resistance for thermal spray coating, Adv Eng Mater 6(1-2) (2004) 74-78.

[52] T.K. Chen, T.T. Shun, J.W. Yeh, M.S. Wong, Nanostructured nitride films of multi-element high-entropy alloys by reactive DC sputtering, Surf Coat Tech 188 (2004) 193-200.

[53] J.W. Yeh, S.K. Chen, S.J. Lin, J.Y. Gan, T.S. Chin, T.T. Shun, C.H. Tsau, S.Y. Chang, Nanostructured high-entropy alloys with multiple principal elements: Novel alloy design concepts and outcomes, Adv Eng Mater 6(5) (2004) 299-303.

[54] W. Guo, W. Dmowski, J.Y. Noh, P. Rack, P.K. Liaw, T. Egami, Local Atomic Structure of a High-Entropy Alloy: An X-Ray and Neutron Scattering Study, Metall Mater Trans A 44A(5) (2013) 1994-1997.

[55] K.Y. Tsai, M.H. Tsai, J.W. Yeh, Sluggish diffusion in Co-Cr-Fe-Mn-Ni high-entropy alloys, Acta Mater 61(13) (2013) 4887-4897.

[56] Y. Ma, G.J. Peng, D.H. Wen, T.H. Zhang, Nanoindentation creep behavior in a CoCrFeCuNi high-entropy alloy film with two different structure states, Mat Sci Eng a-Struct 621 (2015) 111-117.

[57] C.W. Tsai, M.H. Tsai, J.W. Yeh, C.C. Yang, Effect of temperature on mechanical properties of Al0.5CoCrCuFeNi wrought alloy, J Alloy Compd 490(1-2) (2010) 160-165.

[58] C.P. Lee, Y.Y. Chen, C.Y. Hsu, J.W. Yeh, H.C. Shih, The effect of boron on the corrosion resistance of the high entropy alloys Al0.5CoCrCuFeNiBx, J Electrochem Soc 154(8) (2007) C424-C430.

[59] B. Gludovatz, A. Hohenwarter, D. Catoor, E.H. Chang, E.P. George, R.O. Ritchie, A fracture-resistant high-entropy alloy for cryogenic applications, Science 345(6201) (2014) 1153-1158.

[60] M.H. Tsai, C.W. Wang, C.W. Tsai, W.J. Shen, J.W. Yeh, J.Y. Gan, W.W. Wu, Thermal Stability and Performance of NbSiTaTiZr High-Entropy Alloy Barrier for Copper Metallization, J Electrochem Soc 158(11) (2011) H1161-H1165.

[61] W.H. Wu, C.C. Yang, J.W. Yeh, Industrial development of high-entropy alloys, Ann Chim-Sci Mat 31(6) (2006) 737-747.

[62] Y.P. Lu, Y. Dong, S. Guo, L. Jiang, H.J. Kang, T.M. Wang, B. Wen, Z.J. Wang, J.C. Jie, Z.Q. Cao, H.H. Ruan, T.J. Li, A Promising New Class of High-Temperature Alloys: Eutectic High-Entropy Alloys, Sci Rep-Uk 4 (2014).

[63] M.F. del Grosso, G. Bozzolo, H.O. Mosca, Determination of the transition to the high entropy regime for alloys of refractory elements, J Alloy Compd 534 (2012) 25-31.

[64] R. Carroll, C. Lee, C.-W. Tsai, J.-W. Yeh, J. Antonaglia, B.A.W. Brinkman, M. LeBlanc, X. Xie, S. Chen, P.K. Liaw, K.A. Dahmen, Experiments and Model for Serration Statistics in Low-Entropy, Medium-Entropy, and High-Entropy Alloys, Sci Rep-Uk 5 (2015) 16997.

[65] K.A. Dahmen, Y. Ben-Zion, J.T. Uhl, Micromechanical Model for Deformation in Solids with Universal Predictions for Stress-Strain Curves and Slip Avalanches, Physical Review Letters 102(17) (2009).

[66] Y. Wu, W.H. Liu, X.L. Wang, D. Ma, A.D. Stoica, T.G. Nieh, Z.B. He, Z.P. Lu, In-situ neutron diffraction study of deformation behavior of a multi-component high-entropy alloy, Appl Phys Lett 104(5) (2014).

[67] F. Otto, A. Dlouhy, C. Somsen, H. Bei, G. Eggeler, E.P. George, The influences of temperature and microstructure on the tensile properties of a CoCrFeMnNi high-entropy alloy, Acta Mater 61(15) (2013) 5743-5755.

[68] N. Kumar, M. Komarasamy, P. Nelaturu, Z. Tang, P.K. Liaw, R.S. Mishra, Friction Stir Processing of a High Entropy Alloy Al0.1CoCrFeNi, Jom-Us 67(5) (2015) 1007-1013.

[69] A.J. Zaddach, C. Niu, C.C. Koch, D.L. Irving, Mechanical Properties and Stacking Fault Energies of NiFeCrCoMn High-Entropy Alloy, Jom-Us 65(12) (2013) 1780-1789.

[70] X.D. Xu, P. Liu, S. Guo, A. Hirata, T. Fujita, T.G. Nieh, C.T. Liu, M.W. Chen, Nanoscale phase separation in a fcc-based CoCrCuFeNiAl0.5 high-entropy alloy, Acta Mater 84 (2015) 145-152.

[71] Z. Li, K.G. Pradeep, Y. Deng, D. Raabe, C.C. Tasan, Metastable high-entropy dual-phase alloys overcome the strength–ductility trade-off, Nature advance online publication (2016).

[72] Z.J. Zhang, M.M. Mao, J.W. Wang, B. Gludovatz, Z. Zhang, S.X. Mao, E.P. George, Q. Yu, R.O. Ritchie, Nanoscale origins of the damage tolerance of the high-entropy alloy CrMnFeCoNi, Nat Commun 6 (2015).

[73] S.Y. Chen, X. Xie, B.L. Chen, J.W. Qiao, Y. Zhang, Y. Ren, K.A. Dahmen, P.K. Liaw, Effects of Temperature on Serrated Flows of Al0.5CoCrCuFeNi High-Entropy Alloy, Jom-Us 67(10) (2015) 2314-2320.

[74] G. Wei, B. Bhushan, S.J. Jacobs, Nanoscale fatigue and fracture toughness measurements of multilayered thin film structures for digital micromirror devices, Journal of Vacuum Science & Technology A 22(4) (2004) 1397-1405.

[75] X.W. Gu, Z. Wu, Y.-W. Zhang, D.J. Srolovitz, J.R. Greer, Microstructure versus flaw: Mechanisms of failure and strength in nanostructures, Nano letters 13(11) (2013) 5703-5709.

[76] S. Kumar, X. Li, A. Haque, H. Gao, Is stress concentration relevant for nanocrystalline metals?, Nano letters 11(6) (2011) 2510-2516.

[77] J.-H. Huang, Y.-H. Chen, A.-N. Wang, G.-P. Yu, H. Chen, Evaluation of fracture toughness of ZrN hard coatings by internal energy induced cracking method, Surface and Coatings Technology 258(0) (2014) 211-218.

[78] A.-N. Wang, G.-P. Yu, J.-H. Huang, Fracture toughness measurement on TiN hard coatings using internal energy induced cracking, Surface and Coatings Technology 239 (2014) 20-27.

[79] S. Zhang, D. Sun, Y.Q. Fu, H.J. Du, Toughness measurement of thin films: a critical review, Surf Coat Tech 198(1-3) (2005) 74-84.

[80] B.N. Jaya, V. Jayaram, S.K. Biswas, A new method for fracture toughness determination of graded (Pt,Ni)Al bond coats by microbeam bend tests, Philos Mag 92(25-27) (2012) 3326-3345.

[81] S. Liu, J.M. Wheeler, P.R. Howie, X.T. Zeng, J. Michler, W.J. Clegg, Measuring the fracture resistance of hard coatings, Appl Phys Lett 102(17) (2013).

[82] K. Matoy, H. Schonherr, T. Detzel, T. Schoberl, R. Pippan, C. Motz, G. Dehm, A comparative micro-cantilever study of the mechanical behavior of silicon based passivation films, Thin Solid Films 518(1) (2009) 247-256.

[83] R.W. Rice, Microstructural dependence of fracture energy and toughness of ceramics and ceramic composites versus that of their tensile strengths at 22 degrees C, J Mater Sci 31(17) (1996) 4503-4519.

[84] A.H. Cottrell, Commentary. A brief view of work hardening, in: F.R.N. Nabarro, M.S. Duesbery (Eds.), Dislocations in Solids, Elsevier2002, pp. vii-xvii.

[85] S. Mader, C. Leitz, A. Seeger, Work Hardening and Dislocation Arrangement of Fcc Single Crystals .1. Plastic Deformation and Slip Line Studies of Nickel Single Crystals, J Appl Phys 34(11) (1963) 3368-&.

[86] S. Mader, H.M. Thieringer, A. Seeger, Work Hardening and Dislocation Arrangement of Fcc Single Crystals .2. Electron Microscope Transmission Studies of Ni-Co Single Crystals and Relation to Work-Hardening Theory, J Appl Phys 34(11) (1963) 3376-&.

CHAPTER 2

EXPERIMENTAL METHODS

This chapter describes the experimental methods used in this thesis to study the structure and deformation mechanisms of ceramics and alloys. The methods include diffraction contrast imaging, scanning electron nanobeam diffraction (SEND), in situ TEM mechanical testing, and finally focused ion beam (FIB) sample preparation method. We start on the general method of transmission electron microscopy.

2.1. Transmission Electron Microscopy

Transmission electron microscopy (TEM) is a major characterization technique for studying the structure and chemistry of materials by providing high spatial resolution imaging and diffraction. The resolution of a microscope in general is dependent on the wavelength of radiation. According to the Rayleigh criterion, the resolution is defined as $d_{min} = 0.61\frac{\lambda}{nsin\theta}$ where $nsin\theta$ is the numerical aperture (NA), θ is half the acceptance angle of the lens and λ is the radiation wavelength. For TEM operating at 100 keV, $n = 1$ in vacuum, $\lambda = 0.037$Å and $\theta = 10mrad$, and the resultant spatial resolution $d_{min} = 2.3$ Å, which far better than the resolution of optical microscopes.

In a conventional TEM, electrons are emitted from a thermionic electron gun or a field emission gun and accelerated to 80-300 keV by a direct current (DC) electric field. The emitted

electrons are focused into a small beam using a group of condenser lenses, which composes the illumination system of TEM. They collectively control the convergence angle of the electron beam and its size, and thus the illumination on the sample. A condenser aperture is often used to exclude the large angle electrons, which suffer most from the lens aberrations; their inclusion in imaging degrade the spatial resolution.

A major advancement of modern TEM was the invention of the single-field condenser objective lens by Riecke and Ruska[1]. The sample is put at the center of the pole-piece gap which provides maximum space for specimen tilt and translation. It also allows the access by energy-dispersive X-ray (EDX) detectors to determine the chemical composition of specimen. The objective lens is the most crucial lens of the entire microscope. It offers short focal distance and, thus, a large magnification coefficient. The objective lens has a prefield above the sample acting as a final condenser lens to form the electron probe. The magnetic field below the sample acts as the magnifying lens for imaging. The image resolution and the electron probe used by scanning transmission electron microscopy (STEM) are limited by the aberration of objective lens. The aberration increases with the angle between electron beam and optical axis, so it is the objective lens which converge the beam with the largest angle that determines the image resolution or the smallest electron probe in STEM mode.

The beam transverses the sample close to a normal incidence and diffracted by the sample. The transmitted and diffracted beams are collected by the objective lens and form an image.

Intermediate and projection lenses are used to further magnify the image. In the diffraction mode, the intermediate and projection lenses take the diffraction pattern on the back focal plane and project it on the screen. The magnified image or diffraction pattern is shown on the phosphor screen or camera. The geometric optics of a modern TEM is shown in Fig. 2.1.

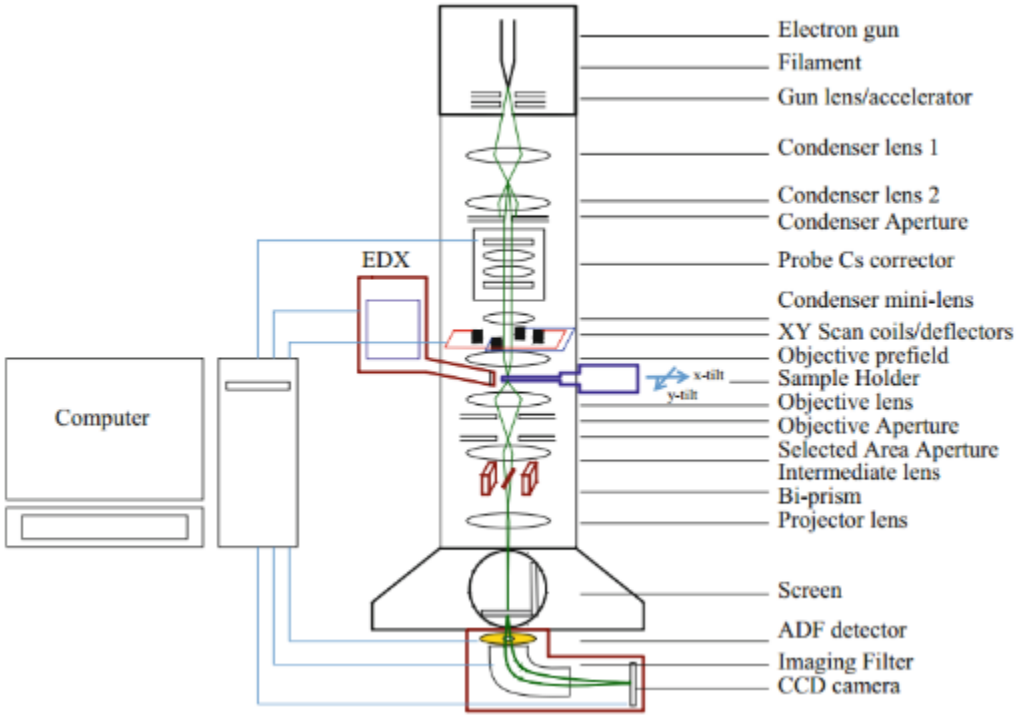

Figure 2.1. *Schematic illustration of a TEM with its attachments[2].*

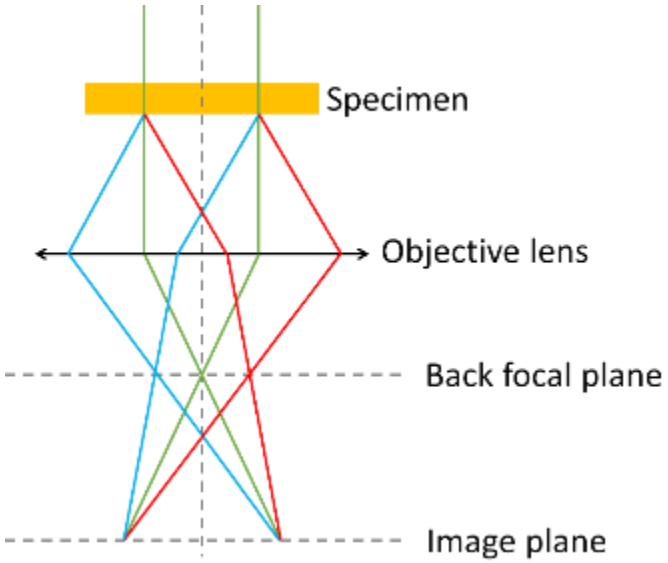

Figure 2.2. *The ray diagram in the objective lens area.*

Figure 2.2 shows the ray diagram in the objective lens area. When a parallel beam illuminates the specimen, the crystallographic planes in specimen will diffract the electron beam based on the Bragg's law. The diffracted beams are collected by the objective lens and focused on the back focal plane. In the diffraction mode, the back focal plane is projected by the intermediate and projection lenses and the diffraction pattern is magnified and shown on the screen. Below the back focal plane is the image plane where magnified image of the specimen is projected. Since this plane is conjugate with the specimen, the selected area aperture is located at this position to create a virtual aperture at the plane of specimen.

Objective aperture is located at back focal plane and often used to selected transmitted, diffracted or both to form an image. When the objective aperture is placed to only allow the center beam to go through, a bright field (BF) image is formed. The specimen area which diffracts the

electron beam will be shown as dark contrast. On the other hand, if the objective aperture is place to select one or more diffracted beam to pass through, a dark field (DF) image is formed where the specimen area diffracting the electron beam has bright contrast. To form a HREM image, both direct beam and diffracted beams are selected to form an interference pattern under zone axis imaging condition.

In the diffraction mode, a selected area diffraction pattern (SAED) is formed by inserting a selected area aperture on the image plane of objective lens. When a parallel beam is illuminated on the sample, sharp diffraction spots are presented on the back focal plane. If a convergent beam is used to form an electron probe on the sample, the diffraction is consisted of disk patterns. This technique is called convergent beam electron diffraction (CBED) which is powerful in studying crystallographic symmetry, lattice strain, structure factor and sample thickness[3].

2.2. Diffraction Contrast Imaging

The diffraction contrast imaging is defined as the change in intensity of diffracted beam due to the local variations of diffraction conditions, such as lattice strain, chemical composition, or sample thickness. Objective aperture is used to allow direct or diffracted beams to pass through, which act as the effective electron sources. According to Abbe's image formation theory, the Fourier transform of the diffracted beams forms image and the image resolution is limited by the aperture size.

The proper way to set up the dark field diffraction contrast imaging is to tilt the incident beam so that the diffracted beam by the sample aligns with the optical axis. Then the specimen is tilted to a particular diffraction condition and an objective aperture is inserted at the center to allow the diffracted beam to go through. Alternatively, dark field imaging could be obtained by directly placing the objective aperture on an off-axis diffracted beam. However, the image formed by this method suffers from astigmatism due to the lens aberration.

2.2.1. Column Approximation

In the column approximation, the crystal sample is divided into multiple columns along the incident beam direction *z*. Within the columns, the atomic displacements vary only along the column direction. The assumption is that the size of column is small enough that the atomic displacement variation normal to the *z* direction is constant, while the size is large enough to allow electron not being diffracted out of the column.

Using the column approximation with the two-beam theory, the intensity of the diffracted beam is shown to be[4]

$$I_g = \left|\phi_g(t)\right|^2 = \frac{1}{1+\omega^2}\sin^2[\frac{\pi t}{\xi_g}\sqrt{1+\omega^2}] \qquad (2.1)$$

where I_g is the intensity of diffracted beam, ϕ_g is the exit wave function and t is the sample thickness, $\omega = S_g\xi_g$ is a dimensionless parameter, S_g is the excitation error and ξ_g is the

extinction distance. For a common wedge TEM sample, the edge of the wedge will show dark contrast in dark field images, while the bright field image shows the opposite contrast. The contrast oscillates with the specimen thickness which is called thickness fringes.

Another characteristic diffraction contrast is the bending contour, which are observed in specimens that are bent under stress. Due to the sample bending, the orientation of crystal lattice varies spatially, which changes the diffraction conditions. When the diffraction condition satisfies

$$\omega = \pm\sqrt{\left(\frac{n\xi_g}{t}\right)^2 - 1} \tag{2.2}$$

where n is an integer. Since this relationship is applicable to g and $-g$ diffraction condition, the bending contour is generally symmetric, which is also helpful in locating the specimen area near zone axis.

2.2.2. Diffraction Contrast from Dislocations

Samples contains various defects, such as dislocations and stacking faults, can be imaged using diffraction contrast. These defects generate atomic displacement and lattice strain fields which gives them unique diffraction contrast. To explain these diffraction contrast, we introduce the Howie-Whelan equation under the kinematic approximation

$$\frac{d\phi_g(z)}{dz} = \frac{i\pi\phi_0}{\xi_g}\exp(-2\pi i S_g z) \tag{2.3}$$

where z is the distance travelled by the diffracted beam within sample, and ϕ_0 is the incident

wave. When the strain fields ***R(z)*** is present in the crystal, it will introduce an additional phase to the equation (2.3)

$$\frac{d\phi_g(z)}{dz} = \frac{i\pi\phi_0}{\xi_g}\exp(-2\pi i[\boldsymbol{g}\cdot\boldsymbol{R}(\boldsymbol{z}) + S_g z]) \qquad (2.4)$$

From equation (2.4), an important conclusion can be reached that the product $\boldsymbol{g}\cdot\boldsymbol{R}(\boldsymbol{z})$ cannot be zero in order to image the strain field. When the product is zero, there will be no diffraction contrast in the image despite of strain fields. Therefore, to clearly observe a defect, the magnitude of $\boldsymbol{g}\cdot\boldsymbol{R}(\boldsymbol{z})$ should be sufficiently large.

The most common defects in crystals are dislocations, which consists of a crystal plane terminating within crystal. The atoms above and below the dislocation core are displaced by half the Burger's vector. The abrupt change of atomic displacement gives fringes at dislocation core position. Away from the core area, the strain field varies continuously and yields a phase change of $\alpha = 2\pi\boldsymbol{g}\cdot\boldsymbol{R}(\boldsymbol{z})$. Since the atomic displacements on the left and right side of dislocations are opposite, the phase change α is added to the thickness phase $2\pi S_g z$ on one side and subtracted on the other side. As a result, one side will be further away from the Bragg diffraction condition and the other side will be closer to the Bragg condition. Thus, dislocations are always shown as strong line contrast on one side of dislocations.

There are three types of dislocations in deformed crystals, namely edge, screw, and mixed dislocations. The edge dislocation is formed by inserting an extra half crystal plane into a perfect crystal lattice. The plane is terminating inside the crystal where the end of extra plane is the

dislocation core (AA' in Fig. 2.3(a)). The Burger's vector of edge dislocation is perpendicular to the dislocation line. The screw dislocation is formed by shearing one part of crystal respect to the rest (see Fig. 2.3(b)) whose Burger's vector is parallel to the dislocation line. The mixed dislocation is a combination of edge and screw dislocations.

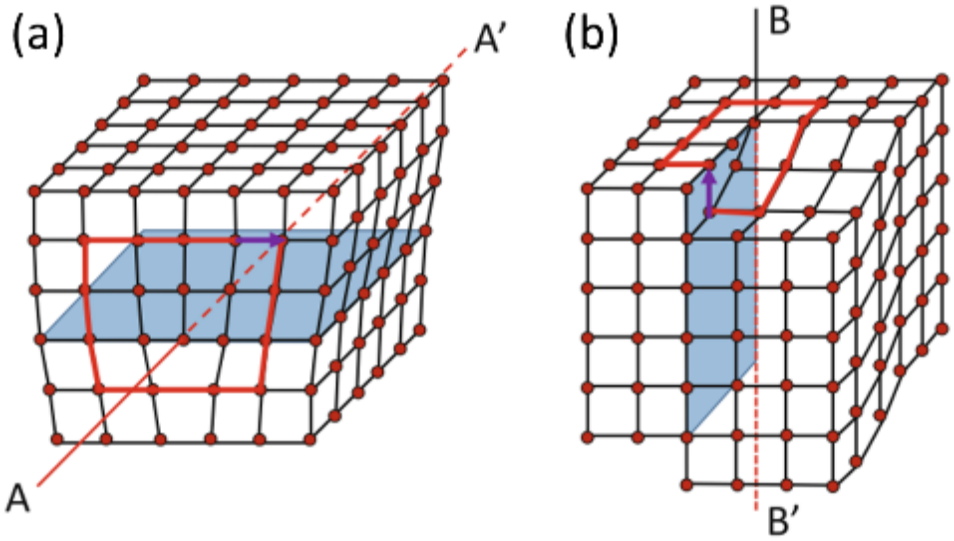

Figure 2.3. *The atomic configuration for edge and screw dislocations. AA' and BB' are dislocation lines and the purple arrows represent the Burger's vectors[4].*

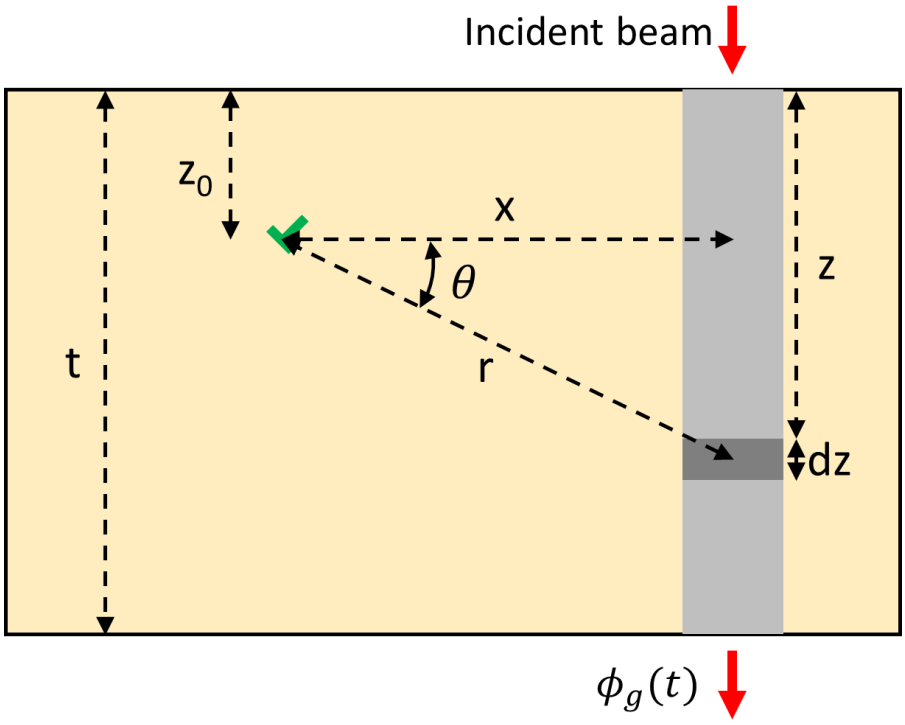

Figure 2.4. *The effect of a screw dislocation on the electron wave in the column approximation (redrawn from [5]).*

The strain fields of edge and screw dislocations are in different format. For a screw dislocation residing at position z in a sample (see Fig. 2.4), the atomic displacement vector away from the dislocation core is

$$\boldsymbol{R} = \boldsymbol{b}\frac{\theta}{2\pi} = \frac{\boldsymbol{b}}{2\pi}\arctan(\frac{z}{x}) \tag{2.5}$$

and the additional phase is

$$\alpha = 2\pi \boldsymbol{g}\cdot\boldsymbol{R} = \boldsymbol{g}\cdot\boldsymbol{b}\arctan\left(\frac{z}{x}\right) = n\arctan\left(\frac{z}{x}\right) \tag{2.6}$$

Thus, the exit wave after pass through a screw dislocation is

$$\phi_g(t) = \frac{i\pi}{\xi_g}\int_0^t e^{-i(2\pi S_g z + n\arctan(\frac{z}{x}))}dz \tag{2.7}$$

For an edge dislocation, the strain field is much complicated. However, under certain approximations, we could represent the strain field of edge dislocations as

$$\alpha = 2\pi \boldsymbol{g} \cdot \boldsymbol{R} \approx n \arctan\left(\frac{2z}{x}\right) \tag{2.8}$$

Equation (2.8) indicates that the contrast of edge dislocations is similar to screw dislocations. Under same diffraction condition the edge dislocation will be wider than screw dislocations. An example bright field image of dislocation arrays in deformed $Al_{0.1}CoCrFeNi$ high-entropy alloys is shown in Fig. 2.5.

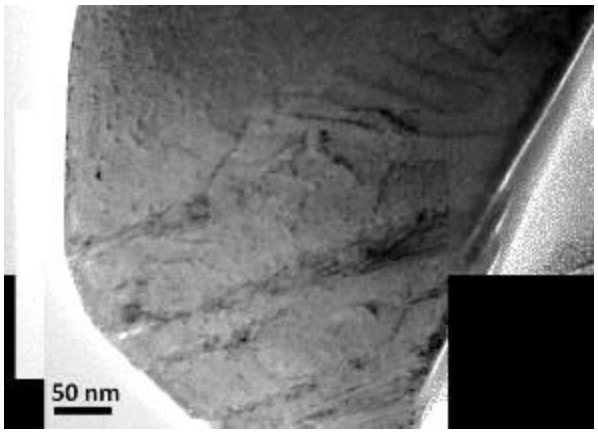

Figure 2.5. *A bright field TEM image of dislocation arrays in deformed $Al_{0.1}CoCrFeNi$ high-entropy alloys.*

2.3. Scanning Electron Nanobeam Diffraction

2.3.1. Historical Development

Electron nanodiffraction technique was first developed by Cowley[6] with a scanning transmission electron microscope (STEM). 1 nm electron probe can be formed with small condenser aperture

and proper focus settings. In the STEM mode, the electron probe is scanned across the specimen using two deflection coils and a diffraction pattern is gathered at each scanning point. Parallel beam electron nanodiffraction was developed later by Zuo et al. in 2003[7] by adding another mini condenser lens. In a field emission gun that has good beam coherence, a wealthy of structural information can be obtained. However, in many cases multiple nanodiffraction patterns at different specimen area are needed to study the complex structure materials. To overcome this issue, a parallel beam diffraction mode in STEM was developed by Kolb et al.[8] to incorporate nanobeam diffraction mode with STEM scanning operation. Alternatively, instead of using STEM mode, Tao et al.[9] reported a scanning electron nanodiffraction (SEND) technique operating in TEM mode by controlling the deflection coils using DigitalMicrograph script. With field emission gun (FEG), the smallest electron probe size is ~1.7 nm with a convergence angle 0.5 mrad. However, due to strong beam intensity of FEG gun, sample damage, heating and drifting become major issues in this technique. To resolve this issue, Kim et al.[10] recently also reported a low-dose SEND technique utilizing LaB6 electron gun which is suitable to study beam sensitive specimens.

2.3.2. Electron Probe Formation and Illumination System

The illumination system for SEND is shown in Fig. 2.6. Three condenser lenses are used, namely condenser lens 1 (CL1), condenser lens 2 (CL2), and condenser minilens (CM). The prefield of objective lens (OL) is also used to form the electron probe. The experiment is done in the NBD mode with CM lens excited. The CL1 first demagnifies the electron probe coming from the

electron source. The crossover of electron source after CL1 decreases when the excitation of CL1 is stronger. The CL2, CM and OL together focus the beam on the sample.

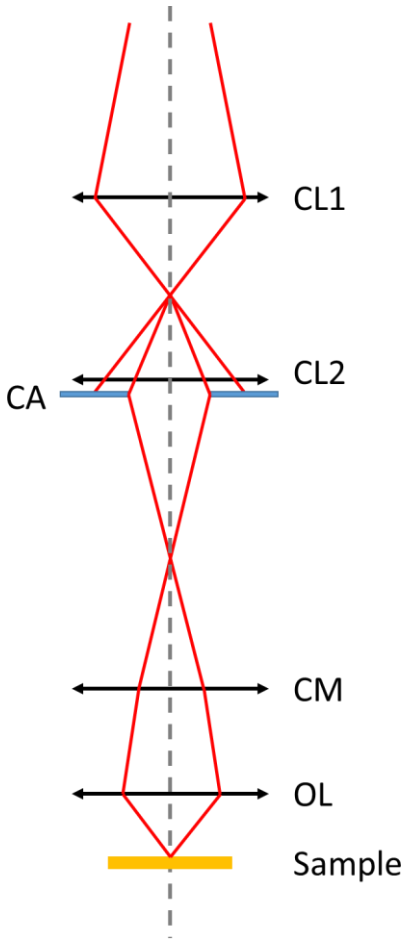

Figure 2.6. *The illumination system for SEND. Three condenser lenses and objective lens prefield is used to form the electron probe.*

The actual probe size is determined by a combination effect of demagnification of condenser lenses, the aberration, condenser aperture diffraction, and defocus. The electron probe diameter can be expressed as the following equation.

$$d_0^2 = d_s^2 M^2 + d_d^2 + d_{sa}^2 + d_c^2 + d_f^2$$
$$= d_s^2 M^2 + \left(\frac{0.6\lambda}{\theta_c}\right)^2 + (0.5 C_s \theta_c^3)^2 + \left(\frac{\Delta E_0}{E_0} C_c \theta_c\right)^2 + (2\theta_c \Delta f)^2 \quad (2.9)$$

where d_0 is the electron probe diameter, d_s is the source image diameter, M is the demagnification by Cl2, CM and OL, d_d is the condenser aperture diffraction limit, d_{sa} is the spherical aberration, d_c is the chromatic aberration, d_f is the focusing error, λ is the electron beam wavelength, θ_c is the beam convergence angle, C_s and C_c are spherical and chromatic aberration coefficient and Δf is the defocus. The diameter of electron probe is mostly dependent on the electron source image size. By changing the setting of CL1, a series of source image size can be obtained. The magnification M is controlled by the alpha setting. The focusing error can be avoided by proper sample position and the chromatic and spherical aberration can be omitted if compared with the small condenser aperture induced diffraction effect.

2.3.3. Microscope Alignment and Automated Scanning Electron Nanodiffraction

Regular TEM alignment procedure should be performed including the pivot point alignment, which separates the coupling between beam shift and beam tilt. In SEND experiment, beam should not tilt during the scanning (beam shift) otherwise it will complicate the interpretation of diffraction patterns.

Next, the diffraction focus needs to be optimized to let the diffraction center (000) stay at the same position during scanning. Improper diffraction focus will cause diffraction pattern shift during scanning and, thus, make it difficult to analyze the data. The diffraction focus is controlled

by intermediate lens focus. Figure 2.7 shows three cases of intermediate lens focus, namely (a) strong, (b) proper, and (c) weak. The electron beams marked by '1', '2', and '3' represent different scanning positions across the sample. In the strong and weak case, the diffraction pattern will shift around, while proper intermediate lens focus will let the diffraction pattern stay at the same position.

A general procedure to optimize the diffraction focus which is also applicable to other TEM is shown as follows:

1) Perform the regular TEM alignment, including CL aperture, gun tilt, gun shift, pivot point, etc.;

2) Move the sample out of the illumination area and switch to diffraction mode, the diffraction center could be seen on the screen;

3) Use BEAM SHIFT function to shift the electron beam around;

4) Adjust diffraction focus to make the diffraction center not moving.

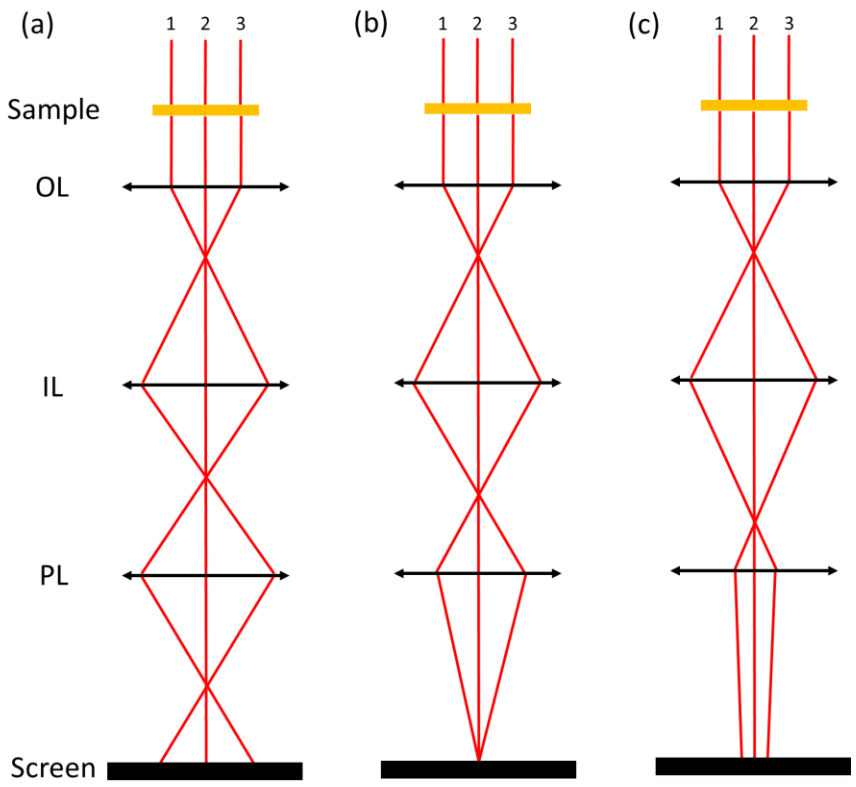

Figure 2.7. *Improper intermediate lens settings shown in a) and c) move the diffraction pattern around during scanning, while proper setting will let diffraction patterns stay at the same position (b) (redrawn from Ref [10]).*

In order to automatically control the electron beam scanning and record diffraction patterns at each scanning point, a DigitalMicrograph script is used to control the deflection coil to scan the electron probe and the CCD camera to record the diffraction. There are two main functions to control the deflection coil, EMGetBeamShift and EMSetBeamShift. The EMGetBeamShift is used to read the settings of illumination deflection coils and store them into variables. The EMSetBeamShift is used to shift the electron beam to the designated position. With these two functions, the scanning process is automated. Another script is written to control the diffraction

pattern acquisition, which is called SSCGainNormalizedBinnedAcquire. This function worked with the scanning script and record the diffraction pattern during scanning.

Figure 2.8 shows the complete schematic of automated SEND system at the University of Illinois.

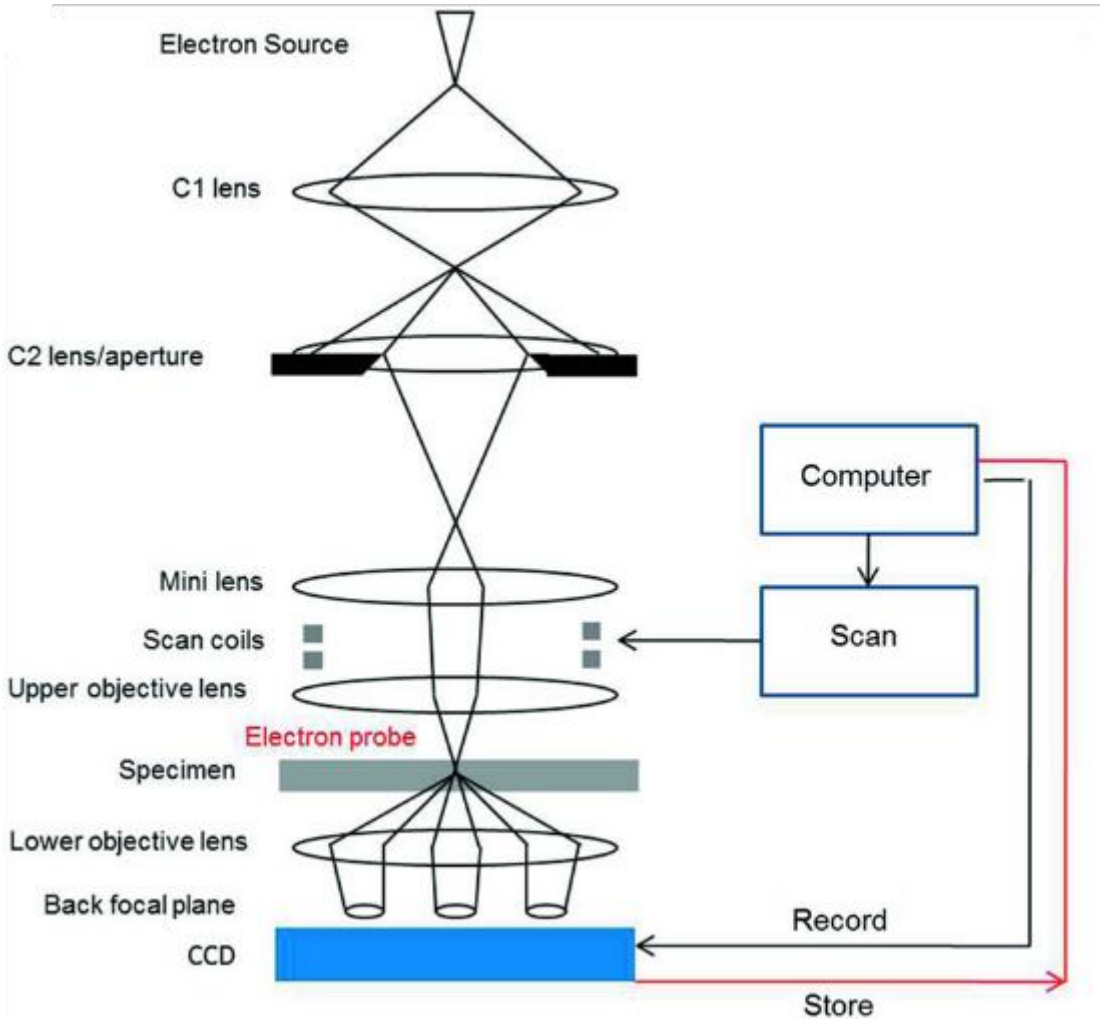

Figure 2.8. *The schematic of the automated SEND system at University of Illinois at Urbana-Champaign[11].*

2.3.4. Automated Diffraction Indexing

The grain orientation for nanocrystalline materials is difficult to determine with traditional EBSD methods. SEND provides nanometer spatial resolution to determine local grain orientation. After the acquisition of diffraction patterns, an automated diffraction indexing function is developed by Zuo[11], which is based on the normalized cross-correlation (NCC) method. The basic working principle of this method is following.

1) Use QED software to calculate the simulated diffraction pattern for every possible orientation in the stereographic projection map;

2) Determine the diffraction spot center and the camera constant for experimental diffraction pattern;

3) Calculate the circular and radial intensity distribution for experimental diffraction patterns;

4) Similarly, calculate the circular and radial intensity distribution for simulated diffraction patterns;

5) Calculate the NCC of experimental and simulated diffraction pattern using radial and circular intensity and select the most similar simulated diffraction patterns;

6) Using NCC to directly compare experimental pattern with the selected most similar simulated diffraction patterns. Choose the best match of simulated diffraction pattern.

One example of automated indexing results is shown in Fig. 2.9.

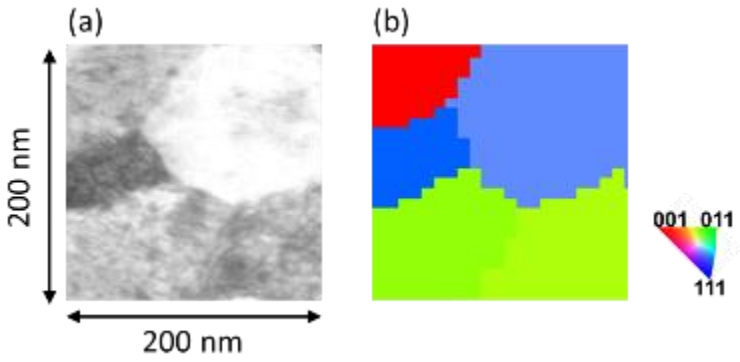

Figure 2.9. *(a) A BF image of nanocrystalline TiN thin film with multiple grains. (b) the corresponding orientation map.*

2.4. In Situ TEM Mechanical Testing

2.4.1. In Situ Straining Techniques

The earliest in situ TEM mechanical testing was carried out with a tensile test specimen holder. Specimens are fixed by two jaws and slowly pulled on one side. Using an electric motor, the tensile displacement rate could be controlled from 10 nm/s to 10 um/s[12-15]. This technique remains popular due to its compatibility to a wide range of specimens. The strain transmission is very rigid in this holder, so it can be applied to both ceramic thin films and alloys. Additionally, the specimen can be also heated using resistive heaters or cooled using liquid nitrogen or He. Special holders have also been developed. For example, Han et al. reported a heating holder with the deformation actuators for performing atomic scale TEM mechanical testing[16]. The deformation actuators are composed of two metal strips with different thermal expansion coefficients. When the temperature is increased, the two strips bend towards opposite directions with a resultant strain rate of ~10^{-4} /s.

A major advantage of this custom-built holder is its double-tilt capability, so high resolution TEM can be conducted during testing to obtain atomic scale information of deformation.

Nanoindentation holders have attracted considerable attentions recently due to its unique capability to measure the force and displacement during deformation. This technique is based on the popular nanoindentation technique as described in [17]. The force and displacement are controlled and measured by a capacitance change between a moveable plate and a grounded plate. In nanoindentation, the force and displacement sensor is used to drive a sharp tip at the forces from 10 nN to 10 N. By measuring the load-displacement curves, this technique can measure the elastic modulus, hardness and yield strength of materials[18]. Inducing nanoindentation into the TEM holder greatly revolutionize the in situ TEM mechanical testing by providing quantitative stress-strain data. Hysitron and Nanofactory Instruments were first companies commercially fabricated these holders.

In order to carry out the nanoindentation experiment inside a TEM, the specimen needs to have a specific geometry and be electron-transparent. The most widely-used sample geometry is the cylindrical column, which is called micropillar or nanopillar depending on the column diameter. The advantage of the column geometry is that it has an almost constant cross-section area to transmit the strain and stress uniformly and the stress can be easily calculated from the load values. Other sample geometries have also been used, including thin-films, clamped beam[19] and wedges[20]. However, stress concentration is highly dependent on the geometries of samples

which changes during indentation, so finite element analysis (FEA) is needed to understand the stress distribution.

Special micro electromechanical systems (MEMS) have also been developed to deform the sample inside TEM[21]. For example, the push-to-pull device is a passive MEMS device, which is mounted on a straining or nanoindentation holder, to perform tensile testing on nanowires or dogbone shaped samples. While the active MEMS device requires external electrical signal input to induce the deformation.

2.4.2. Hysitron PI95 TEM Holder

Hysitron PI95 TEM holder is a commerciali nanoindentation TEM holder. The holder is controlled by a control box including a transducer controller, a piezo controller, and a digital signal processor (DSP) capable of 100 million instructions per second (MIPS). The DSP controller is programmable and has a memory space for storing digitized data. The DSP controller employed in this thesis always executes at loop rates of 78 kHz with damping capability. Damping feedback loop is critical since the indenter is in a vacuum environment with low air damping and the indenter will take much longer time to settle which seriously affects the mechanical testing. DSP controls the system quality factor Q to modify the system damping. The lower the Q value, the greater the indenter damping. To control Q, a phase-shifted drive signal is added to the original indenter displacement signal. The mixed signal goes through a feedback loop and produce Q-controlled indenter

displacement. It provides various modes to deform the sample, such as load control mode and displacement control mode. The load control mode utilizes a feedback control algorithm to adjust the contact force. In this way, the controller can provide a predetermined contact force vs time function. Similarly, displacement control mode uses a feedback control loop to control the indenter displacement to follow the programmed displacement rates. The control box is connected to a computer running the software via a USB link. The DSP controller communicates with the transducer controller, which is connected to the actuator capacitive transducer housed within the TEM holder. Additionally, it also communicates with the piezo controller, which is connected to the 3D piezo-electric actuator housed within the TME holder for positioning the nanoindenter The indenter can be a flat punch or cube corner boron-doped diamond probe.

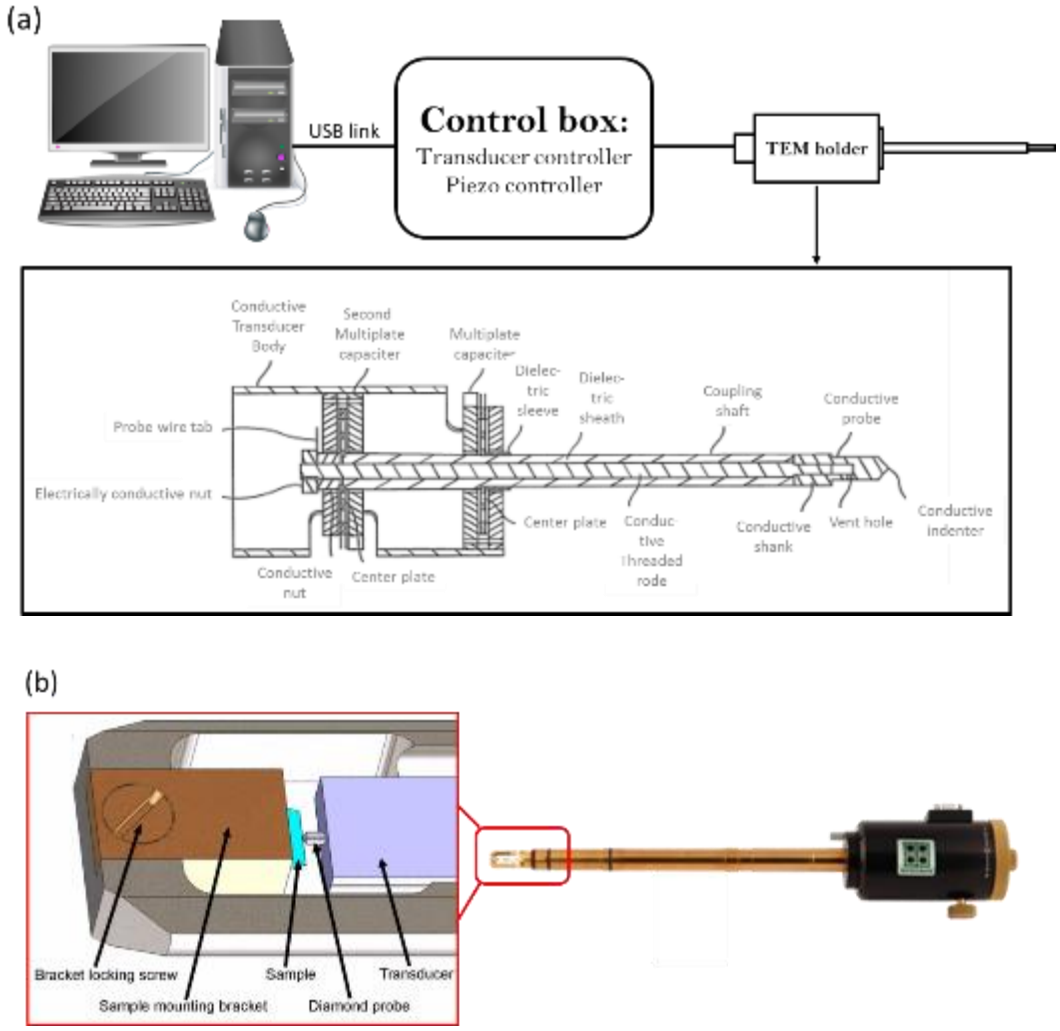

Figure 2.10. *Hysitron PI95 TEM holder system. a) the block diagram for the control system. b) a cross-sectional drawing of the inner structure of PI95 TEM holder.[22]*

2.4.2.1 Transducer

The transducer used to apply and measure the load and displacement in the PI95 holder is the Triboscope© three plate capacitive transducer. Figure 2.11 shows the structure of the transducer. The middle plate is the moveable plate which is attached to the nanoindenter and two outer plates

are reference plates. Alternating current (AC) current is applied to the reference plates with 180 degree difference. This results in a minimum electric potential at the center position and maximum at two outer plates. The electric field potential varies linearly between the minimum and maximum. The moveable plate has the same potential present at its location. By measuring the electric potential of moveable plate, the displacement can be measured. To apply a force on the sample, an additional DC potential is added to the upper plates and the moveable plate moves downwards due to the electrostatic attraction between the moveable plate and the bottom plate. The load is measured from the voltage applied on the upper reference plate. The maximum applied force is 1.5 mN with a noise floor of 200 nN. The displacement measurement range is up to 5 um with noise floor of 0.4 nm. The minimum force that can be measured is ~800 nN.

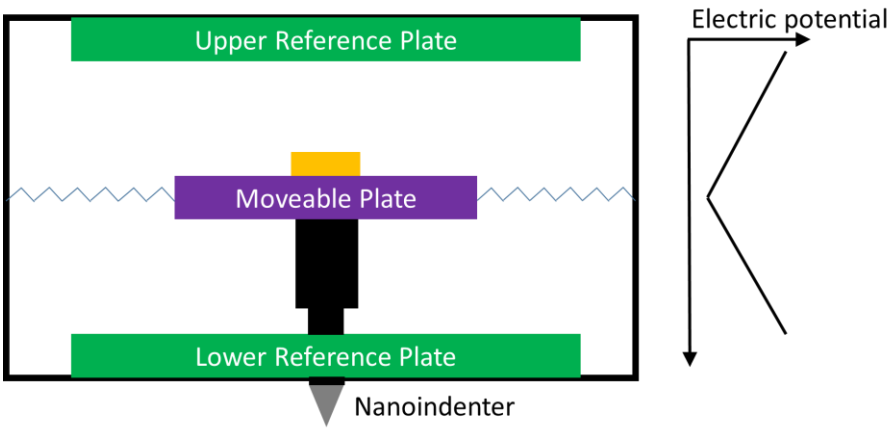

Figure 2.11. *The schematic of the Triboscope© transducer. The moveable plate is suspended with springs. The electric potential profile along the vertical direction is shown on the right. (Redrawn from Ref [23]).*

2.4.2.2. Transducer Calibration

Before experiment, the transducer needs to be calibrated to guarantee correct data acquisition. The calibration includes following steps.

1) *Load a transducer constant file.* The transducer constants include load and displacement scale factors, which converts the measured voltage to load and displacement data. The load and displacement scale factors are calibrated by factory and will not be changed during the following calibration steps.

2) *Update the tare value.* The tare value needs to be updated to check if it is approximately the value given by the factory calibrated value. If not, the indenter may not be correctly installed. Check the indenter installation again.

3) *ADC calibration.* The performance of DSP controller need analog-to-digital convertor (ADC) calibration to calibrate the gains and data acquisition board. The ADC calibration is needed after first transducer installation, but is always performed before experiment to ensure accurate gain settings.

4) *Z-axis Calibration.* The Z-axis calibration is used to calibrate the electrostatic force constant. Every transducer has its own electrostatic force constant, which determines the required electrostatic force for indenter displacement. For large displacement, the relationship between electrostatic force and displacement is nonlinear, thus it is important to perform Z-axis calibration before all experiments. The calibration is carried out by an air indenting experiment. After

calibration, the measured indenter displacement should be close to the programmed displacement time curve, and the measured force should varies within 1 uN.

2.4.2.3. Sample Preparation

Focused ion beam (FIB) is the main sample preparation tool to fabricate sample with specific geometry. The operation procedure in general is similar to regular FIB TEM sample preparation, so the basic FIB preparation steps are not explained in details. A good description of FIB techniques can be found in Ref. [24]. Only the differences are highlighted here.

1) *Perform the regular FIB lift-out*. The preparation steps are same as regular TEM sample lift-out. The final lift-out sample dimension is ~30 um × ~3 um × ~8 um (see Fig. 2.12(a,b)). Considering the final sample (nanopillars or beams) dimension is around 200-600 nm, the lift-out sample provides large enough substrate area for the deformation;

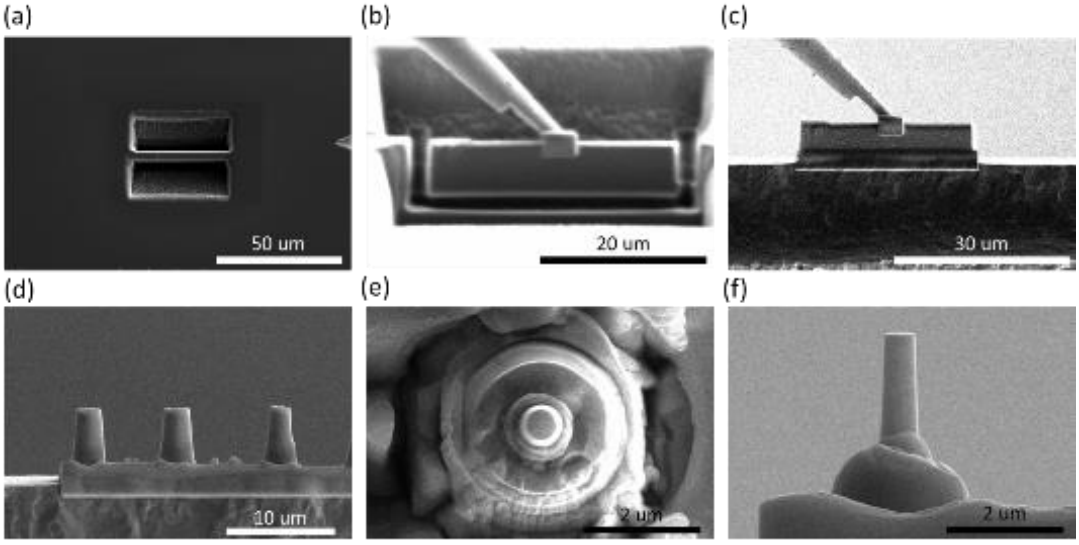

Figure 2.12. *FIB sample preparation procedure. Firstly, trench cut (a) and U-cut (b) to fabricate a ~30 um × ~3 um × ~8 um chunk, which is lifted out and attached to a Molybdenum TEM grid*

(Fig. 2.12 cont.) top with Pt deposition shown in (c). Then the middle parts are cut to allow separation between pillars (d). The nanopillar is gradually milled using annular milling function to 500-600 nm diameter. A top-view and front-view of the final nanopillar is shown in (e) and (f).

2) *Attach the lift-out sample onto the top of molybdenum TEM grid using Pt deposition* (Fig. 2.12(c)). The reason for using molybdenum grid is that it is harder than copper grid, so it is easy to handle in the later steps. Because the bottom surface of lift-out sample is not flat but have a 52 degree inclination, the top of Mo grid is also cut by Ga^+ to have a 52 degree inclination to insure perfect contact between sample and grid (see Fig. 2.13).

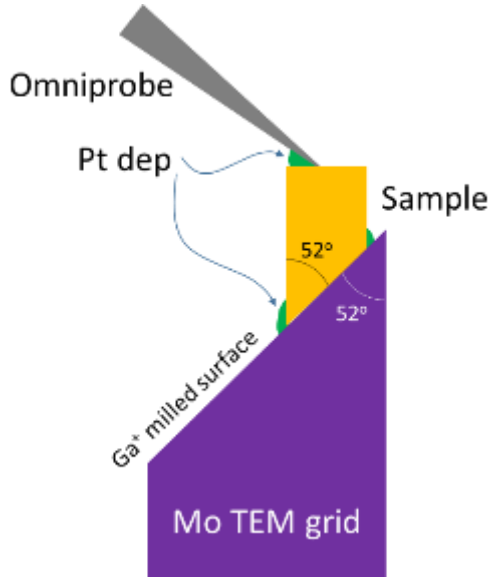

Figure 2.13. *Ga^+ milled Mo TEM grid provides inclined surface in perfect contact with the lift-out sample.*

3) *Annular mill the sample into cylindrical pillar (Fig. 2.12 (e,f)) or mill a lamella (for beam bending experiment)*. In this step, the milling current is gradually reduced from 80 pA to 7.7 pA as the pillar/lamella diameter reduces. The acceleration voltage is kept at 30 keV. Lower voltage will degrade the imaging and milling quality by introducing more astigmatism, so no attempt was made to use lower voltage for milling;

4) *For the beam bending experiment described in Chapter 3, a rectangle hole is cut from the lamella sample at a normal incidence angle*. However, regular FIB machine tilt angle ranges from -10 to 60 degrees which cannot place the lamella at a normal position respect to Ga^+ beam. Thus, the lamella is mounted to a 45 degree SEM sample stage which gives the flexibility to cut a hole out of the lamella at a normal incidence as shown in Fig. 2.14.

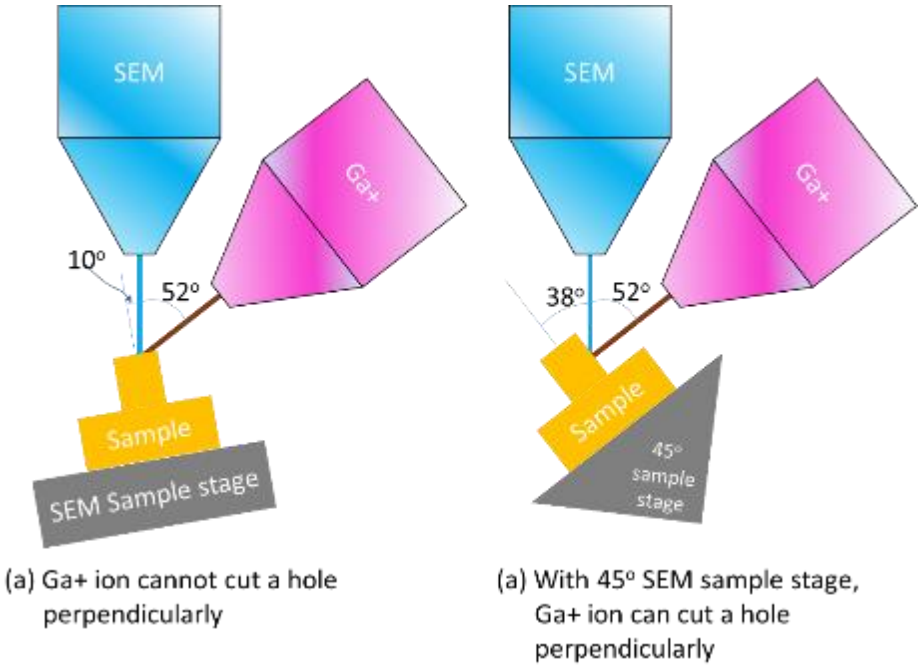

Figure 2.14. *(a) Regular SEM sample stage cannot provide enough tilting angle for perpendicular hole cut using Ga+ beam. (b) A 45 degree SEM sample stage offers the flexibility to orient the sample in a position where perpendicular hole cut is possible.*

5) *Mount on TEM grid*. The Mo grid together with the FIBed sample was glued using crystal bond to a custom-made copper sample mount shown in Fig. 2.15. The copper sample mount was specially designed to fit the PI95 holder and a plateau to glue the Mo grid.

6) Finally, the copper sample was fixed onto the PI95 holder using a screw.

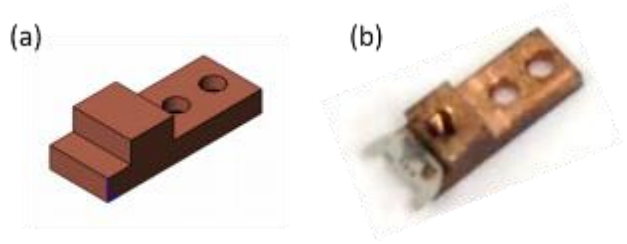

Figure 2.15. *Custom-made copper sample mount. (a) shows the CAD design geometry and (b) is a picture showing Mo grid mounting on the copper sample mount.*

2.5. Evaluation of Nanopillar Compression Tests Using Finite Element Analysis

The nanopillar compression test provides an easy way to access the stress-strain curve of materials. By fabricating a column with uniform diameter, the stress can be easily calculated from measured force. However, several experimental variables may affect the accuracy of stress-strain measurement, such as tapered column geometry induced by FIB annular milling, aspect ratio (pillar height : pillar diameter), and substrate sink-in effect. Here, we systematically studied these influences using finite element analysis (FEA) to guide the experiments. Although there have been studies on the accuracy of nanopillar compression experiments using FEA, they are focused on in situ SEM compression instead of in situ TEM, where a much smaller substrate (2~3 um) is present. Thus, it is still necessary to revisit this issue using FEA.

2.5.1. Finite Element Analysis

We constructed a 3D geometry for FEA simulation using Abaqus standard version 6.13, as shown in Fig. 2.16. The indenter is modeled as an analytical rigid part, which is not allowed to deform. h is the nanopillar height, d is the nanopillar diameter defined at middle height position, θ is the taper angle and L is the substrate height and diameter. In the simulation, the nanopillar diameter d is kept at 550 nm, and L at 2000 nm, which is based on the dimension used for experiments. Taper angle from 0 – 5 degrees and aspect ratio from 2 – 4 are chosen in the simulation. The pillar and substrate are same materials and they are connected by nodes. The bottom surface of substrate is fixed. The surface-to-surface contact is assigned between top surface of nanopillar and indenter and the friction coefficient is chosen to be 0.2 to simulate the diamond and metal interactions. An 8 node hexagonal linear brick is used for meshing. Proper mesh density is selected to reach a convergent stress-strain curve. The materials true stress-strain curve used for simulation is plotted in Fig. 2.16(b), which is reported in Ref. [25] for CoCrFeMnNi HEAs. The measured true stress-strain curve is calculated from the reaction force between indenter and nanopillar and the relative displacement between nanopillar top and bottom. Firstly, the engineering stress σ_E is calculated by the reaction force divided by the nanopillar cross-section area at middle. The engineering strain ε_E is calculated by relative displacement dividied by original pillar length. Then the true stress σ_T and strain ε_T is calculated based on $\sigma_T = \sigma_E(1 + \varepsilon_E)$ and $\varepsilon_T = \ln(1 + \varepsilon_E)$.

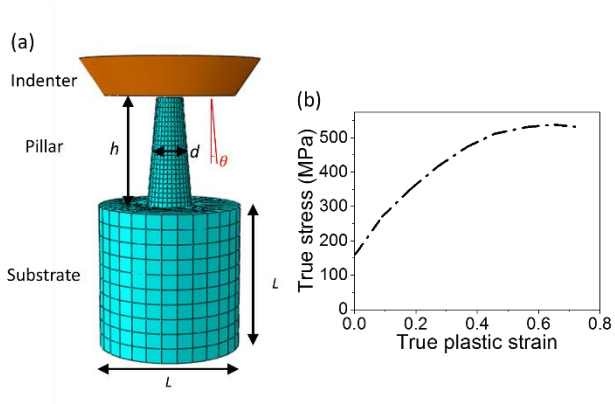

Figure 2.16. *a) The geometry and mesh of the finite element model. h is the nanopillar height, d is the nanopillar diameter defined at middle height position, θ is the taper angle and L is the substrate height and diameter. b) the true plastic stress-strain curve for HEA used in the simulation.*

2.5.2. Aspect Ratio Effect

The aspect ratio (AR) of nanopillar is defined as the ratio between height and diameter *h/d*. In the simulation, three AR 2, 3, and 4 are used to understand its influence on the compression experiment. Figure 2.17 shows the comparison between measured true stress-strain curve and input HEA materials stress-strain curve. The stress-strain curve measured from aspect ratio 2 and 3 is close to the intrinsic curve, while the nanopillar with high aspect ratio 4 buckles (see Fig. 2.17(b)) and significantly influences the stress-strain curve. This indicates that nanopillars with small aspect ratio are suitable for compression testing. However, if the aspect ratio is too small, the constraint between substrate and nanopillar will influence the stress-strain curve. Thus, the aspect ratio 3 is chosen for the experiment.

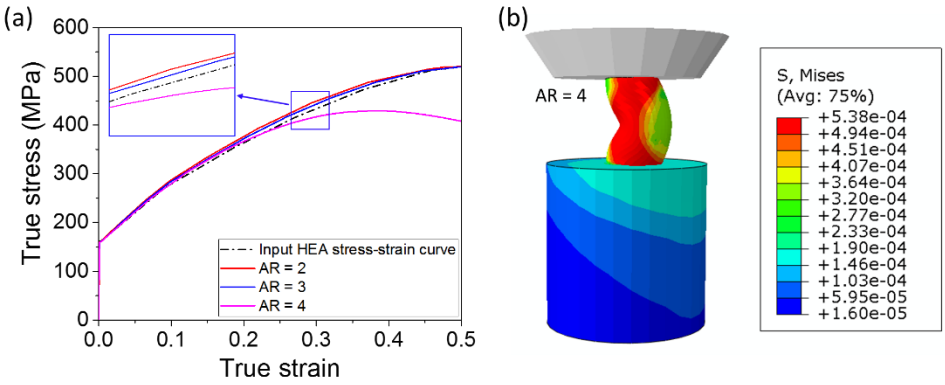

Figure 2.17. *a) Aspect ratio effect on the measured stress-strain curve using nanopillar compression. b) The buckling of nanopillar with aspect ratio of 4.*

2.5.3. Taper Angle Effect

The tapered geometry is an evitable effect from FIB annular milling process. The diameter of nanopillar top is smaller than that of nanopillar bottom. In FEA simulation, stress-strain curves of nanopillars with taper angle from 0 to 5 degree are studied and compared with the intrinsic HEA stress-strain curve. The nanopillar diameter is kept at 550 nm. The result is shown in Fig. 2.18(a). The deviation from the intrinsic curve increases with increasing taper angle, indicating that smaller taper is always preferred. The tapered geometry introduces a stress concentration on nanopillar top, as shown in Fig. 2.18(b). Consequently, the dislocation first nucleates at the nanopillar top and gradually propagate towards the nanopillar bottom. Through carefully controlling Ga^+ beam, a taper angle ~2 degree is achieved in the experiment.

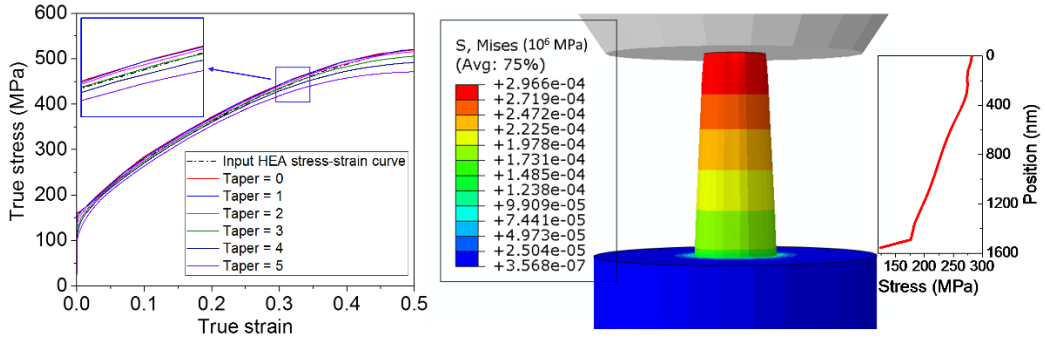

Figure 2.18. *Taper angle effect. a) The comparison between stress-strain curve from nanopillars with taper angles from 0 to 5 degrees. b) The stress gradient induced by the tapered geometry.*

2.6. References

[1] Riecke W, Ruska E. A 100-kV transmission electron microscope with single-field condenser objective. Proceedings of the 6th International Congress on Electron Microscopy1966. p. 19-20.

[2] Zuo JM, Spence JCH. Introduction and Historical Background. Advanced Transmission Electron Microscopy: Imaging and Diffraction in Nanoscience. New York, NY: Springer New York; 2017. p. 1-18.

[3] Zuo JM, Kim M, O'Keeffe M, Spence JCH. Direct observation of d-orbital holes and Cu-Cu bonding in Cu2O. Nature 1999;401:49-52.

[4] Zuo JM, Spence JCH. Imaging and Characterization of Crystal Defects. Advanced Transmission Electron Microscopy: Imaging and Diffraction in Nanoscience. New York, NY: Springer New York; 2017. p. 501-52.

[5] Williams DB, Carter CB. Transmission electron microscopy : a textbook for materials science. 2nd ed. New York: Springer; 2008.

[6] Cowley JM. Electron nanodiffraction methods for measuring medium-range order. Ultramicroscopy 2002;90:197-206.

[7] Zuo J, Vartanyants I, Gao M, Zhang R, Nagahara L. Atomic resolution imaging of a carbon nanotube from diffraction intensities. Science 2003;300:1419-21.

[8] Kolb U, Gorelik T, Kübel C, Otten M, Hubert D. Towards automated diffraction tomography: Part I—Data acquisition. Ultramicroscopy 2007;107:507-13.

[9] Tao J, Niebieskikwiat D, Varela M, Luo W, Schofield M, Zhu Y, et al. Direct imaging of nanoscale phase separation in La 0.55 Ca 0.45 MnO 3: relationship to colossal magnetoresistance. Physical review letters 2009;103:097202.

[10] Kim K-H, Xing H, Zuo J-M, Zhang P, Wang H. TEM based high resolution and low-dose scanning electron nanodiffraction technique for nanostructure imaging and analysis. Micron 2015;71:39-45.

[11] Meng YF, Zuo JM. Three-dimensional nanostructure determination from a large diffraction data set recorded using scanning electron nanodiffraction. Iucrj 2016;3:300-8.

[12] Messerschmidt U, Appel F. Quantitative Tensile-Tilting Stages for High-Voltage Electron-Microscope. Ultramicroscopy 1976;1:223-30.

[13] Martin JL, Kubin LP. Optimum Conditions for Straining Experiments in the Hvem. Ultramicroscopy 1979;4:257-.

[14] Imura T, Saka H. In-situ dynamic observations of dislocation behaviour in metals and alloys by high voltage electron microscopy. Nagoya University, Faculty of Engineering, Memoirs

1976;28:54-112.

[15] Fujita H. Ultra‐high voltage electron microscopy: Past, present, and future. Journal of electron microscopy technique 1986;3:243-304.

[16] Han XD, Wang LH, Yue YH, Zhang Z. In situ atomic scale mechanical microscopy discovering the atomistic mechanisms of plasticity in nano-single crystals and grain rotation in polycrystalline metals. Ultramicroscopy 2015;151:94-100.

[17] Oliver WC, Pharr GM. An Improved Technique for Determining Hardness and Elastic-Modulus Using Load and Displacement Sensing Indentation Experiments. J Mater Res 1992;7:1564-83.

[18] Oliver WC, Pharr GM. Measurement of hardness and elastic modulus by instrumented indentation: Advances in understanding and refinements to methodology. J Mater Res 2004;19:3-20.

[19] Hu Y, Huang JH, Zuo JM. In situ characterization of fracture toughness and dynamics of nanocrystalline titanium nitride films. J Mater Res 2016;31:370-9.

[20] Ohmura T, Minor A, Stach E, Morris J. Dislocation–grain boundary interactions in martensitic steel observed through in situ nanoindentation in a transmission electron microscope. J Mater Res 2004;19:3626-32.

[21] Haque MA, Saif MTA. Application of MEMS force sensors for in situ mechanical characterization of nano-scale thin films in SEM and TEM. Sensor Actuat a-Phys 2002;97-8:239-45.

[22] Warren OL, Asif SAS, Cyrankowski E, Kounev K. Actuatable capacitive transducer for quantitative nanoindentation combined with transmission electron microscopy. Google Patents; 2013.

[23] Maass R. In-situ Laue diffraction on deforming micropillars. 2009.

[24] Giannuzzi LA, Stevie FA. A review of focused ion beam milling techniques for TEM specimen preparation. Micron 1999;30:197-204.

[25] Gludovatz B, George EP, Ritchie RO. Processing, Microstructure and Mechanical Properties of the CrMnFeCoNi High-Entropy Alloy. JOM 2015;67:2262-70.

CHAPTER 3

IN-SITU CHARACTERIZATION OF FRACTURE TOUGHNESS AND DYNAMICS OF NANOCRYSTALLINE TITANIUM NITRIDE FILMS

3.1. Introduction

Nanocrystalline metals and ceramics have attracted considerable interests in the past decade due to the observation and expectation of their high strength, high hardness, and good fatigue resistance[1-13]. However, nanocrystalline materials show low ductility at room temperature[1, 14-16], which limits their applications. Thus, it is very important to understand the fracture mechanisms operating in these systems. In nanocrystalline metals, fracture surface is characterized with dimpled structures whose sizes are larger than the grain size. Hasnaoui et al.[16] used molecular dynamics to simulate the fracture process of nanocrystalline nickel and their results suggested that the formation of local shear planes contributed to the dimpled characteristics on the fracture planes. Shan et al.[14] conducted in-situ tensile straining on nanocrystalline nickel in a TEM. Grain agglomerates were found to form rapidly and frequently ahead of an advancing crack, which was used to explain the formation of dimpled structure. However, there are few reports on fracture mechanisms of nanocrystalline ceramics. It has been proposed that nanocrystalline ceramics consist of a large portion of grain boundary (GB) atoms compared with nanocrystalline metals[17] and the mechanical properties and fracture mechanisms of nanocrystalline ceramics are mainly determined by the amorphous and soft GB phases. GBs act as a preferable place for crack

nucleation and propagation, because of their low atomic density and weak interatomic bonds. Ovid'Ko et al.[18-21] constructed theoretical models to study the deformation and fracture mechanisms of nanocrystalline ceramics. Their models suggested that stress-induced GB sliding and migration serve as the toughening mechanisms. Pozdnyakov and Glezer[22] theoretically examined the fracture toughness of a quasi-brittle nanomaterial and concluded that plastic deformation carried by GBs can significantly increase the fracture toughness of nanocrystalline ceramics. However, so far, there is a lack of experimental evidences on how GBs contribute to the fracture dynamics, how the crack propagates and what toughening mechanisms are behind nanocrystalline ceramics.

Fracture toughness in general serves as an important indicator of the reliability of structural materials. For bulk materials, the method to measure fracture toughness is well-established by following the standard ASTM procedures. However, these methods are not compatible with in-situ monitoring of microstructure using TEM, which requires a thin film. There has also been a lack of a universal methodology to measure the fracture toughness of thin films. Numerous techniques were applied to evaluate the fracture toughness of thin films, including indentation[23], tension[24, 25], and buckling[26, 27]. Those measurement methods for fracture toughness rely on testing thin films deposited on metallic or Si substrates. Because of substrate effect and difficulties in fabricating specimens and applying external stress, there are considerable uncertainties in the measured values[28], and the origin of these variations may be also due to different deformation

and failure mechanisms of thin films. Recently, bending experiment performed in a scanning electron microscope (SEM)[29-31] avoids the subtrate effect, but the deformation and fracture mechanism were not identified. Therefore, it is necessary to measure the fracture toughness and investigate the accompanying deformation and failure mechanisms in thin film using TEMs.

Here, we report a study of fracture mechanism in nanocrystalline TiN thin films based on a new method to evaluate the conditional fracture toughness by in situ testing under TEM. In-situ TEM provides valuable information on the evolution of microstructures during deformation and failure, which is not accessible by other methods including in-situ fracture toughness measurements performed with SEM[29, 32-34] or optical microscopy[35]. Though in-situ TEM has been applied to study crack propagation behavior, the major focus was on nanocrystalline metals[14, 25]. Our study focuses on nanocrystalline TiN to gain important insights into the deformation mechanism of nanocrystalline ceramics. Nanocrystalline TiN thin films were selected for this study because their applications in coatings have attracted great interests due to their excellent mechanical properties, e.g., high hardness and high strength, high chemical stability, low electrical resistivity and high biocompatibility. The current and potential applications of TiN thin films include hard and corrosion protective coatings on mechanical tools and prosthetic devices, anti-erosion coatings on aerospace components, conducting coatings on counter electrode of flexible dye-sensitized solar cell[36], and diffusion barriers in microelectronic components, where fracture toughness is one of the most crucial properties.

3.2. Experimental Methods

Nanocrystalline TiN thin films were prepared by unbalanced magnetron sputtering. The cross-sectional SEM images indicate that the film is ~4.5 μm thick. The technical details can be found in Ref. [27]. The as grown films were characterized by X-ray diffraction and X-ray photoelectron spectroscopy, and the crystal structure and N/Ti ratio were also listed in Ref. [37]. Fig. 3.1 shows the plan-view and cross-section bright field TEM images of the TiN thin films. From the plan-view image, the TiN film has nanometer-sized and equiaxed grains. The distribution of grain sizes in the plan-view direction is measured from ~166 grains, which is shown in Fig. 3.1(e). The average grain size is 48.1 nm. The cross-section image indicates that the film has columnar grains along the growth direction (perpendicular to the film). In order to investigate the deformation and failure mechanism of nanocrystalline TiN films with equiaxed grains distribution, the beam specimen was prepared in the plan-view direction, as shown in Fig. 3.2. The sample was taken from the middle part along the thickness direction of TiN thin films by FIB.

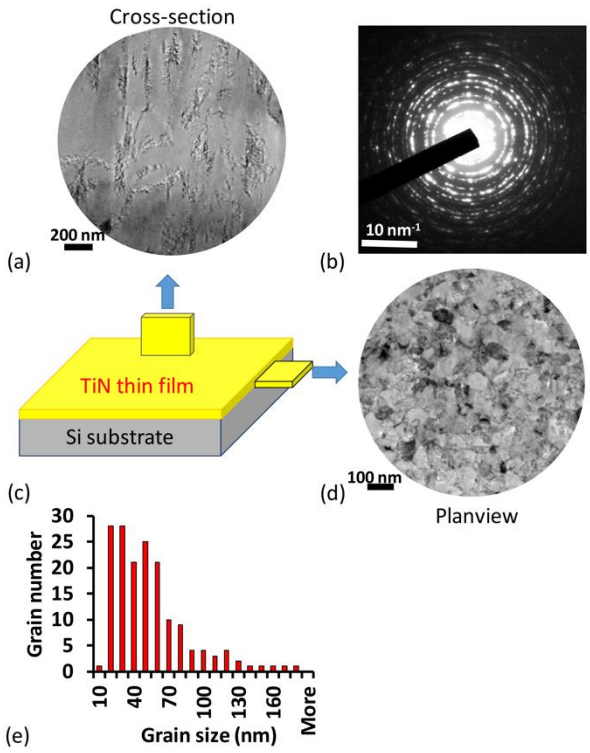

Figure 3.1. *Characterization of TiN thin film specimen. (c) schematic figure of the sample geometry, and corresponding plan-view (d) and cross-sectional (a) bright field TEM images. The selected area diffraction pattern is taken from plan-view sample and shown in (b). (e) The grain size distribution of TiN film in plan-view direction.*

For in-situ fracture toughness measurement, we followed the ASTM E399 three-point bending test standards, and fabricated a beam specimen with the dimensions along horizontal, depth and thickness directions of ~1600 nm×~400 nm×~200 nm, as shown in Fig. 3.2, using a dual-beam FIB (Helios 600i, FEI). The Ga^+ ion beam was controlled from 30 kV and 2.3 nA to 5 kV and 7.7 pA during the fabrication of the beam specimen. There is very few grain overlap along the thickness direction due to the TiN film columnar grain structure (see Fig. 3.1). This is further confirmed by the orientation mapping performed using scanning electron nanobeam diffraction

(SEND) on the beam specimen (see Fig. 3.5(b) and Fig. 3.6(b)). A notch of length ~100 nm at the middle of the beam acts as a precrack for stress concentration and initiation of the crack. The radius of curvature at the notch tip was around 10 nm. The notch was fabricated using 30 kV and 7.7 pA Ga^+ ion beam in FIB. Since the test specimen is made entirely of TiN film, we avoid the substrate effect on the fracture toughness measurement. Also, no microcracks or flaws before fracture testing were observed from TEM imaging.

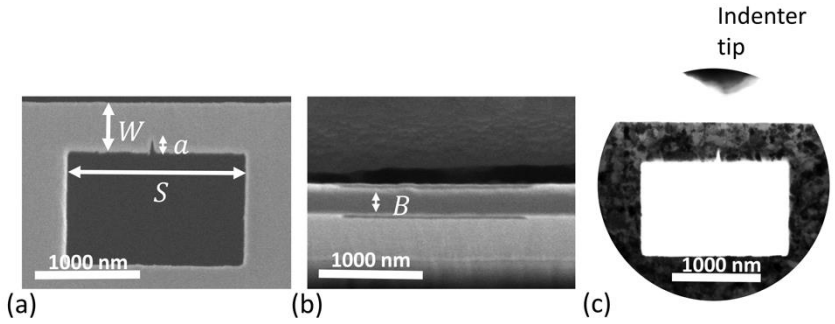

Figure 3.2. *(a) and (b) show the SEM images for a TiN beam prepared using FIB for three point bending test. The sample geometry is as follows: W=~400 nm, S=~1600 nm, a=~100 nm, B=~200 nm. (c) a TEM bright field image of the prepared beam. The contrast is enhanced to show the microstructure of the TiN thin film.*

The bending test was performed using a Hysitron PI95 picoindenter TEM holder equipped with a cube corner diamond indenter. The experiment was carried out in displacement-control mode under 2 nm/s displacement rate. The indenter applied a bending force at the middle of the beam until the crack started to propagate. Ten beams were tested in total.

Finite element analysis software Abaqus 6.13 was used to calculate the conditional fracture

toughness of all ten experiments. In the simulation, the bending test was simulated using a rigid cube corner indenter with tip radius ~45 nm (measured from TEM images) and a TiN beam with an elastic modulus of 395 GPa, Poisson's ratio of 0.21[37], and a yield stress of 7 GPa[38]. The effect of the plastic penetration effect from the cube corner diamond indenter was accounted in the simulation. The beam geometry before bending and mesh used for simulation is shown in Fig. 3.3(a). All the dimensions in the simulation were based on the measurement from SEM and TEM images, including the span, width, thickness of the beam, and the shape of the notch. Boundaries are encastered at the two end surfaces of beams. The experimentally measured upper load marked by arrow (f) in Fig. 3.4(a) at which crack starts to propagate was used to simulate the stress distribution. The stress near the notch tip was used to calculate the conditional fracture toughness based on the stress method in Ref. [39].

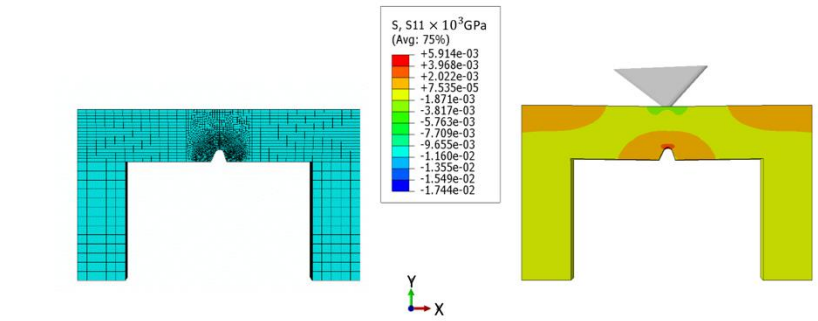

Figure 3.3. *(a) The beam geometry and mesh employed in the FEM simulation. (b)* σ_{xx}*(S11) tensile stress contour plots obtained from FEM simulation at the fracture load, plotted in shaded color.*

The measured K_C is under plane-strain condition, which is attributed to the small plastic zone

size of TiN thin film. The radius of plastic zone at the crack-tip can be estimated as[40]

$$R_f \approx \frac{1}{6\pi}\frac{K^2}{\sigma_{ys}^2} \tag{3.1}$$

where K is the stress intensity factor and σ_{ys} is the yield strength. The critical stress intensity factor K_C for TiN thin film is ~3 MPa·m$^{1/2}$ [23, 27, 41-43], and the yield strength σ_{ys} is ~7 GPa[38]. Thus, the plastic zone size of TiN is about 10 nm. This is further validated from TEM imaging where no obvious dislocation activities near the notch tip were detected (see Fig. 3.4). For the specimen considered to satisfy the plane strain conditions, the ratio of plastic zone size to film thickness should be less than 1/10, which is met if the specimen thickness is larger than 100 nm. In our case, the sample dimension is ~200 nm×~400 nm×~1600 nm, and hence the conditional fracture toughness of the TiN coatings is under plane strain condition which is at the lower limit regardless of the loading modes.

3.3. Results and Discussion

Fig. 3.4(a) (and the associated supplementary video) shows a typical load-displacement curve accompanying with the TEM bright field images corresponding to several data points. No detectable dislocation activities can be observed near the notch tip during the loading. Thus, the plastic zone size should be less than 10 nm, further experimentally confirming the satisfaction of plane strain condition. At point (f), a crack starts to propagate from the notch, which corresponds to the load drop in the measured load-displacement curve. The formation of crack and its propagation are accompanied by a drop in the measured load on the picoindenter. Afterwards, the

crack ceases to propagate due to the compressive stress field induced by the cube corner indenter. Once the crack stops, the measured load stabilizes and further increases upon continued mechanical loading due to the two cantilevers (see Fig. 3.3). The load just before the crack propagation is used in the FEM simulations. The crack growth is stable due to the following possible reasons: (1) As discussed by Jaya and Jayaram in their paper[44], the crack will grow stably due to the clamped beam geometry; (2) the compressive stress field due to the sharp cube corner indenter used in the experiment also stops the propagation of the crack and prevents catastrophic crack growth; (3) the bridging and grain boundary deflection toughening mechanisms together with (2) stabilize crack growth. Using the Hysitron PI95 picoindenter with a data acquisition rate of 500 Hz, we can estimate the crack propagation time by measuring the crack start and stop times, and thus obtain the crack propagation speed in the nanocrystalline TiN film.

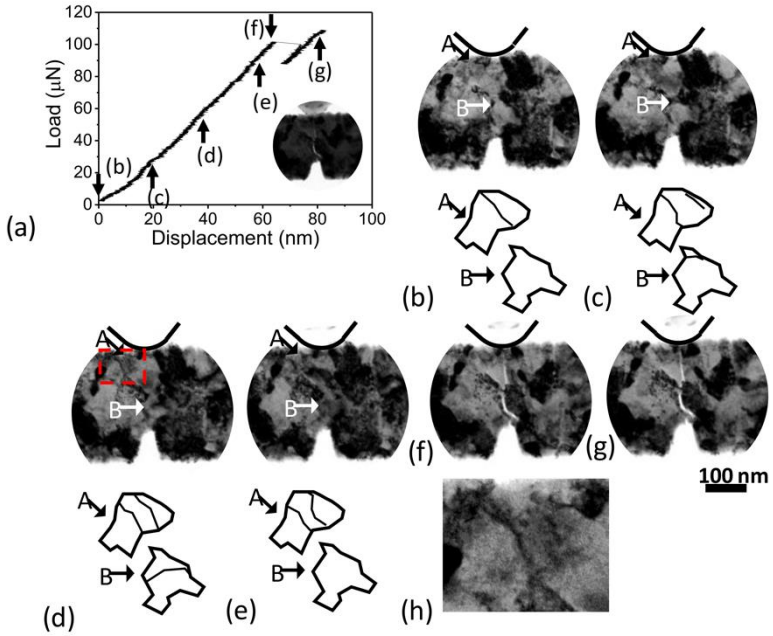

Figure 3.4. *The measured load-displacement curve (a) for beam 7 in Table 3.1 and corresponding*

(Fig. 3.4 cont.) TEM bright field images from (b) to (g). The TEM image with reduced contrast showing the indenter tip in contact with the beam specimen is shown in inset of a). The arrow A and B highlight grains with dislocation activities. The contrast of images in (b) to (g) is enhanced for better visualization. The black line depicts the position of the indenter in (b) to (g). (h) shows a magnified image extracted from the boxed region in (d) in order to show the dislocations clearly.

Ten experiments were performed on the TiN beams with similar geometry. Among all the experiments, failure always occurs near the notch. The beam geometry and calculated conditional fracture toughness by FEM simulation for each beam are listed in Table 3.1. The beam dimensions were measured from SEM images, except the notch length and curvature which were measured from TEM imaging. The resultant average fracture toughness of the TiN specimens is 2.33 ± 0.50 $MPa \cdot m^{1/2}$ which is comparable to literature data as shown in Table 3.2. The fracture toughness that we measured is a mixed mode K_c. Grain boundary deflection, crack propagation on cleavage planes and the misalignment between the indenter and the notch will change the fracture mode from pure mode I fracture to a mixed mode of mode I and mode II fracture. We also calculated the mode II fracture toughness based on the stress method in Ref. [39] as shown in Table 3.1. The value is comparably small compared with mode I fracture toughness, indicating mode I fracture is the dominant fracture mode in our measurement. Thus, the K_I value is effectively fracture toughness K_{IC}.

Table 3.1 Sample geometry and conditional fracture toughness for 10 TiN beams

	Beam 1	Beam 2	Beam 3	Beam 4	Beam 5
Specimen width W (μm)	0.437	0.402	0.426	0.432	0.439
Thickness B (μm)	0.189	0.204	0.196	0.219	0.236
Span S (μm)	1.588	1.605	1.581	1.588	1.591
Crack size a (μm)	0.088	0.111	0.102	0.094	0.082
Fracture load P (μN)	94.700	76.000	92.200	97.100	121.491
Mode I fracture toughness K_I (MPa·m$^{1/2}$)*	2.19	1.79	1.72	1.85	1.95
Mode II fracture toughness K_{II} (MPa·m$^{1/2}$)	0.00198	0.0205	0.0343	0.0324	0.00375
Crack propagation speed (μm/s)	44	46	60	44	35
	Beam 6	Beam 7	Beam 8	Beam 9	Beam 10
Specimen width W (μm)	0.433	0.442	0.417	0.429	0.421
Thickness B (μm)	0.183	0.175	0.182	0.181	0.209
Span S (μm)	1.613	1.621	1.621	1.621	1.613
Crack size a (μm)	0.109	0.106	0.110	0.083	0.071
Fracture load P (μN)	105.850	101.700	90.056	108.380	115.540
Mode I fracture toughness K_I (MPa·m$^{1/2}$)*	2.76	2.77	2.63	3.15	2.48
Mode II fracture toughness K_{II} (MPa·m$^{1/2}$)	0.0978	0.00888	0.0318	0.0252	0.130
Crack propagation speed (μm/s)	129	63	44	74	60

* Since the K_{II} value is small compared with K_I value, the K_I is effectively K_{IC}.

Table 3.2 Comparison of fracture toughness (K_C) of TiN with literature values

Testing method	Film/substrate system	Deposition	Fracture Toughness MPa·m$^{1/2}$	Reference
In-situ TEM, clamped beam bending	TiN/no substrate	PVD	2.33±0.50	This study
IEIC*	TiN/Si	PVD	2.7	[26]
Bending	TiN/Si	PVD	2.6	[36]
	Ti-TiN multilayer	EBPVD	2.9	[37]
Indentation	TiN/Si	PVD	1.19 to 3.3	[23, 38]

* Internal energy induced cracking

The measured conditional fracture toughness shows considerable fluctuations that are dependent on how cracks are formed. Three kinds of crack propagation pathways are observed, namely bridging, intergranular fracture and a mixed mode of transgranular and intergranular fracture.

In the beam 1 (see Table 3.1), the crack bridging process is observed. TEM bright field images before bending and at the failure point and a schematic figure to illustrate the observed grain rotation or bending process are shown in Fig. 3.5. Change in the shapes of grain A and grain B took place during the deformation. The solid and dashed lines represent the shape of grain A and B before and after deformation respectively. Because TEM images were recorded in projection, the shape changes can be due to grain rotation or bending. At the fracture point, the crack initiates

from the notch, and is hampered by grain A, and subsequently starts to propagate on the other side of grain A.

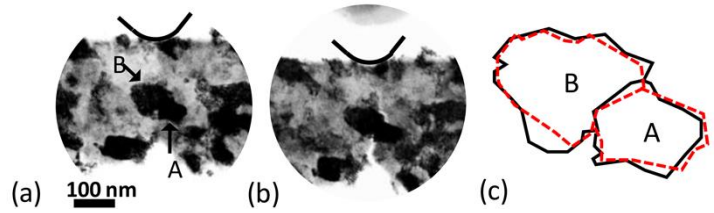

Figure 3.5. *Bright field TEM images recorded before bending (a) and at the failure point (b) for beam 1 in Table 3.1. (c) shows the illustration of the change in the grain shape. The solid line depicts the grain shape before deformation and the dashed line depicts the grain shape after deformation. The contrast is enhanced. A black line is used to depict the shape of the indenter.*

Intergranular fracture in nanocrystalline TiN is observed in beam 8 as shown in Fig. 3.6. In order to better distinguish the grain boundary and grain shape, SEND was performed before the bending test. The scanning region was ~200 nm × ~200 nm with an electron probe size ~2 nm and step size 8 nm. The orientation of each grain can be determined by fitting each scanning nanobeam electron diffraction pattern with simulations from Quantitative Electron Diffraction software (QED). The orientation map and the corresponding diffraction pattern for each grain are shown in Figs. 3.6(a) and (b). The majority of diffraction patterns are from single crystal, indicating that very few grain-overlaps exist along the electron beam direction. From the correlation map color-coded by the crystal orientation of each grain, most of the grains are separated by high angle

grain boundaries. The crack propagation path is shown in Fig. 3.6(c) with a post-mortem bright field TEM image and a schematic figure illustrating the configuration of grains and crack. The crack front proceeds along the GB between G5 and G6, and then diverges into two crack propagation paths (see Fig. 3.6(c)). The crack on the right keeps propagating along the GB of G3 until it meets G2, where the crack is arrested due to large resistance exerted by the grain boundary perpendicular to the crack propagation direction. The crack on the left continues to propagate along the GB of G2, G4 and G5 and keeps being deflected by the GBs. The crack contrast within G2 may be due to the tilted GB alignment between G2 and G1, or transgranular crack growth in G2.

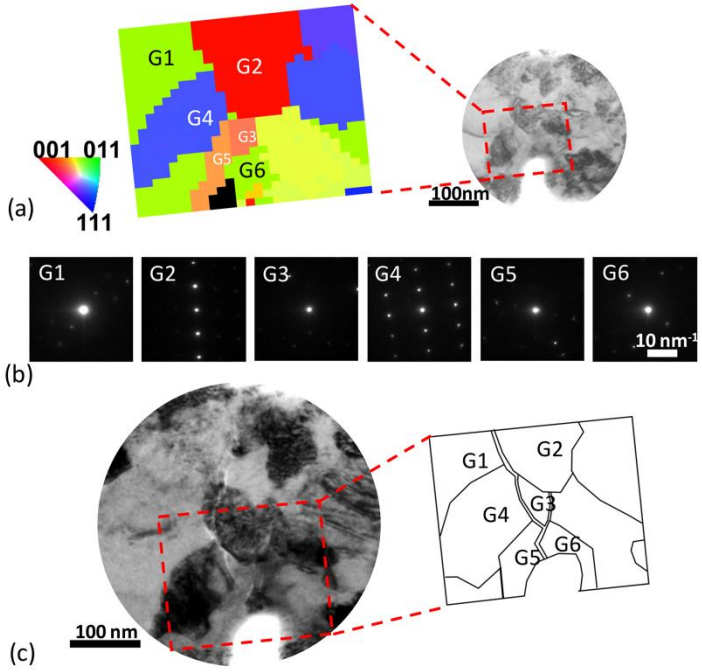

Figure 3.6. *Intergranular fracture mode. (a) Orientation map of beam 8 obtained from the boxed region using SEND. The diffraction pattern for each grain is shown in (b). (c) shows the crack growth path.*

A mixed mode of transgranular and intergranular fracture is shown in Fig. 3.7, corresponding to beam 6 in Table 3.1. SEND is also performed before the bending test with a scanning area of ~360 nm × ~200 nm, probe size of ~2 nm and step size 8 nm. The orientation map and the corresponding diffraction pattern for each grain are shown in Figs. 3.7(a) and (b). The crack first propagates transgranularly in G1 until it meets a triple junction formed by G1, G2 and G4. The triple junction acts as a deflection point and deflects the crack by an angle of 38° since the energy required for intergranular crack is less than that for transgranular crack. The crack then deflects to G4 by an angle of 59° and continues propagating within G4. Based on the SEND patterns for G1 and G4, the cleavage plane can be indexed as (001) for G1 and $(01\bar{1})$ for G4 (see Fig. 3.7 (c)). The grain boundary deflected the crack propagation by 38° and 59° (see Fig. 3.7(c)). The large angle kinks may enhance the fracture resistance and toughens the materials.

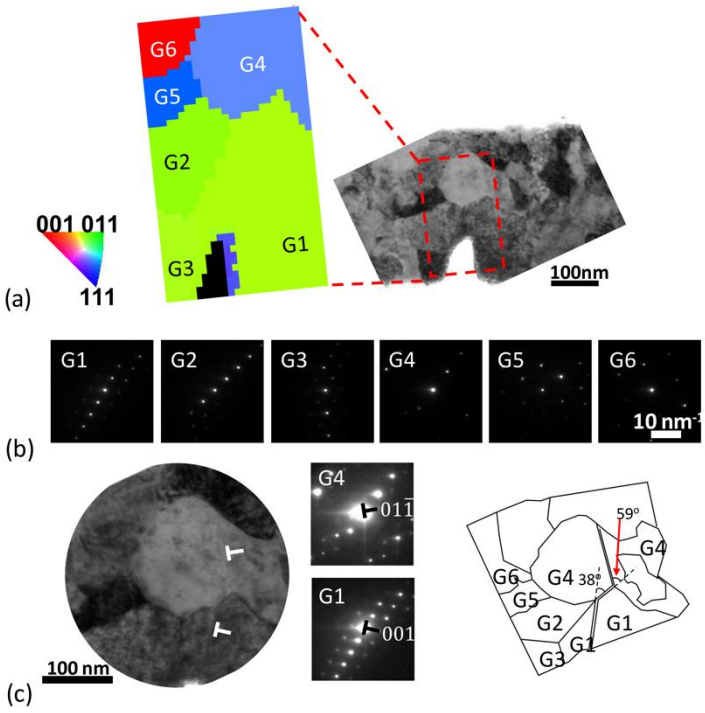

Figure 3.7. *Mixed mode of intragranular and intergranular fracture. (a) is the orientation map of*

(Fig. 3.7 cont.) beam 6 obtained by SEND from the boxed region. The diffraction pattern for each grain is shown in (b). (c) shows the crack growth path. The ⊥ mark denote the directions parallel and perpendicular to the cleavage plane. The inset diffraction patterns for G1 and G4 are contrast enhanced to better show diffraction spots. The normal of cleavage plane points to (001) diffraction spot in G1 and $(01\bar{1})$ *diffraction spot in G4.*

Among the 10 specimens observed, 6 (beam 2, 4, 5, 7, 8, and 10) show cracks predominately propagate along GBs. When the crack initiates in the vicinity of a GB, it will propagate along the GB if the GB has nearly parallel orientation respect to the crack propagation direction. This is consistent with the fact that GB has a lower atomic density and weaker atomic bonds, which facilitates crack propagation due to smaller amount of broken bonds compared with that required for transgranular fracture. Thus, the cracks have a tendency to propagate along GBs. In two cases (beam 5 and 8), the GBs perpendicular to the crack growth direction are observed. Their presence arrests the crack propagation, and forces the crack to proceed along other intergranular paths, or nucleate a new crack on the other side of the blocking grain in a bridging toughening manner, or grow into the grain. When the crack front ends in the grain interior, the crack will start to advance transgranularly (beam 3, 6 and 9) until it meets a GB which will deflect the crack.

For the specimen geometry we used, the stress is partly relieved compared with the thin film on substrate. The thin films grow on the substrate are normally under compressive stress.

Because of this, the measured value by in-situ TEM clamped beam bending method is lower than other method with films bonded to a substrate (Table 3.2).

The crack bridging process occurring in beam 1 (Fig. 3.5) is believed to be consuming more energy than transgranular fracture. Normally transgranular fracture in brittle materials such as ceramics occurs on the cleavage plane, where the crack propagation is unstable and spontaneous once the Griffith criterion is met and the crack propagation speed is very fast. On the other hand, the observed crack bridging process is mainly because an existing crack arrested by encountering a grain with unfavorable orientation such that transgranular cleavage or intergranular crack cannot be initiated. Therefore, grain boundary-mediated mechanisms such as grain rotation or bending are activated to relieve the stress concentration at the crack tip, where a crack is formed on the other side of the two grains to accommodate the deformation of the change of grain shape. This grain boundary-mediated mechanisms accompanying with the formation of a new crack should consume more energy than a simple transgranular cleavage fracture. We succeeded in observing this type of fracture once in our experiment. Further experiments are needed to quantify the toughening associated with it.

The amount of time that crack propagated varies from 2 ms to 6 ms with our measurement resolution at 2 ms. By measuring the length of crack using TEM images, we estimated the average crack propagation speed at $60\ \mu m/s$, with the highest speed at $129\ \mu m/s$ observed in beam 6

with mostly transgranular crack path and the lowest speed at ~44 $\mu m/s$ at beam 1, 4 and 8 with bridging and intergranular crack path. Those specimens showing predominantly transgranular crack (group A, 3 specimens) had an average speed of 88 $\mu m/s$ while specimens involving intergranular cracks (group B, 6 specimens) had an average speed of 52 $\mu m/s$. The relative low propagation speed may be due to the compressive stress field imposed by the sharp cube corner indenter which limits the crack propagation. Also, the toughening mechanisms, e.g. bridging and grain boundary toughening, will also retard the crack propagation. Although the data points are somewhat limited, the trend shows that intergranular fracture and bridging serve as effective toughening mechanisms to retard crack propagation.

Further, dislocation activities are observed during loading as shown in Fig. 3.4 (and the associated supplementary video) as an example. As shown in Fig. 3.4(b), a trapped dislocation existed in the grain marked by arrow A before bending. During bending a dislocation nucleated from the upper right GB. Then the trapped dislocation and newly-formed dislocation together propagated to the lower left direction. The arrow B denotes a dislocation that nucleates, glides through the grain, and finally is absorbed by GBs. This process has been previously observed in nanocrystalline metals[3, 45-48]. The schematic figures below bright field TEM images illustrate these processes. Similar behavior is observed in other test specimens. Dislocation activity tends to be observed near the indenter tip where it is under compressive stress. While in other grains, the recorded TEM images show few or very limited dislocation activities. Previous studies reported that nanograins hinder the intragranular dislocation motion[1, 38]. However, in nanocrystalline

nickel of ~30 nm grain size which is similar to that of our specimens, significant dislocation activities were observed during deformation[48]; by contrast, dislocation activities are much limited in nanocrystalline TiN, only observed in regions near the indenter tip where under compressive stress. Dislocation activities are restricted in ceramics like TiN mostly due to their high Peierls barrier for dislocation slip. In addition, for a notched specimen satisfied plane strain conditions, the area in the vicinity of the notch tip will be under triaxial stress state due to the plastic constraint, and the yield stress will be higher than that under uniaxial stress state[40]. The inhibited dislocation activities seen in our fracture toughness test appear to be consistent with these reasons.

3.4. Conclusion

In summary, we demonstrated a novel method to evaluate the conditional fracture toughness of thin films and to correlate with in-situ study of fracture mechanisms. Nanocrystalline TiN thin films were investigated using this method. Reproducible fracture toughness values were measured in a good agreement with previous reports, indicating high reliability of our method. The fracture toughness that we measured is a local fracture toughness near the notch, dependent on the crack initiation. In-situ TEM bright field imaging reveals three crack propagation pathways, namely bridging, intergranular fracture and a mixed mode of transgranular and intergranular fracture. Also, grain rotation or bending and dislocation sliding contribute to the deformation of nanocrystalline TiN. By comparing the crack propagation speed, it can be concluded that bridging and GB deflection act as toughening mechanisms for nanocrystalline TiN thin films. The influence of stress

state on the dislocation behaviors in nanocrystalline ceramics is discussed, which confirmed the applicability of the classical yielding criteria at submicron size scale. Our methodology is universal and can be applied to other ceramic material systems to evaluate the fracture toughness and study the deformation and failure mechanisms.

Our results show that both the measured fracture toughness value and crack propagation speed are important parameters that can be obtained in in-situ TEM to correlate with microstructure and crack behaviors. Using these data, we can also conclude that GB deflection and bridging hinder the crack growth by reducing the crack propagation speed and act as toughening mechanisms for nanocrystalline ceramics. Our method of measuring thin-film fracture toughness has advantages of avoiding substrate effect, and overcoming difficulties in sample preparation and applying external stress in conventional methods, and gives reproducible and reliable fracture toughness values.

3.5. References

[1] M.A. Meyers, A. Mishra, D.J. Benson. Mechanical properties of nanocrystalline materials, Prog. Mater Sci. 51 (2006) 427-556.

[2] H. Gleiter. NANOCRYSTALLINE MATERIALS, Prog. Mater Sci. 33 (1989) 223-315.

[3] K.S. Kumar, H. Van Swygenhoven, S. Suresh. Mechanical behavior of nanocrystalline metals and alloys, Acta Mater. 51 (2003) 5743-5774.

[4] J. Schiotz, F.D. Di Tolla, K.W. Jacobsen. Softening of nanocrystalline metals at very small grain sizes, Nature 391 (1998) 561-563.

[5] C. Suryanarayana. NANOCRYSTALLINE MATERIALS, Int. Mater. Rev. 40 (1995) 41-64.

[6] M.W. Chen, E. Ma, K.J. Hemker, H.W. Sheng, Y.M. Wang, X.M. Cheng. Deformation twinning in nanocrystalline aluminum, Science 300 (2003) 1275-1277.

[7] J. Schiotz, K.W. Jacobsen. A maximum in the strength of nanocrystalline copper, Science 301 (2003) 1357-1359.

[8] I.W. Chen, X.H. Wang. Sintering dense nanocrystalline ceramics without final-stage grain growth, Nature 404 (2000) 168-171.

[9] M. Dao, L. Lu, R.J. Asaro, J.T.M. De Hosson, E. Ma. Toward a quantitative understanding of mechanical behavior of nanocrystalline metals, Acta Mater. 55 (2007) 4041-4065.

[10] S.C. Tjong, H. Chen. Nanocrystalline materials and coatings, Materials Science & Engineering R-Reports 45 (2004) 1-88.

[11] E.M. Bringa, A. Caro, Y.M. Wang, M. Victoria, J.M. McNaney, B.A. Remington, R.F. Smith,

B.R. Torralva, H. Van Swygenhoven. Ultrahigh strength in nanocrystalline materials under shock loading, Science 309 (2005) 1838-1841.

[12] L. Lu, M.L. Sui, K. Lu. Superplastic extensibility of nanocrystalline copper at room temperature, Science 287 (2000) 1463-1466.

[13] Y. Wang, M. Chen, F. Zhou, E. Ma. High tensile ductility in a nanostructured metal, Nature 419 (2002) 912-915.

[14] Z. Shan, J.A. Knapp, D.M. Follstaedt, E.A. Stach, J.M.K. Wiezorek, S.X. Mao. Inter- and intra-agglomerate fracture in nanocrystalline nickel, Phys. Rev. Lett. 100 (2008).

[15] D. Farkas, H. Van Swygenhoven, P.M. Derlet. Intergranular fracture in nanocrystalline metals, Physical Review B 66 (2002).

[16] A. Hasnaoui, H. Van Swygenhoven, P.M. Derlet. Dimples on nanocrystalline fracture surfaces as evidence for shear plane formation, Science 300 (2003) 1550-1552.

[17] I. Szlufarska, A. Nakano, P. Vashishta. A crossover in the mechanical response of nanocrystalline ceramics, Science 309 (2005) 911-914.

[18] I.A. Ovid'ko, A.G. Sheinerman. Special strain hardening mechanism and nanocrack generation in nanocrystalline materials, Appl. Phys. Lett. 90 (2007).

[19] I.A. Ovid'ko, A.G. Sheinerman. Nanocrack generation at dislocation-disclination configurations in nanocrystalline metals and ceramics, Physical Review B 77 (2008).

[20] I.A. Ovid'ko, A.G. Sheinerman, E.C. Aifantis. Effect of cooperative grain boundary sliding and migration on crack growth in nanocrystalline solids, Acta Mater. 59 (2011) 5023-5031.

[21] I.A. Ovid'ko, A.G. Sheinerman, E.C. Alfantis. Stress-driven migration of grain boundaries and fracture processes in nanocrystalline ceramics and metals, Acta Mater. 56 (2008) 2718-2727.

[22] V.A. Pozdnyakov, A.M. Glezer. Structural mechanisms of plastic deformation in nanocrystalline materials, Phys Solid State+ 44 (2002) 732-737.

[23] G. Wei, B. Bhushan, S.J. Jacobs. Nanoscale fatigue and fracture toughness measurements of multilayered thin film structures for digital micromirror devices, Journal of Vacuum Science & Technology A 22 (2004) 1397-1405.

[24] X.W. Gu, Z. Wu, Y.-W. Zhang, D.J. Srolovitz, J.R. Greer. Microstructure versus flaw: Mechanisms of failure and strength in nanostructures, Nano Lett. 13 (2013) 5703-5709.

[25] S. Kumar, X. Li, A. Haque, H. Gao. Is stress concentration relevant for nanocrystalline metals?, Nano Lett. 11 (2011) 2510-2516.

[26] J.-H. Huang, Y.-H. Chen, A.-N. Wang, G.-P. Yu, H. Chen. Evaluation of fracture toughness of ZrN hard coatings by internal energy induced cracking method, Surf. Coat. Technol. 258 (2014) 211-218.

[27] A.-N. Wang, G.-P. Yu, J.-H. Huang. Fracture toughness measurement on TiN hard coatings using internal energy induced cracking, Surf. Coat. Technol. 239 (2014) 20-27.

[28] S. Zhang, D. Sun, Y.Q. Fu, H.J. Du. Toughness measurement of thin films: a critical review, Surf Coat Tech 198 (2005) 74-84.

[29] B.N. Jaya, V. Jayaram, S.K. Biswas. A new method for fracture toughness determination of graded (Pt,Ni)Al bond coats by microbeam bend tests, Philos. Mag. 92 (2012) 3326-3345.

[30] S. Liu, J.M. Wheeler, P.R. Howie, X.T. Zeng, J. Michler, W.J. Clegg. Measuring the fracture resistance of hard coatings, Appl. Phys. Lett. 102 (2013).

[31] K. Matoy, H. Schonherr, T. Detzel, T. Schoberl, R. Pippan, C. Motz, G. Dehm. A comparative micro-cantilever study of the mechanical behavior of silicon based passivation films, Thin Solid Films 518 (2009) 247-256.

[32] M.G. Mueller, V. Pejchal, G. Žagar, A. Singh, M. Cantoni, A. Mortensen. Fracture toughness testing of nanocrystalline alumina and fused quartz using chevron-notched microbeams, Acta Mater. 86 (2015) 385-395.

[33] S. Johansson, J.Å. Schweitz, L. Tenerz, J. Tiren. Fracture testing of silicon microelements insitu in a scanning electron microscope, J. Appl. Phys. 63 (1988) 4799-4803.

[34] A.A. YAWNY, J.E. PEREZ IPINA. In situ fracture toughness measurement using scanning electron microscopy, J. Test. Eval. 31 (2003) 413-422.

[35] X. Zhang, S. Zhang. A Microbridge Method in Tensile Testing of Substrate for Fracture Toughness of Thin Films, Nanoscience and Nanotechnology Letters 3 (2011) 735-743.

[36] P. Chen, W.-Y. Wu. The use of sputter deposited TiN thin film as a surface conducting layer on the counter electrode of flexible plastic dye-sensitized solar cells, Surf. Coat. Technol. 231 (2013) 140-143.

[37] A.-N. Wang, C.-P. Chuang, G.-P. Yu, J.-H. Huang. Determination of average X-ray strain (AXS) on TiN hard coatings using cos2αsin2ψ X-ray diffraction method, Surf. Coat. Technol. 262 (2015) 40-47.

[38] C.H. Ma, J.H. Huang, H. Chen. Nanohardness of nanocrystalline TiN thin films, Surface & Coatings Technology 200 (2006) 3868-3875.

[39] S. Chan, I. Tuba, W. Wilson. On the finite element method in linear fracture mechanics, Engineering Fracture Mechanics 2 (1970) 1-17.

[40] R.W. Hertzberg, R.P. Vinci, J.L. Hertzberg. Deformation and fracture mechanics of engineering materials, Wiley New York, 1996.

[41] S. Massl, W. Thomma, J. Keckes, R. Pippan. Investigation of fracture properties of magnetron-sputtered TiN films by means of a FIB-based cantilever bending technique, Acta Mater. 57 (2009) 1768-1776.

[42] M.P. Manoharan, A.V. Desai, M.A. Haque. Fracture toughness characterization of advanced coatings, Journal of Micromechanics and Microengineering 19 (2009).

[43] S. Kataria, S.K. Srivastava, P. Kumar, G. Srinivas, Siju, J. Khan, D.V.S. Rao, H.C. Barshilia. Nanocrystalline TiN coatings with improved toughness deposited by pulsing the nitrogen flow rate, Surface & Coatings Technology 206 (2012) 4279-4286.

[44] B.N. Jaya, V. Jayaram. Crack stability in edge-notched clamped beam specimens: modeling and experiments, Int J Fracture 188 (2014) 213-228.

[45] X.Z. Liao, F. Zhou, E.J. Lavernia, S.G. Srinivasan, M.I. Baskes, D.W. He, Y.T. Zhu. Deformation mechanism in nanocrystalline Al: Partial dislocation slip, Appl. Phys. Lett. 83 (2003) 632-634.

[46] H. Van Swygenhoven, P.M. Derlet, A. Hasnaoui. Atomic mechanism for dislocation emission

from nanosized grain boundaries, Physical Review B 66 (2002).

[47] H. Van Swygenhoven, J.R. Weertman. Deformation in nanocrystalline metals, Mater. Today 9 (2006) 24-31.

[48] K.S. Kumar, S. Suresh, M.F. Chisholm, J.A. Horton, P. Wang. Deformation of electrodeposited nanocrystalline nickel, Acta Mater. 51 (2003) 387-405.

CHAPTER 4

GRAIN ROTATION DURING COMPRESSION OF NANOCRYSTALLINE TITANIUM NITRIDE NANOPILLARS

4.1. Introduction

Nanocrystalline ceramics have attracted considerable attention due to the observation of unique mechanical properties, including high fracture toughness[1], high hardness[2] and superplasticity behavior[3]. In particular, nanocrystalline titanium nitrides are widely used for hard and protective coatings on mechanical tools, protective and functional coating in MEMS. Thus, understanding deformation mechanisms in nanocrystalline ceramics is of great importance. Since dislocation activities are retarded due to nanograin structure, grain rotation or grain boundary sliding has been suggested as the possible deformation mechanisms for nanocrystalline thin films. For example, Szlufarska et al.[4] used MD simulations to study the indentation process of nanocrystalline silicon carbide. Their results revealed that grain sliding, grain rotation and intergranular dislocation activity all contribute to the deformation during indentation. However, experimental characterization of nanostructure evolution under the mechanical stress is a challenge, and so far very few experimental studies have been reported related to granular dynamics. In situ nanoindentation performed in a transmission electron microscope (TEM) is a powerful technique for studying the mechanics of nanocrystalline materials[5-8]. This technique was previously used by Jian et al.[9] to investigate the grain size effect on the plastic deformation of nanocrystalline

TiN thin films. While their results indicated grain rotation and grain boundary sliding as the main deformation mechanism of the nanocrystalline thin films, however, the thin-film testing geometry does not allow meaningful measurements of stress-strain curve. Further, the TEM imaging technique employed in their study does not take into account of sample bending during testing.

Here, we provide direct evidence of grain rotations in the nanocrystalline TiN nanopillar under compression using electron diffraction. In-situ electron diffraction experiments were performed in a TEM. Diffraction pattern indexing and nanograin identification were helped by the technique of scanning electron nanobeam diffraction (SEND)[10, 11]. The diffraction experiments were further complemented by in-situ TEM imaging. Together, the experiments reported here provide insights into the mechanism of grain rotation with the help of a classical crystal rotation model.

4.2. Experimental Methods

Nanocrystalline TiN thin film was prepared by the unbalanced magnetron sputtering method. The details of the preparation can be found in Ref. [12]. The thin film was characterized by cross-sectional TEM and the results show that the TiN film has nanometer-sized and equiaxed grains (Figure 4.1, also see Ref. [11]). The distribution of grain sizes in the plan-view direction is measured from 166 grains and plotted in Fig. 4.1(c). The average grain size is 48.1 nm. Selected area electron diffraction pattern reveals grains in random orientations (Fig. 4.1(d)).

To investigate the deformation mechanism of nanocrystalline TiN with equiaxed grains

distribution, the nanopillar specimen was prepared in the plan-view direction, as shown in Fig. 4.1(a). The sample was taken from the middle part along the thickness direction of TiN thin films by FIB.

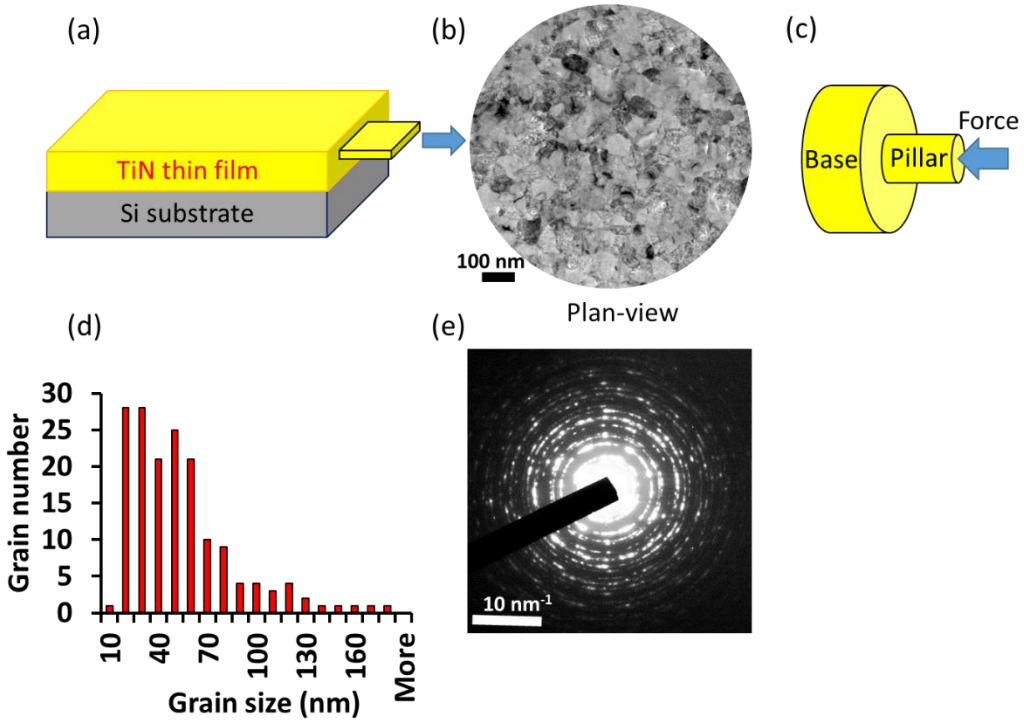

Figure 4.1. *Microstructure of nanocrystalline TiN thin films. (a) TiN thin film was grown on single crystal silicon substrate. (b) The planview sample shows nanometer-sized and equiaxed grains. (c) The average grain size is 48.1 nm. The selected area diffraction pattern is shown in (d).*

The fabricated TiN nanopillars have diameters of ~185 nm and an aspect ratio of ~2:1 as shown in Fig. 4.2(a). The relatively large diameters were used to avoid buckling that occurs under the lateral constraint in nanopillars of smaller diameters. Before compression, SEND was performed to identify the orientation for each grain using the technique described in Ref. [13]. The

electron probe diameter used in SEND was ~2 nm and the scanning area was about 200 nm × 200 nm. After acquiring the data, the diffraction patterns were grouped based on the correlation coefficients between diffraction patterns; these having high correlations are distinguished as a separate grain. Their orientations are further determined using an automatic diffraction pattern indexing procedure based on comparison with calculated diffraction patterns[11]. The orientation map is shown in Fig. 4.2(b) which corresponds to the black squared region in Fig. 4.2(a). 6 grains are marked in the correlation map and their diffraction patterns are color-coded. The neighboring grains of G1, G2, G3 and G4 (others) are characterized as high angle GBs.

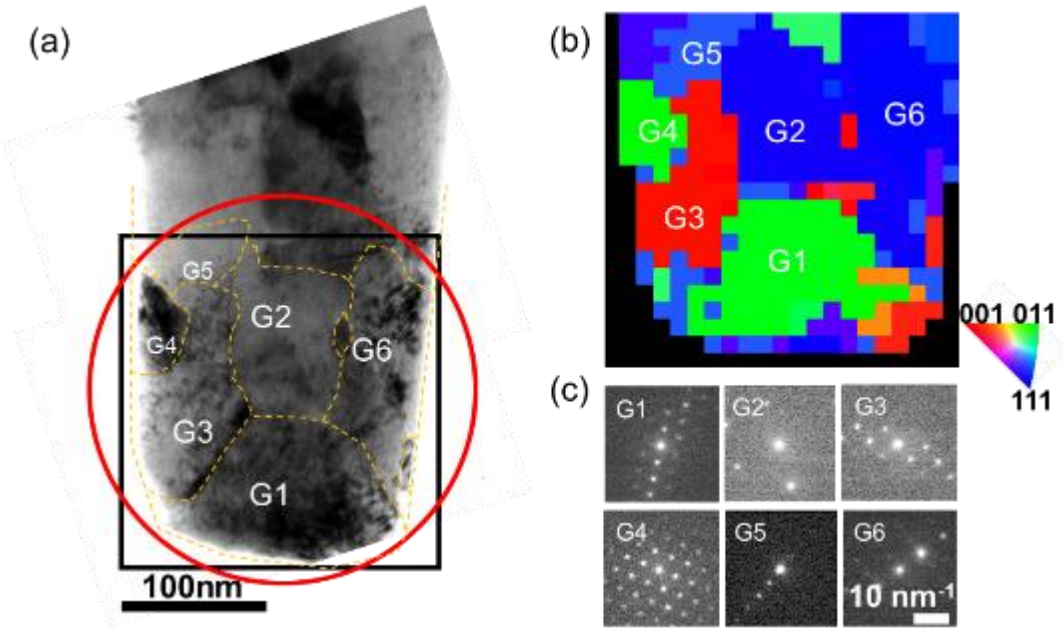

Figure 4.2. *SEND results of TiN nanopillars. (a) shows a 186 nm TiN nanopillars. SEND was performed on the TiN nanopillars before compression. The black square marks the scanning region by SEND. The red circle marks the selected area diffraction region during compression. The orientation of each grain is color-coded and shown in (b). (c) shows the diffraction patterns from*

(Fig. 4.2 cont.) G1-6. The morphology of grains is drawn in dashed line and overlays on (a) to better depict the grain configuration.

In-situ compression experiment was performed using a Hysitron PI95 picoindenter TEM holder in a JEOL 2010 TEM with the LaB_6 emitter. The compression was carried out in the displacement-control mode[14]. In-situ electron diffraction experiment was conducted in the selected area diffraction mode on an area of ~300 nm in diameter (which is marked as red circle in Fig. 2(a)). A charge-coupled-device camera (Orius, Gatan) was used to capture the in-situ diffraction patterns at a frame rate of 30 frames per second. A typical selected area diffraction pattern is shown in Fig. 4.3(b). From the individual grain diffraction patterns identified by SEND (Fig. 4.2(c)), we can identify the corresponding diffraction spots for each grains as marked in Fig. 4.3(b). Thus, by following the movements of individual diffraction spots, we can monitor the grain dynamics under compression using our methods. The diffraction technique provides quantitative information about grain rotation for all the grains within the selected area. This method is universal and can be applied to other nanocrystalline materials.

4.3. Results

The measured stress-strain data is shown in Fig. 4.3(c) for the TiN nanopillar characterized in Fig. 4.2. Sneddon's correction is applied to correct the substrate effect on the displacement

measurement[15]. The stress-strain curve is approximately linear up to 1.5% strain, after which the nanopillar deviated from the linear curve and the nanopillar broke at 2.0% strain.

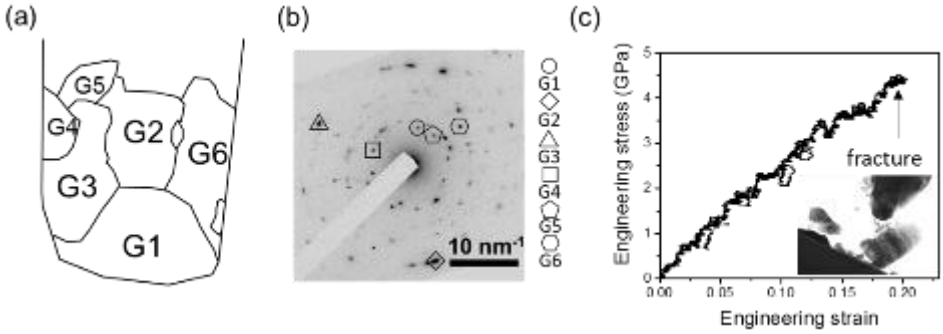

Figure 4.3. *(a) the grain configuration of TiN nanopillar. (b) the selected area diffraction pattern. The contrast is inversed to better show the diffraction spot. Different shapes mark the position of diffraction spots from grain G1 to G6. (c) shows the stress-strain curve measured during experiment. At 0.02 strain, the nanopillar fractured (inset of (c)).*

After acquiring the in-situ diffraction data, Gaussian peak fitting along horizontal and vertical directions was performed to measure the center position of diffraction peaks. By calculating the rotation angle for all diffraction spots in the plane perpendicular the electron beam, the grain rotation was determined for the grains 1, 3 to 6 as marked in Fig. 4.4. These grains on averaged rotated by ~1 degree. The global nanopillar rotation was subtracted from the rotation of each grain. Figure 4.4(b) plots the relative rotation of five grains. The inset figure of Fig. 4.4(b) illustrates the overall nanopillar rotation. This rotation was caused by a misalignment between the indenter surface and the nanopillar top surface. The results show that grain 4 (G4) and G5 show nearly 2 degree difference in the rotation angle in the opposite directions. The rotations for G1 and G6 only

extend to 1.1% and 1.5% respectively because the diffraction spots are too weak to fit afterwards. The G2 diffraction spot overlaps with other spots which cannot be separated, and therefore no attempt on fitting the diffraction spot of grain 2 is carried out. The evolution of rotation angle can be separated into two stages, one from 0 to 0.01 strain, and the other from 0.01 strain to the break point. In the first stage, all the grains show similar rotation behavior since grains are coupled to each other by the GB. After stage one, G3, G4 and G5 undergo different rotation behaviors which are due to the fact that grains are effectively decoupled with each other.

A separate nanoindentation experiment without breaking the TiN pillar was performed. After retracting the indenter, the rotated grains did not fully recover back to its original orientation. This result indicates that the grain rotation also involves plastic deformation of the grains and their GBs.

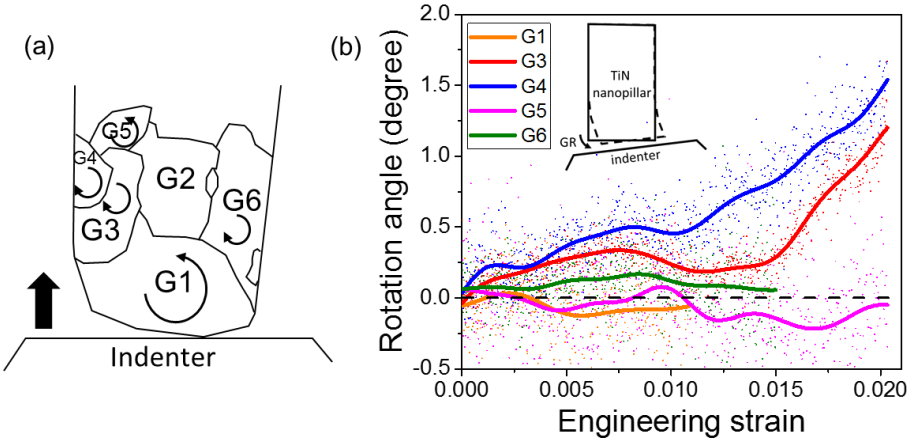

Figure 4.4. *Grain rotation during compression. (a) Schematic showing the rotation direction of measured grains. (b) shows the rotation angle of G1, G3, G4, G5, and G6. G2 was not measured due to the difficulty separating its diffraction spot from other grains. Positive is defined as clockwise direction.*

To further understand the mechanism of grain rotations under compression, real-time TEM imaging observations were performed on a TiN nanopillar with a diameter of 207 nm and aspect ratio of 2.4:1 as shown in Fig. 4.5(a). The displacement rate was 0.1 nm/s, corresponding to a strain rate of 2×10^{-4} s^{-1}. The measured stress-strain curve is shown in Fig. 4.5(a) which is similar to the stress-strain data in Fig. 4.3(c). Multiple stress drops are observed during the compression. To understand the origin of stress drops, image frames before and after the stress drop, which were extracted from the video recording during the compression, are shown in Fig. 5(b, e, h) and (c, f, i). Difference images are used to highlight the changes in the image contrast, which are shown in (d), (g), and (j). Red color in the different image denotes high intensity, while blue denotes low intensity. Figure 4.5(b-d) and (e-g) show the two grain rotation events causing the stress drops. From (b) to (c), the grain marked by the blue arrow uniformly changed the contrast. If the change of contrast was due to dislocations or planar defects such as stacking fault, the contrast will be lines instead of uniform contrast change. Similar contrast change was also observed in another stress drop from (e) to (f). The grain is also marked as blue arrow in the different images. The whole grain has a uniform contrast change, while other grains don't have this kind of contrast change. This is a further evidence indicating the rotation is not caused by the global nanopillar bending.

Limited dislocation activities were also observed as evidenced in Fig. 4.5 (h) to (j),. Before the dislocation activities, a crack formed along the grain boundary. The crack formation is due to

the incompatibility between adjacent grains under large stress 6.83GPa. After the formation of the crack, one grain in the nanopillar shows the contrast change as marked by the arrows in (h-j). The contrast change can be attributed to the dislocation nucleation inside the grains. This could also be caused by the imaging condition change due to grain rotation. The imaging condition change shows GB defect contrast. Thus, during the deformation of nanopillars, the grain rotation and dislocations are cooperatively operating and contribute to the plasticity.

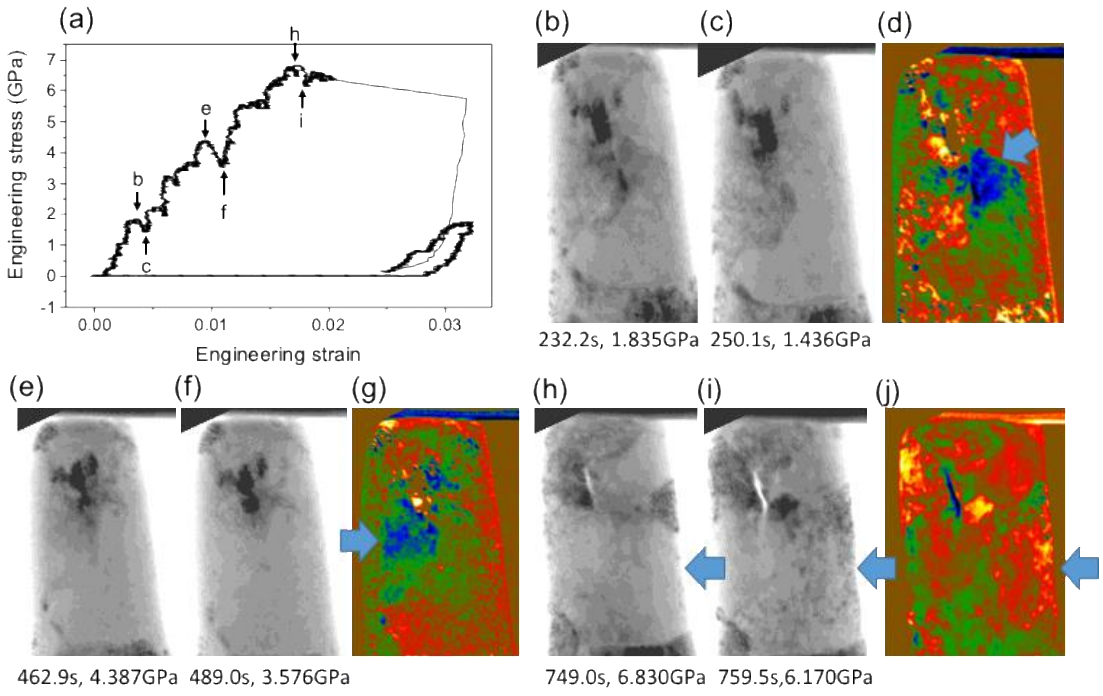

Figure 4.5. *In situ TEM compression of TiN nanopillar under bright field imaging mode. (a) shows the measured stress-strain curve. Multiple stress drops can be observed. Representative image frames before and after stress were marked as arrows on the curve. (b-d) (e-g) (h-j) show the bright field images before the stress drop, after the stress drop and difference image taken from*

(Fig. 4.5 cont.) subtracting the after frame from the before frame. Different images are used to highlight the changes in the image contrast.

4.4. Discussion

The measured rotation angles are too large to be attributed to dislocation sliding. The constraint from the two ends of the pillar cause them not to move freely. Previous reports[16] demonstrated that the slip caused by dislocations gliding on slip plane inside each grain could contribute to the grain rotation in bulk samples. A classical crystal rotation model[17] can be applied to estimate the contribution to the grain rotation from dislocation sliding. The assumption made in this model is that all grains in the polycrystals are subjected to the same macroscopic stress. In each grain, deformation takes place by slip systems with the highest Schmid factor. The rotation angle is determined by $\theta = \langle \boldsymbol{L}, \boldsymbol{L}' \rangle$ where $\boldsymbol{L}'$ and $\boldsymbol{L}$ are compression axes after and before deformation and $\boldsymbol{L}'$ is related to $\boldsymbol{L}$ by $\boldsymbol{L}' = \boldsymbol{L} + \frac{E\epsilon\mu}{G}(\boldsymbol{L} \cdot \boldsymbol{n})\boldsymbol{b}$ where E is the Young's modulus, ϵ is the measured strain, μ is the Schmid factor for active slip system, G is the shear modulus, and $\boldsymbol{n}$ and $\boldsymbol{b}$ are the slip plane normal and slip direction respectively. This model predicts the highest bounds of grain rotation angle since the compatibility across grains is not considered in this model. For TiN with the NaCl structure, the primary slip system for dislocations is $\{110\}\langle 1\bar{1}0\rangle$. Based on the SEND data, the active slip systems, Schmid factor for the active slip systems and rotation angles are calculated as listed in Table 3.1. The calculated rotation angles are all apparently smaller than our measured values. Thus, GB mediated grain rotation is primarily responsible for the

observed grain rotation.

The in-situ diffraction technique is also capable of measuring the lattice strain evolution during deformation. The lattice strain ϵ can be calculated by $\epsilon = \frac{d_{hkl}-d_0}{d_0}$ where the lattice spacing *d* can be obtained using $d = \frac{\lambda l}{r}$, λ is wavelength of incident electron beam, *l* is the camera length and *r* is the distance between the central spot and the diffraction spot. By tracking *r*, the lattice strain along certain (hkl) crystallographic direction for each individual grain thus can be monitored. The lattice strain for G3, G4, and G5 are shown in Fig. 4.6. From 0 to 0.01 strain, the lattice strain of all grains increases, implying the building-up of elastic strain inside grains. After 0.01 strain, the lattice strain surprisingly ceases to increase. For G3, the lattice strain even begins to reduce. The grain rotation and presence of dislocation activities as detected by electron imaging play an important role in accommodating the externally applied strain. The electron diffraction data shows a direct relationship between the alleviation of strain concentration inside the grain and the grain rotation. The grain rotation of G1 and G3-6 are not separated until the strain reaches 0.01. After 0.01 strain, the grain rotation of different grains decoupled with each other and showed a maximum of 2 degrees difference between G4 and G5. The correlation between the decoupling of grain rotation and the alleviation of lattice strain after 0.01 strain indicates that the initial build-up of lattice strain before 0.01 strain can be attributed to the grain rotation and dislocation sliding[5]. It also implies that each individual grain does not bear the same amount of strain that was applied externally. The grain rotation alleviates the lattice strain, which means nanocrystalline ceramics

can collectively undertake larger strain compared with their polycrystalline counterpart. Grain rotation and plastic flow relieve the lattice strain on individual grain substantially. By promoting grain rotation mechanism, it would be expected that the ductility of nanocrystalline materials will be improved. This provides possible guidelines to the design of nanocrystalline ceramics for mechanical applications.

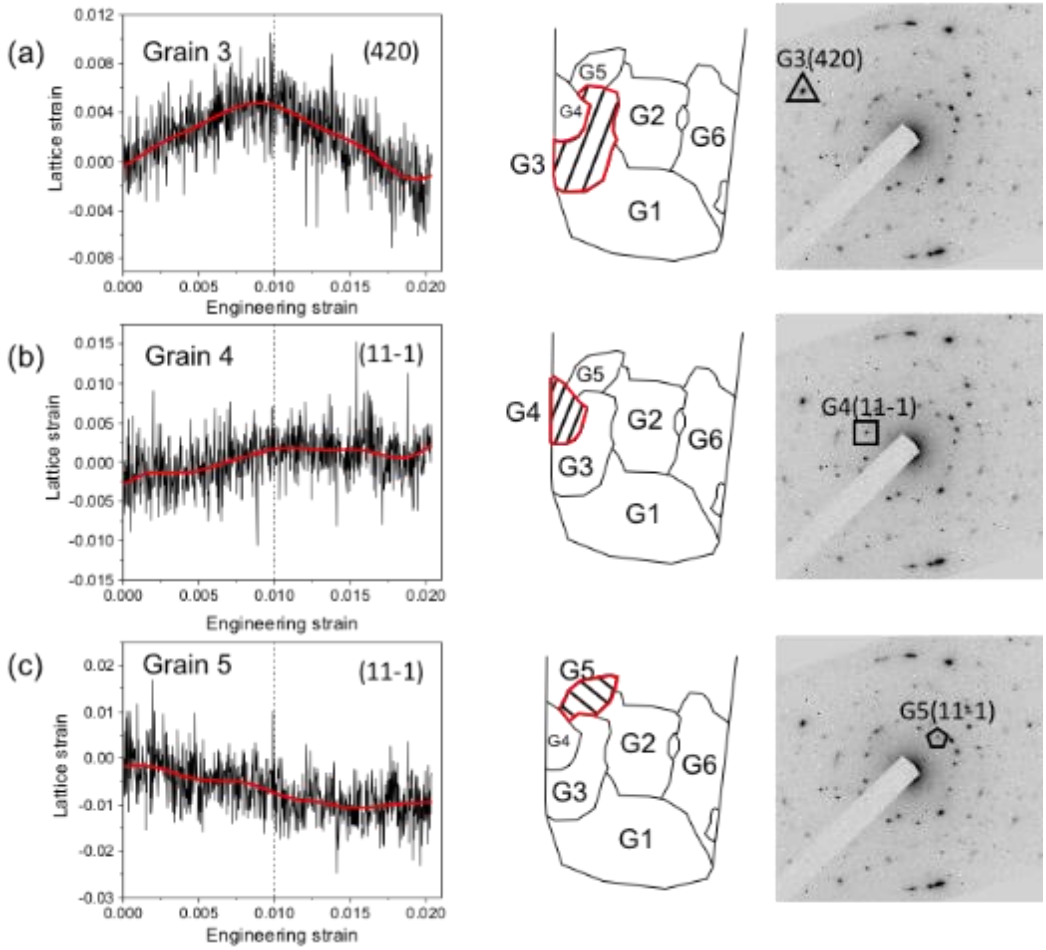

Figure 4.6. *Lattice strain variation during compression. (a), (b), and (c) show the change in the lattice strain during compression. The tracked diffraction spot is indexed.*

Clear dislocation activities were observed in the nanopillar compression experiments at the stage after 0.01 strain. On the other hand, our previous report on in situ clamped beam bending experiment of same TiN beam[19] showed only limited dislocation activities near the pre-fabricated notch. This difference in dislocation activities between the two kinds of experiments can be explained by the different stress conditions. In the clamped beam bending experiment, the beam is under plane strain condition. The plane strain condition limits dislocation activities by imposing a triaxial stress state, and the yield stress will be higher than that under uniaxial stress state. On the contrary, the nanopillar compression testing is under plane stress conditions. Dislocations are easily activated to nucleate and propagate. This difference highlights the importance of stress condition in the operating mechanisms of dislocations.

In Szlufarska's MD simulations [4] on nanocrystalline SiC, they predicted the rotation of grains serving as one of the deformation mechanisms under the compression of a square indenter. Unit and partial dislocations emit from GBs and propagate through the grain are also observed under extensive deformation. Additionally, they concluded that there exists a crossover from intergranular continuous deformation to intragrain discrete deformation at a critical indentation depth. Here, our results provide for the first time confirm those predictions from MD simulation and investigate the mechanism behind the grain rotation. The grain boundary rotation is an important mechanism to accommodate stress. Grain boundary will act as the dislocation nucleation

site. Once the dislocations nucleated, they will propagate within the grains. Dislocations will accommodate the mismatch between the rotation of different grains. The grain rotation is also another mechanism to toughen the materials by increasing its fracture toughness. Since grain rotation will consume energy, it will delay the fracture.

4.5. Conclusion

In summary, the grain rotation is detected during the deformation of nanocrystalline ceramics which is due to the interplay between the sliding of dislocations and GB mediated processes. The grain rotation and plastic flow effectively alleviate the lattice strain. The present experiment for the first time confirmed the prediction of MD simulations for grain rotation and dislocation formation inside the grain in nanocrystalline ceramics. Our methods can be applied to a wide range of nanocrystalline materials, which will unveil the elusive deformation mechanism and shed light on the design and fabrication of nanocrystalline materials with unique mechanical properties.

4.6. References

[1] Wang HK, He DW, Xu C, Tang MJ, Li Y, Dong HN, et al. Nanostructured diamond-TiC composites with high fracture toughness. J Appl Phys 2013;113.

[2] Zhang S, Sun D, Fu YQ, Du HJ. Recent advances of superhard nanocomposite coatings: a review. Surf Coat Tech 2003;167:113-9.

[3] Mohamed FA, Li Y. Creep and superplasticity in nanocrystalline materials: current understanding and future prospects. Mat Sci Eng a-Struct 2001;298:1-15.

[4] Szlufarska I, Nakano A, Vashishta P. A crossover in the mechanical response of nanocrystalline ceramics. Science 2005;309:911-4.

[5] Wang L, Teng J, Liu P, Hirata A, Ma E, Zhang Z, et al. Grain rotation mediated by grain boundary dislocations in nanocrystalline platinum. Nat Commun 2014;5.

[6] Legros M, Gianola DS, Hemker KJ. In situ TEM observations of fast grain-boundary motion in stressed nanocrystalline aluminum films. Acta Mater 2008;56:3380-93.

[7] Hugo RC, Kung H, Weertman JR, Mitra R, Knapp JA, Follstaedt DM. In-situ TEM tensile testing of DC magnetron sputtered and pulsed laser deposited Ni thin films. Acta Mater 2003;51:1937-43.

[8] Shan ZW, Stach EA, Wiezorek JMK, Knapp JA, Follstaedt DM, Mao SX. Grain boundary-mediated plasticity in nanocrystalline nickel. Science 2004;305:654-7.

[9] Jian J, Lee JH, Liu Y, Khatkhatay F, Yu KY, Sub Q, et al. Plastic deformation in nanocrystalline TiN at ultra-low stress: An in situ nanoindentation study. Mat Sci Eng a-Struct 2016;650:445-53.

[10] Kim KH, Xing H, Zuo JM, Zhang P, Wang HF. TEM based high resolution and low-dose scanning electron nanodiffraction technique for nanostructure imaging and analysis. Micron 2015;71:39-45.

[11] Meng YF, Zuo JM. Three-dimensional nanostructure determination from a large diffraction data set recorded using scanning electron nanodiffraction. Iucrj 2016;3:300-8.

[12] Wang AN, Yu GP, Huang JH. Fracture toughness measurement on TiN hard coatings using internal energy induced cracking. Surf Coat Tech 2014;239:20-7.

[13] Hu Y, Huang JH, Zuo JM. In situ characterization of fracture toughness and dynamics of nanocrystalline titanium nitride films. Journal of Materials Research 2016;31:370-9.

[14] Minor AM, Lilleodden ET, Stach EA, Morris JW. In-situ transmission electron microscopy study of the nanoindentation behavior of Al. J Electron Mater 2002;31:958-64.

[15] Sneddon IN. The relation between load and penetration in the axisymmetric boussinesq problem for a punch of arbitrary profile. International Journal of Engineering Science 1965;3:47-57.

[16] Taylor GI. Plastic strain in metals. J I Met 1938;62:307-24.

[17] Sachs G. Plasticity problems in metals. Transactions of the Faraday Society 1928;24:84-92.

[18] Ma CH, Huang JH, Chen H. Nanohardness of nanocrystalline TiN thin films. Surf Coat Tech 2006;200:3868-75.

[19] Hu Y, Huang J-H, Zuo J-M. In situ characterization of fracture toughness and dynamics of nanocrystalline titanium nitride films. Journal of Materials Research 2016;31:370-9.

CHAPTER 5

DIRECT OBSERVATION OF DISLOCATION ACTIVITIES DURING IN SITU TEM COMPRESSION OF HIGH-ENTROPY ALLOYS NANOPILLARS

5.1. Introduction

Dislocations are one-dimensional defects in materials, consisting of an extra crystal plane or a plane of shear which is terminated inside the crystal along a line of atoms. Dislocation motions control the strength of ductile materials, such as metals and alloys. The concept of dislocations was first introduced by Taylor[1], Orowan[2], and Polyani[3] to explain the discrepancies between experimentally observed and theoretically calculated shear strengths required to deform materials. The concept of crystallinity was firmly established in the early 20th century by the works of M. Von Laue, P.P. Ewald, W.H. Bragg, W.L. Bragg and others. At above the same time, experimental observations of slip bands in deformed metals were made and localized and extended defects were invoked to explain the crystal slip. The theory of dislocations in crystal slip was established in three seminal papers published in 1934 [1-5].However, doubts about the existence of dislocations persisted until their direct observations in transmission electron microscope (TEM) in 1950s [6, 7]. The study of dislocations in TEM is based on the characteristic contrast patterns produced by the transmitted and diffracted electron beam under certain imaging conditions. The theory for explaining the dislocation contrast was largely developed by Hirsch, Howie, Whelan and others in the 1960s[8] for the interpretation of those characteristic contrast patterns. A key concept they

introduced is the column approximation to explain the image contrast based on local diffraction. They recognized that the strain field away from the dislocation core changes slowly and the electron scattered from the sample only deviates from the incident beam by a small angle. Thus, image contrast could be produced from local changes in diffraction conditions within a crystal. In regards to dislocations, atoms around dislocation cores are displaced from their equilibrium positions resulting from the near-core strain field. The lattice strain field alters the local diffraction conditions and thus the intensity of diffracted beams. By placing an objective aperture to select a diffracted beam to form images, dislocations can be identified as bright contrast at a medium magnification.

In situ straining stages were invented to observe deformation mechanisms in TEMs. The use of these stages enabled dynamic observations of dislocation motions in metals and ceramics[9-12]. The TEM straining holders have continually been improved, including some that could operate at low or high temperatures. In situ TEM studies were also extended to the study of the behavior of dislocations and their interactions with other defects such as twins, grain boundaries, and interfaces.

Recent progress in the load sensors and transducers has popularized the technique of nanoindentation technique[13, 14] has been widely used for measuring local hardness, elastic modulus, and yield stress of a sample. The force and displacement in a nanoindenter are controlled and measured through a change in capacitance between two reference plates and a movable electrostatic plate attached to the indentor. The indentation experiment could be conducted either in displacement-control or force-control mode. The correlation between mechanical response with

dislocation activities is possible by performing nanoindentation inside a TEM.

Here, we report on the methods that we have developed to achieve a quantitative understanding of dislocation activities by performing indentation of nanopillars in-situ inside a TEM. Hysitron nanoindentation TEM holder was used. The high-entropy alloy (HEA) of $Al_{0.1}CoCrFeNi$ was used as the test sample. HEAs in general exhibit complex, and unexplained mechanical behaviors[15, 16] (Also see Section 1.3). By studying deformation of HEAs in situ, we aim to better understand the deformation mechanisms of HEAs on a fundamental level; the knowledge enables the design of new HEAs to better control their mechanical behaviors.

By observing dislocation activities leading to dislocation slip on a single slip plane in HEA nanopillars using in-situ TEM, a series of yielding events are revealed, including activation/deactivation of dislocation sources, intermittent propagation of dislocation arrays, collective dislocation jumps, and finally slip avalanches with large stress drops.

5.2. Experimental Methods

The $Al_{0.1}CoCrFeNi$ high-entropy alloy (HEA) was fabricated using vacuum induction melting. To reduce porosity in as-cast samples, they were hot isostatic pressed (HIPed) at 1100 °C for 1 h under 207 MPa ultra-high-purity argon pressure. The HIP process consisted of several steps. First the samples were placed in a HIP vessel, which was evacuated to 10^{-6} Torr (10^{-4} Pa) and filled with the ultra-high purity argon next to the atmospheric pressure. Then the temperature in the chamber

was increased to 1100 °C at a heating rate of 15 °C/min, with a simultaneous linear increase in the argon pressure to 207 MPa, and the samples were soaked at 1100 °C, 207 MPa for 1 h. Finally, the furnace power was shut down, the samples were cooled down to 500 °C under the argon pressure of 207 MPa, followed by the pressure release to 101 kPa (1 atm) and cooled to room temperature. The mechanical properties of the $Al_{0.1}CoCrFeNi$ HEA was characterized and reported in Ref [17]. To characterize the microstructure of HEA, electron backscattered diffraction (EBSD), energy-filtered nanoarea electron diffraction, scanning electron nanoarea diffraction (SEND), dark-field and bright-field imaging in a transmission electron microscope (TEM), and atom probe tomography (APT) were conducted.

Our experimental design was to use HEA single crystal nanopillars of selected orientations for studying crystal slip deformation. After experimenting with several orientations, we decided on … which also simplifies the interpretation of dislocation contrast by limiting the operating dislocations to one slip system. A focused ion beam (FIB) microscope operated with Ga^+ ions at 30 keV and a final milling current of 7.7 pA was used to structure the nanopillar samples with a diameter of 500-600 nm. These diameters were selected based on experiments performed on multiple nanopillars of different sizes ranging from 160 nm to 700 nm. We found that if the nanopillar diameter was too small, the compression easily bent the nanopillar due to the constraint imposed from the substrate and the indenter. The pillar bending had adverse effects on imaging by changing the imaging condition, which made the observation of dislocations exceedingly difficult. On the other hand, if the nanopillar was too large, the electron penetration through the sample was

low. The dislocation contrast was lost in large diameter pillars due to the low signal and increased image noise from multiple inelastic scattering.

To identify the orientation of grains in the polycrystalline HEA sample, electron backscattered diffraction (EBSD) was performed in a SEM (JEOL 7000F Analytical SEM, JEOL). The sample for the EBSD analysis was polished using diamond lapping films and finally polished with 0.05 μm colloidal silica suspension using a vibratory polisher. As shown in Fig. 5.1 (a), three grains with the pillar axis along [116], [103], and [647] were identified by EBSD, and they give rise to multiple slip, double-slip, and single-slip planes, respectively. After EBSD characterization, the grain with single slip orientation [647] was selected to produce HEA nanopillars. The [647] single slip system was chosen for the following reason. Instead of dislocation moving on multiple slip planes, dislocation slips primary occur on the (1-11)[0-1-1] slip plane. This greatly simplify the observation of dislocations by converting a 3-dimensional dislocation observation problem to a 2-dimensional problem.

Focused ion beam (FIB) (Helios 600i, FEI) was used to fabricate nanopillars. Figure 5.1 (b-d) show the fabrication procedure. The specimen was first lifted out from the grain and attached to the top of Molybdenum TEM grid with Platinum deposition. Then multiple nanopillar samples were milled using annular milling method with 30 keV and 7.7 pA to reduce the surface damage. The side view and top view morphology of nanopillar are shown in Fig. 5.1 (e) and (f).

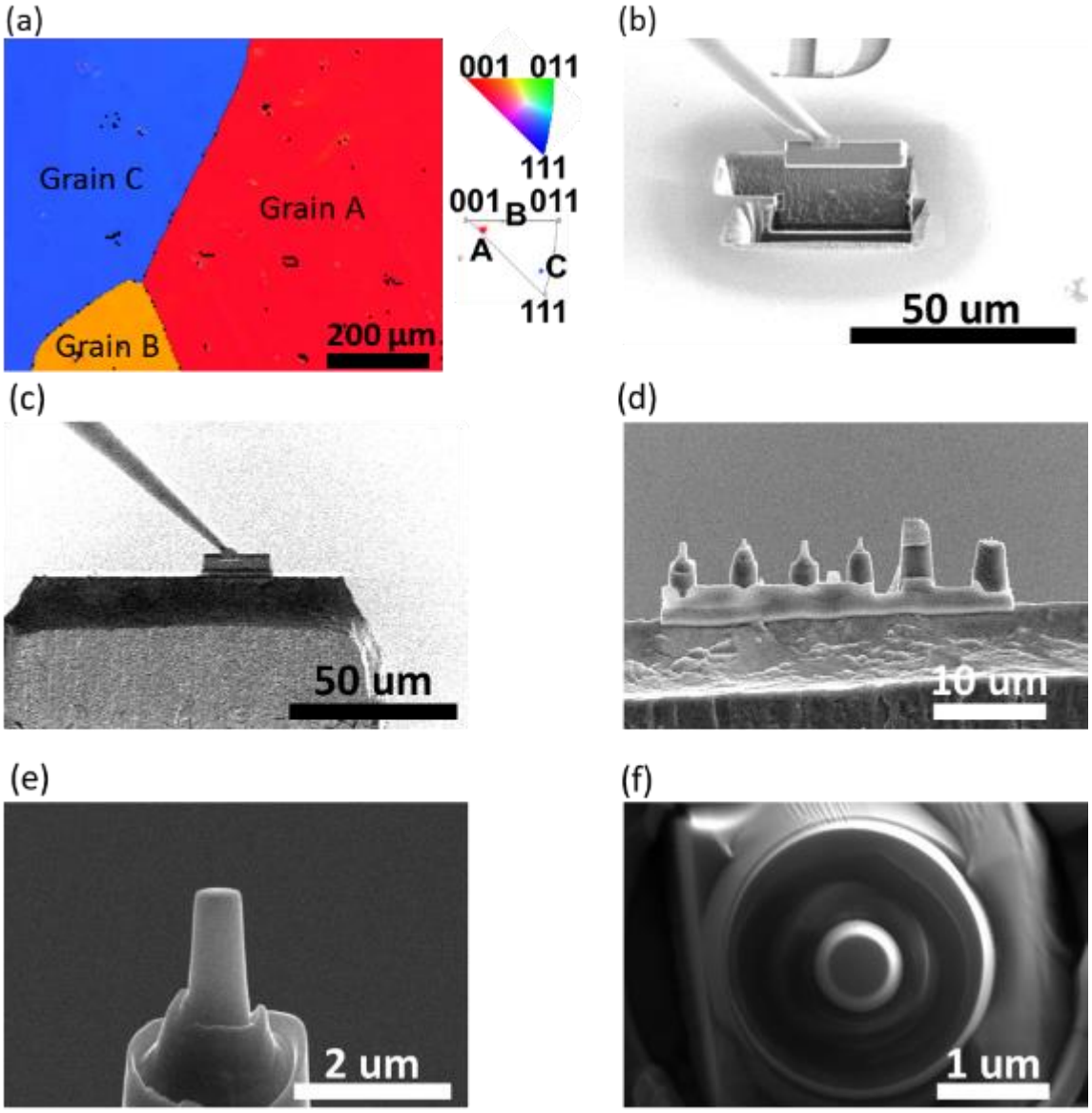

Figure 5.1. *Sample preparation procedure of HEA nanopillars (a) An EBSD orientation map obtained from the polycrystalline HEA sample with three grains, marked as A, B, and C corresponding to the [116], [103], and [647] grain orientations. The inverse pole figure and color map for orientation are shown in the inset of a). (b) Use Omniprobe to liftout HEA sample. (c) attach the HEA sample to the top of a Molybdenum TEM grid. (d) nanopillars after annular milling. (e) and (f) show the side view and top view of HEA nanopillar.*

In situ compression tests of the HEA nanopillars were performed using a Hysitron picoindenter (Hysitron PI95 TEM holder, Hysitron) equipped with a 2 μm flat punch diamond indenter in a JEOL 2010 LaB_6 TEM (JEOLUSA, Boston) operated at 200 keV. The compression tests were performed in the displacement-controlled mode with the displacement rates of 0.5 - 1.5 nm/s, resulting in a strain rate of $\sim 1 \times 10^{-3}$ /s. The load, displacement, and time data were read out at 500 Hz. A video of each test was recorded using a charge-coupled device (CCD) camera (Gatan Orius, Gatan) with a resolution of 720×480 pixels and readout at 10 frames per second. We carefully tilt the nanopillars inside TEM to have the best projection image respect to the electron beam. The imaging condition of the pillar we selected is bright field TEM imaging mode under two beam condition where the (111) reflection is excited. Since only dislocations with Burger's vector [0-1-1] are activated, the $\mathbf{g} \bullet \mathbf{b} = 0$ condition is not satisfied and thus all operating dislocations are observable. The zone axis is [-312], which gives clear dislocation contrast. In summary, the optimum conditions for in-situ TEM are nanopillars with single slip orientation [647], size between 500 nm to 600 nm, and bright field imaging mode along the [-312] zone axis (see Fig. 5.2).

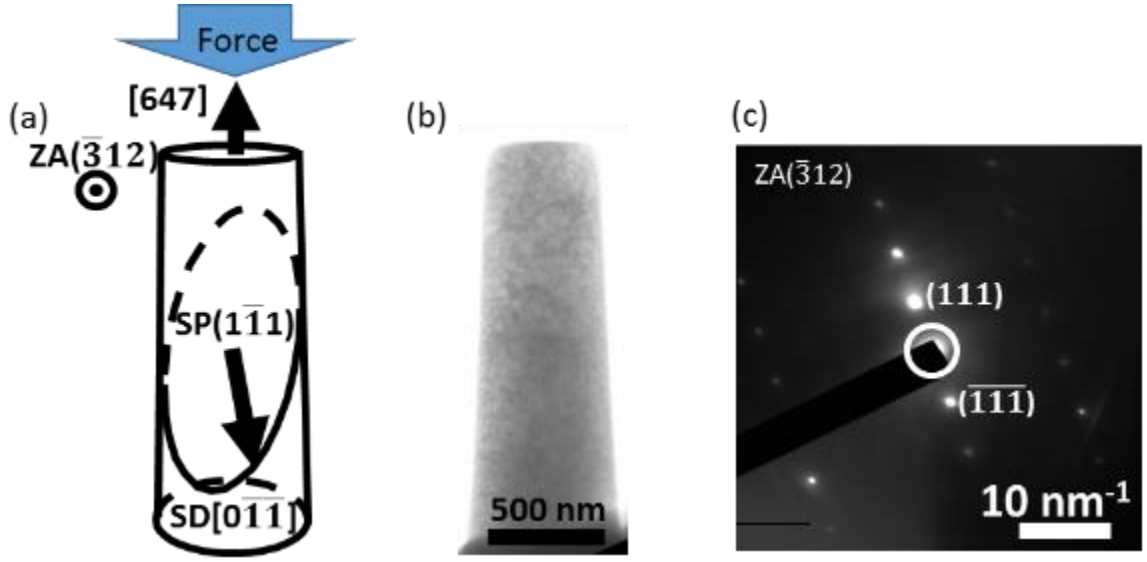

Figure 5.2. *Imaging condition of HEA nanopillar. (a) A schematic showing the geometry between compression axis [647], zone axis [-312], slip plane (1-11), and slip direction [0-1-1]. Slip plane and slip direction are abbreviated as SP and SD in the figure. (b) shows a bright field TEM image of a 512 nm nanopillar. The diffraction pattern is shown in (c). The (111) diffraction spot is excited.*

5.3. Results and Discussion

To characterize the nanopillar microstructure before deformation, we recorded dark-field images of a 230 nm (116)-oriented pillar mounted on a double tilt TEM holder under different two beam diffraction conditions. Figure 5.3 (a-c) show the dark-field images of the pillar using the (022), (02-2), and (200) reflections. Tweed-like features are observed; such contrast is absent in pure metals [18]. The width of the tweed-like contrast is of few tens of nm. Interestingly, the direction of the tweed-like contrast changes with the reflection used for dark-field imaging. Fast Fourier Transformation (FFT) of the tweed-like contrast (inset of Fig. 5.3 (c-e)) shows clear FFT

streak, which is always perpendicular to the direction of reflection used for the dark-field imaging. Figure 5.3 (d) shows a bright field image of the same pillar with no tweed-like contrast nor FFT streak. The image was recorded using the transmitted beam under the same imaging condition as Fig. 5.3 (a) where the (022) reflection was excited at the two beam diffraction condition.

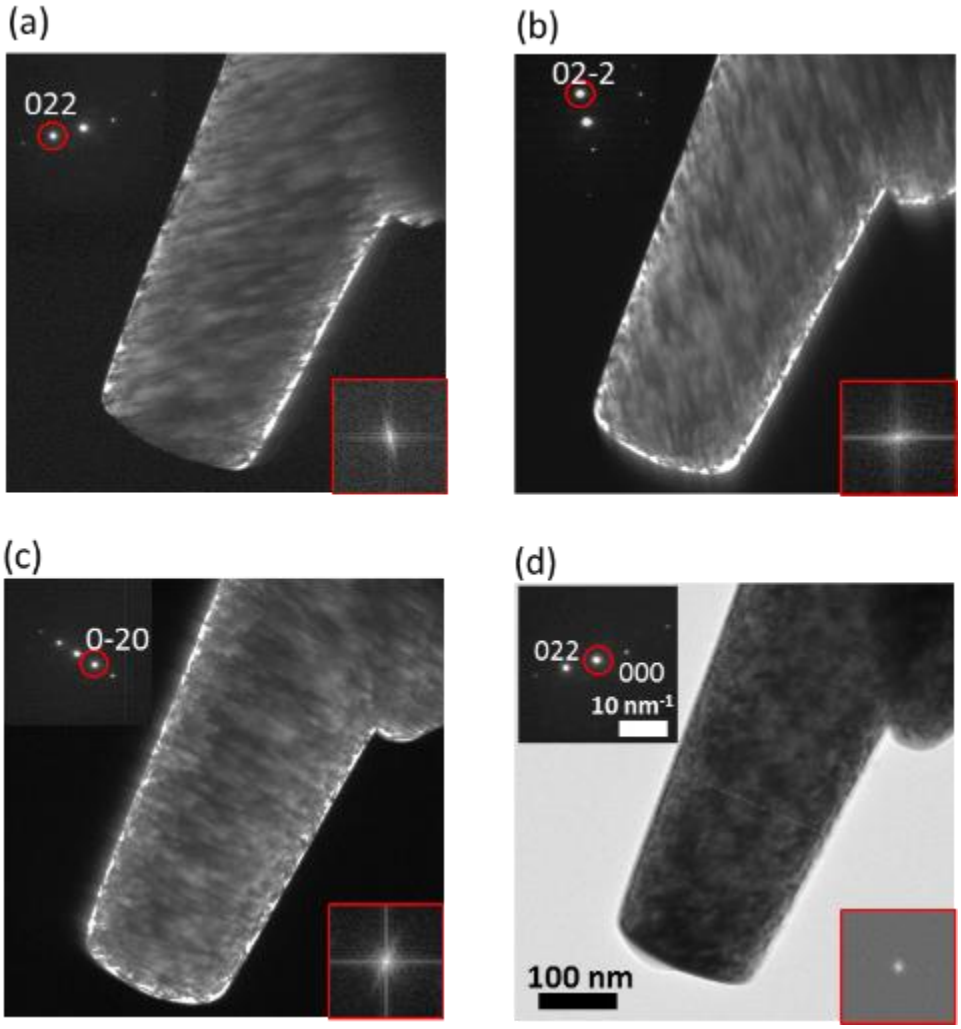

Figure 5.3. *Characterization of the HEA nanopillar of specific orientations. a-c) Dark-field images of the pillar recorded using the (022), (02-2), and (200) reflections under the diffraction conditions shown in the insets. d) A bright field image of the same pillar with no tweed-like contrast nor FFT streak.*

In order to understand the structural origin of the tweed-like contrast, scanning electron nanodiffraction (SEND) technique was employed to analyze the local crystal structures before the compression test. The principle of this technique was described in Ref. [19]. Briefly, a focused probe of ~5 nm is scanned across the nanopillar using the illumination deflection coils. At each probe position, a diffraction pattern is recorded using a CCD camera. The scanned region in Fig. 5.4 (a) is ~100 nm × ~100 nm using a step size 5 nm and 20x20 scanning points. Fig. 5.4 (b) shows one of diffraction patterns acquired from SEND. By integrating the intensity from each diffraction spot, the intensity sum from (0-20), (0-2-2), and (00-2) for every single diffraction pattern is then mapped and shown in Fig. 5.4 (c-e), respectively. Tweed-like contrast similar to Fig. 5.3 (a-c) was also observed in these images. To extract the structural information from regions of different tweed-like contrast, the diffraction patterns from two tweed regions (one with white contrast DP4 and one with black contrast DP3 marked by two yellow circles) were averaged. Then the difference image was obtained by subtracting the averaged diffraction pattern from one another to highlight the difference. Clear intensity difference in the diffraction spots indicates the orientation difference between the two regions of different tweed contrast. Quantitative Electron Diffraction software developed by Zuo at University of Illinois is employed to index the diffraction patterns from region DP3 and DP4. The indexing results are (0, -0.00999, 0.99995) for DP3 and (0, 0.01501, 0.99989). The orientation difference between region DP3 and DP4 is ~1.4 degrees, indicating the existence of low-angle grain boundary (LAGB) in HEAs.

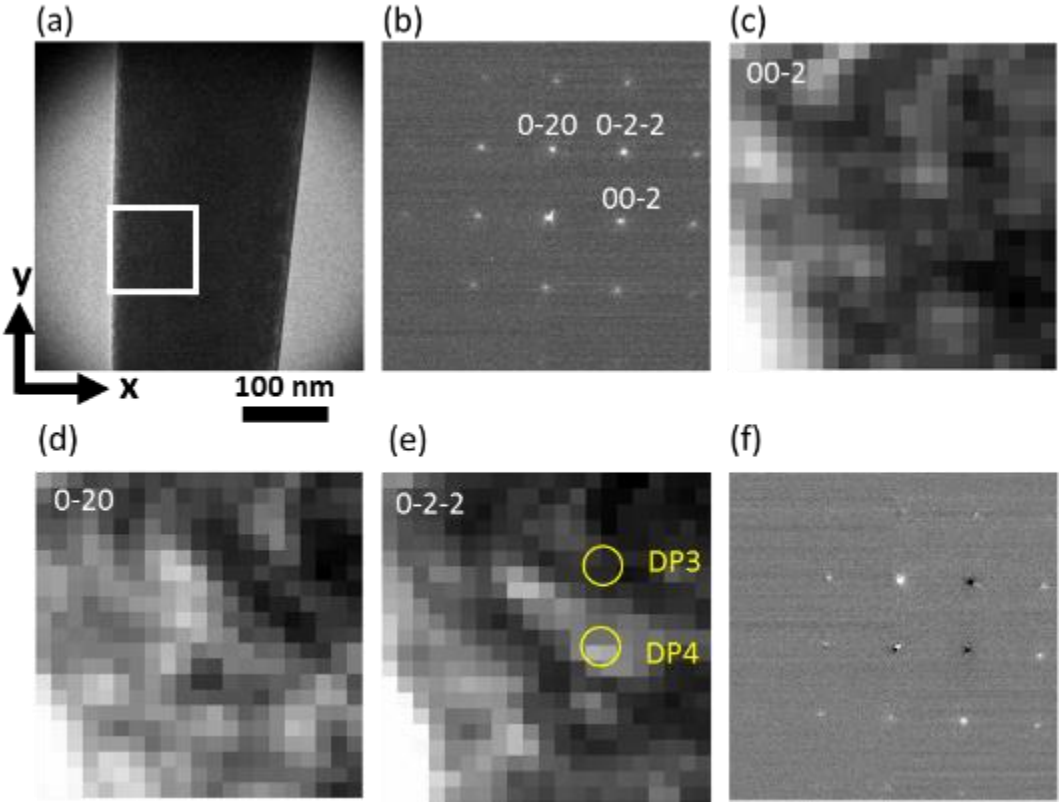

Figure 5.4. *Determination of low-angle grain boundary. (a) A TEM image of the nanopillar sample showing the region ~100 nm × ~100 nm scanned by the nanobeam with a step size 5 nm and 20x20 points. (b) One of diffraction patterns acquired from the SEND patterns. The intensity sum of diffraction spot (00-2), (0-20), and (0-2-2) for every single diffraction pattern is then mapped and shown in (c-e). (d) shows the difference image of DP3 and DP4.*

Atom probe tomography (APT) is used to characterize the composition distribution and defects, including the existence of low-angle grain boundaries. The APT sample were prepared using a site-specific FIB lift-out procedure. The sample was lifted out from the interior of a grain. ATP was conducted on a LEAP 4000X HR instrument (Cameca) operating in laser mode with a

set-point temperature of 30 K, a 65 pJ laser energy, a 125 kHz repetition rate and a detection rate of 0.5%. 3D atom maps of HEA APT sample are shown in Fig. 5.3. Clear evidence for high yield rate in a planar region is obtained as shown in the 5 nm slice of atom maps. The average separation distance between planes is ~20 nm which agrees with dark-field imaging and SEND result. This suggests that low-angle grain boundaries exist in the HEA nanopillars.

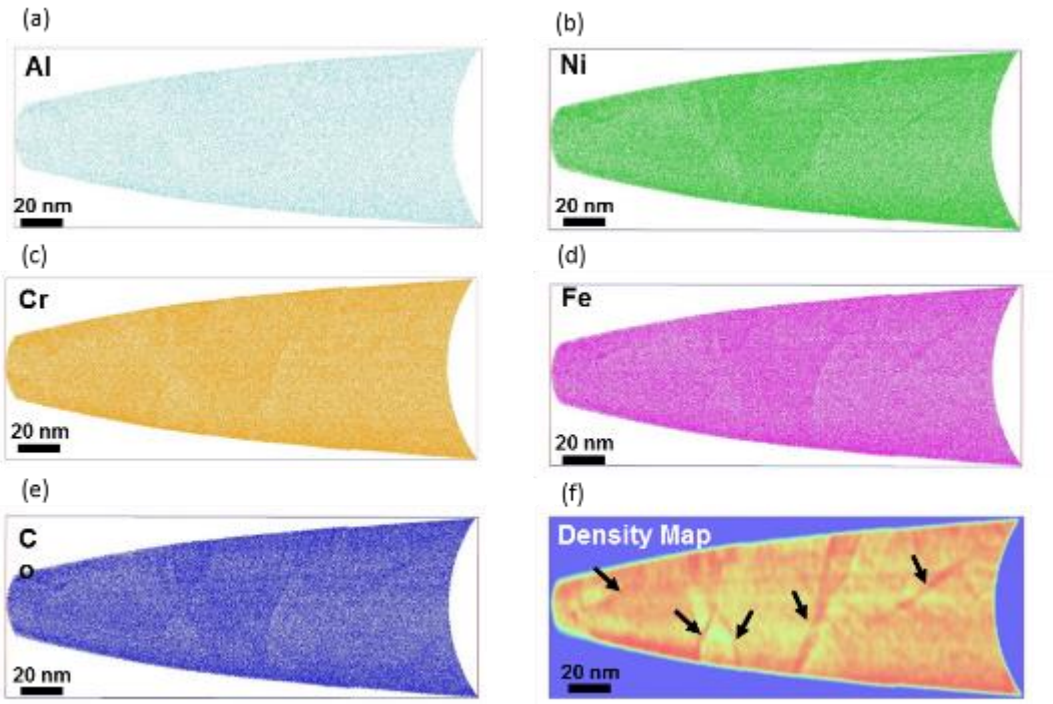

Figure 5.5. *Elemental atom maps containing multiple LAGBs. The black arrows in (f) mark the position of low angle grain boundaries.*

Based on the observations made from dark-field imaging, SEND and APT, it can be concluded that low-angle grain boundaries exist in HEAs. The LAGB consists of an array of edge dislocations

aligned along the dislocation line. Collectively, these dislocations gives rise to a crystal rotation and lattice displacements $\mathbf{R_q}(x,y)$ proportional to the rotation angle, plus the strain field $\mathbf{R_d}(x,y)$ of each dislocations. Since the contrast of TEM imaging depends on $\mathbf{g} \cdot \mathbf{R}$ where $\mathbf{g}$ is the reflection used for dark field imaging and $\mathbf{R} = \mathbf{R_q} + \mathbf{R_d}$ when $\mathbf{g} \cdot \mathbf{R} = \mathbf{0}$, there will be no contrast. The observed change in the tweed-like contrast direction as we choose a different reflection $\mathbf{g}$ for imaging suggest that a range of $\mathbf{R}$ in many nanodomains. In the bright field imaging mode, the tweed-like contrast is absent due to the fact that only the direct beam is chosen to form the image and thus no $\mathbf{g} \cdot \mathbf{R}$ effect exists.

To investigate the underlying deformation mechanism of the HEA nanopillars, we followed the dislocation motion by simultaneous measurements of stress and displacement under compression and video recording of dislocations and crystal-slip events. Figure 5.6 shows an example of the simultaneous measurements. The [647] orientation has a single slip plane, which we observed using the bright-field (BF) TEM with the incident beam near the zone axis of [-312]. As the stress increased, the pillar began to deform plastically. The deformation process can be divided into the following three stages based on the engineering stress and time curve: a region with I) little or no stress drops, II) small stress drops, and III) large stress drops.

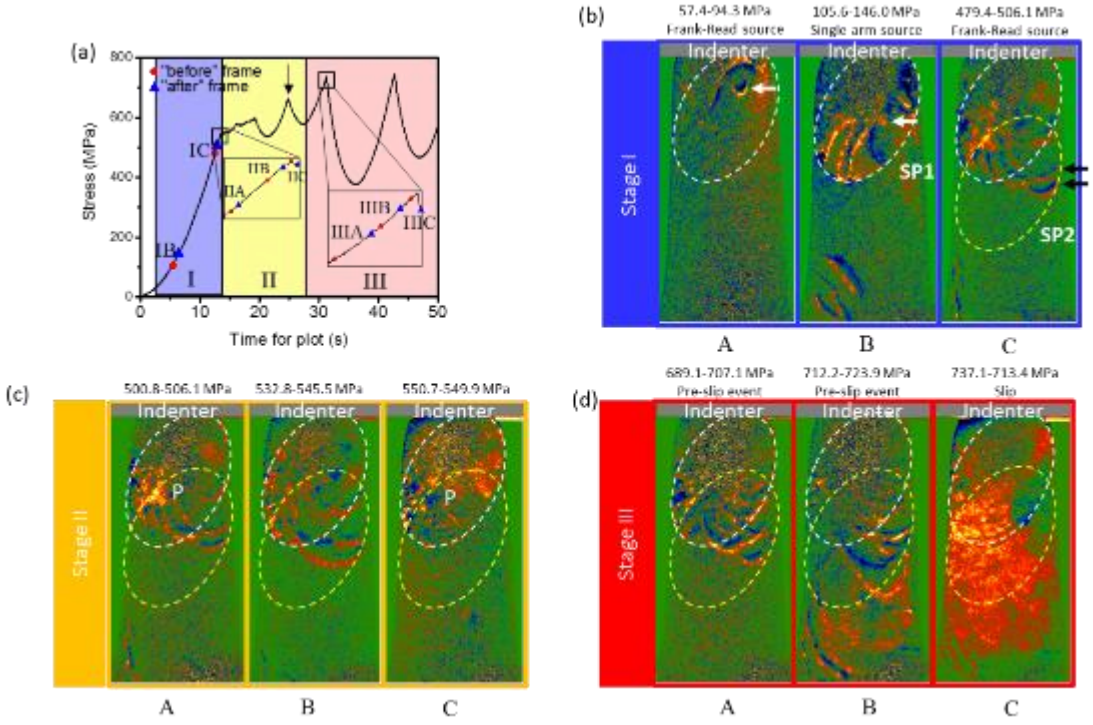

Figure 5.6. *Simultaneous nanocompression testing and TEM observations of a [647]-oriented HEA pillar and 665 nm in diameter. (a) the measured stress-time curve with color-coded deformation stages. The inset figures mark the representative event in stage I, II, and III. The color-scale images in b)-d) are captured from the video. The difference images are shown in color with yellow and blue for positive and negative difference image intensities of dislocations. Representative events in each deformation stage are chosen. b) shows the operation of Frank-Read dislocation sources and the single-arm dislocation source at different stress levels. The white dashed lines in (b) indicate the boundary of a slip plane. The Frank-Read dislocation sources in (b-A) and single arm sources in (b-B) operate on a single slip plane (marked as SP1). As the stress went up, a new Frank-Read source came in and operated at a slip plane, SP2. c) shows the pre-dislocation jump events (c-A and c-B) and the dislocation jump event. The dislocation jump occurs*

(Fig. 5.6 cont.) in the same crystal plane (SP1) as the operation plane of dislocation sources in (b-A,B). In (c-A), dislocations were pinned at point marked as "P" and stayed pinned at (c-B). At (c-C), the jammed dislocation depinned from position "P", resulting in a dislocation jump. d) shows the pre-slip event (d-A) and two slip events. The slip event in (d-B) occurred at a slip plane of SP1, and the slip event in (d-C) occurred in slip plane SP2.

In region or stage I, dislocations are nucleated and multiplied through two mechanisms, namely Frank-Read dislocation sources and single arm dislocation sources. Representative difference images were used to highlight dislocation behaviors. In difference images, the red color denotes the positive image intensity, and the blue color denotes the negative intensity. Since dislocations manifest themselves as dark contrast in the BF-TEM images, when taking the difference image by subtracting the "after" frame from the "before" frame, the positive intensity (red color) represents the new dislocation position while the negative intensity (blue color) represents the old dislocation position. Figure 5.6 (b) shows the dislocation-source activities in stage I; firstly, Frank-Read sources were activated near the pillar top due to the stress concentration of the tapered pillar geometry. As the stress went up, a single arm dislocation source began to operate. Single arm dislocation source is formed by one immobilized segment and one moveable segment of dislocation line. The moveable segment will swipe on the slip plane under the applied force. Once it swipes the entire slip plane, the nanopillar will slip by one Burger's vector. The spiral motion of single arm dislocation source is clearly shown in the difference image in Fig. 5.6

(b-B). Then the single arm source ceased to operate, and more Frank-Read sources started to operate and multiply more dislocations in the middle part of pillar [see Fig. 5.6 (b-C)]. Figure 5.7 shows an example of dislocation multiplication by Frank-Read dislocation source. FR source is formed due to two immobilized dislocation lines pinning the middle part of dislocation. When a shear stress is applied, the mobilized part of dislocations will bow out (see Fig. 5.7(a-c)). However, dislocations also have line tension force which tends to reduce the length of dislocation line. The required stress for dislocation to overcome the line tension of dislocations is $\tau = Gb/2r$ where G is the shear modulus, b is the Burger's vector. The smallest radius of curvature, obtained when the loop is in the form of a semi-circle, corresponds to the maximum stress required to continuously operate the FR source. When this threshold stress is reached, the FR source will continuously operate and generate dislocation loops. Under the action of the applied stress, this loop continues to expand, producing slip across the slip plane. Once the loop encounters either obstacles or grain boundary that is impenetrable to dislocations, the loop will stop moving. The resulting restricted motion of the dislocation lines produces a back stress to the following dislocations and oppose the FR operation. An array of dislocations can be seen after this process, which is shown in Fig. 5.7(d-f). In HEA, by taking G to be 80 GPa, b to be 0.2539 nm, and r to be 300 nm, the resultant threshold stress to overcome the line tension is 33 MPa. However, the measured shear stress required to continuously operate the Frank-Read source measured from the experiment is 100 MPa. The extra stress required is due to lattice distortion and low angle grain boundary (LAGB) in the HEA pillars.

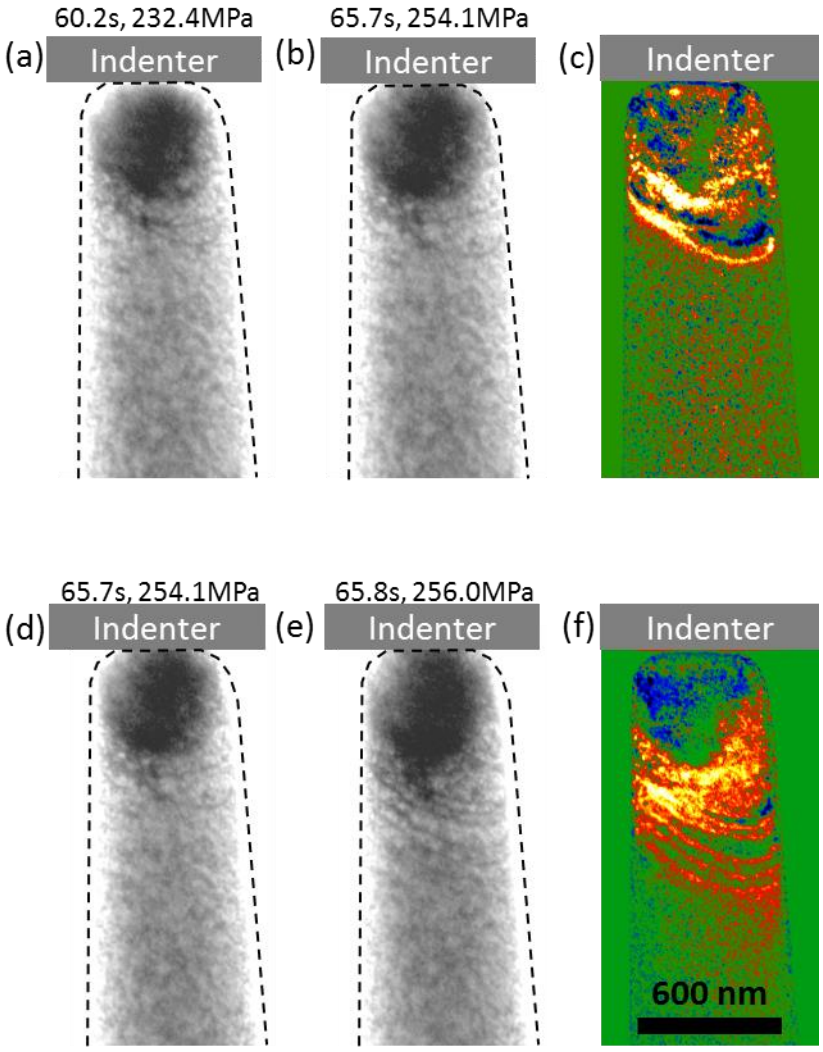

Figure 5.7. *The operation of Frank-Read dislocation source. (a-c) shows the bowing out of mobile part of dislocations under applied stress. (a) and (b) is shows the before and after frames of the bowing out event. (c) is the difference image by subtracting (b) from (a). When the threshold stress is reached, the Frank-Read dislocation source will continuously operate and generate dislocation arrays which is shown in (d-f).*

After the dislocation array has formed, it will propagate inside the HEA nanopillars. To gain

insight into the motion of dislocations in HEA, we tracked one dislocation named as d3 (see Fig. 5.8) by examining the dislocation position as a function of time. Figure 5.8(b) shows representative difference images between successive frames, showing the dislocation motion at the corresponding time intervals. The dislocation positions were measured with respect to its position at 33.1s along three lines (A, B, and C) as shown in the inset of Fig. 5.8 (a). The position versus time plot in Fig. 5.8 (a) shows the stepped dislocation motions, i.e., the dislocation moved intermittently in segments. Different segments moved at different paces; dislocation d3 moved faster along the C direction from 33.1s to 35.1s, which was then exceeded by segments along the directions of A and B. (The dislocation velocities in pure Cu, Al, and Fe are in the range of ~1-10^2 m/s. The dislocation group moved with significantly lower velocity of ~10^{-6} m/ in Au. In HEA, our data shows that single dislocations are shown to move at speeds of ~10^{-8} m/s even under shear stress ~200 MPa, which are eight to ten orders of magnitude slower in pure metals. This could be attributed to the highly distorted lattice and low-angle grain boundaries in HEAs. As compared to conventional metals and alloys, the HEA lattice is heavily distorted, due to the atomic size variations of the constituent elements and the variations in binding energy between atom pairs. Especially the presence of Al, whose atomic radius is larger than all the remaining four constituent elements, will greatly distort the lattice. The lattice distortion will make the lattice friction stress, also known as Peierls-Nabarro (P-N) stress which is a function of dislocation width and the length of Burgers vector [20], highly inhomogeneous. If a segment of a dislocation line is in the region where P-N stress is high, the activation stress required to move that segment will be quite large. Unless the

applied stress is provided to overcome the P-N stress, that part of dislocation segment becomes immobile, hence acting as a pinning point [17]. Besides, the low-angle grain boundaries are also well-known as strong dislocation barriers, which hinder the dislocation motion. Thus, dislocations in HEA move in a slow and jerky way and some parts of a dislocation line are moving faster than others.

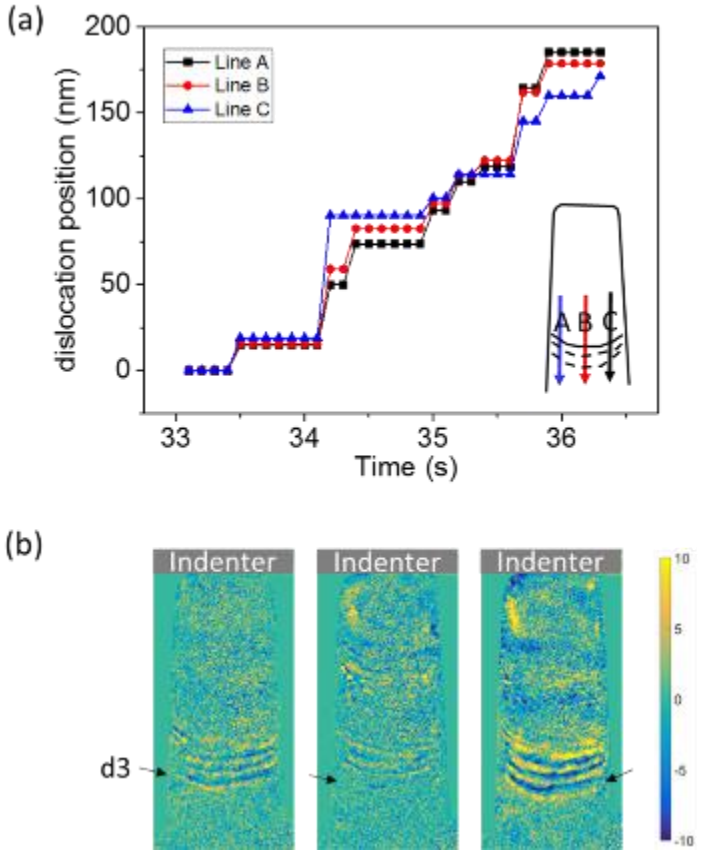

Figure 5.8. *Slow and intermittent motion of dislocation arrays in HEA nanopillar. (a) shows dislocation position of d3 versus time curve. (b) Successive frames and their different images showing the motion of dislocation d3.*

In stage II, we observed the collective motion of groups of dislocations. Figure 5.6 (c) shows a representative event, where groups of dislocations collectively jumped to new position (see c-C), resulting in the stress drop from 550.7 MPa to 549.9 MPa. To understand the trigger of the collective dislocation jump, two pre-dislocation jump events [see (c-A) and (c-B)] are shown to highlight the pinning-depinning transition of dislocations. In (c-A), there is a high image intensity area of dislocations in the difference images marked as "P". The high-intensity area is the new dislocation position, showing that dislocations were jammed and entangled at position "P". The pinning remained until the stress increased to 550.7 MPa and a collective dislocation jump occurred. The collective dislocation jump is resulted from depinning of the jammed and entangled dislocations, as evidenced by the negative intensity at position "P" in (c-C). The dislocation jump occurred at the same plane as the operation plane, (SP1), of the single arm-dislocation source and Frank-Read source.

In stage III, slip avalanches occurred, resulting in large stress drops. In Fig. 5.6(d), two pre-slip events and one slip event were selected to show the dislocation activities before and after the slip avalanche. Before the large slip avalanche, multiple dislocation movements can be clearly observed in the pre-slip events as the stress increased from 689.1 MPa to 723.9 MPa [see (d-A) and (d-B)]. Then a large slip avalanche happened, as shown in (d-C). In (d-C), there is a large area of high image intensity in the nanopillar. Through the careful inspection of the original frames

from the video-recording, this intensity change is not caused by dislocations but by an overall strain contrast change in the nanopillars. Large slip avalanche alleviates the strain built in the sample during the compression and thus changes the TEM BF-imaging contrast. The slip avalanche may be caused by the formation of ellipsoidal slip bands proposed by Brown[21]. However, the crystal-slip event happens so fast that it supersedes the temporal resolution of our instrument (0.1s), so a better camera with higher temporal resolution is needed to further understand this behavior.

To identify with certainty the observation of dislocation arrays and the nature of the observed dislocations, a TEM lamella was prepared from a deformed 706 nm diameter HEA pillar (see Fig. 5.9(b)) using Pt coating as protective layer and subsequent FIB milling under 2kV and 7pA to minimize Ga^+ damage. A montage of bright-field images of the lamella is shown in Fig. 5.9(a). Dislocation arrays were observed (marked by the white arrow) which indicates that dislocations, instead of moving on multiple slip planes, have a tendency to follow each other and move on the same slip plane. To characterize the nature of dislocations, **g·b** analysis of a lamella sample was performed by orientating the sample under different two beam conditions using a double-tile holder. By using $(0\bar{2}2)$ and $(\overline{31}1)$ reflections to form dark-field image (see Fig. 6(c-d)), the contrast of dislocation arrays disappears, indicating that observed dislocations are perfect dislocations with Burgers vector $\pm\frac{1}{2}(011)$. Two discrete slip steps are marked by the blue circles both in Fig. 5.9(a) and (b).

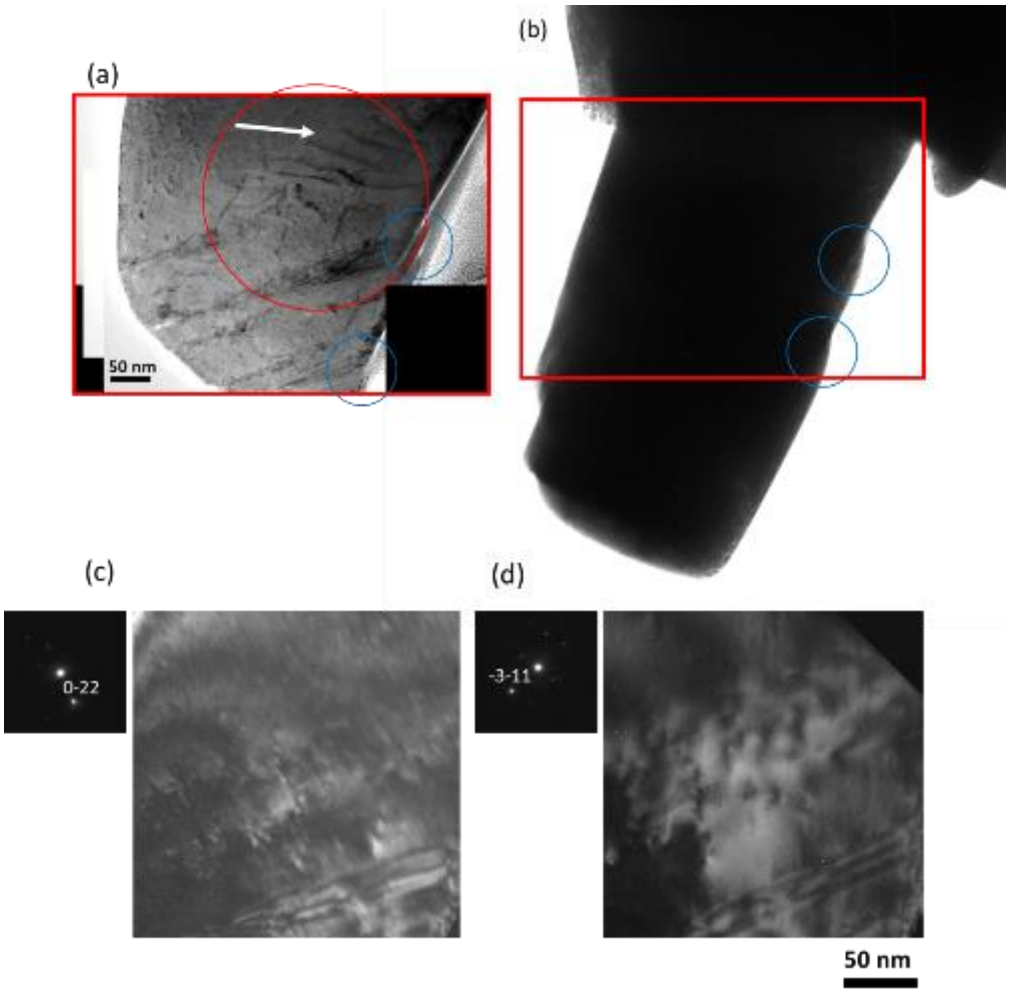

Figure 5.9. *A bright-field TEM image of a deformed 706 nm diameter HEA pillar shown in (b) after FIB milling into a lamella shape shown in (a). (c-d) post-mortem* ***g·b*** *analysis of the lamella sample.*

5.4. Conclusion

In this study, we reported a universal method that can be applied to other in situ TEM mechanical testing to achieve a quantitative understanding of dislocation activities. The deformation mechanism of HEA nanopillar is revealed by simultaneous measurement of mechanical response and dislocation dynamics. The plasticity of HEA is first carried by the operation of new dislocation

sources. As the dislocation density continues to rise, dislocations entangle with each other during propagation and cease to move. The entangled dislocation structure impedes the motion of dislocations and hardens the pillar significantly. The dislocation entanglement also de-activates the operation of certain dislocation sources. The entangled dislocation structure collectively jumps when the stress is high enough. At last, the large crystal slip happens. A large amount of dislocations escapes from the pillar accompanied by a large stress drop. The dislocation activities pick up and new dislocation sources are activated under further compression, and the dislocation density increases to a sufficiently high level so that another large slip occurs. This pattern repeats itself under the applied stress. Thus, the experiments in this paper visualize physical details of slowly-deformed HEAs and provide a more intuitive understanding of the creation and multiplication of dislocations and slip avalanches in HEAs during deformation. Nanoscale in situ testing can be used to determine bulk-like mechanical response and simultaneously identify deformation mechanisms in HEAs. This result is more similar to the study of irradiated metals (Clouet *et al.*[22] and by Kiener *et al.*[23]) than the nanopillars of pure metals, whereas in the latter mechanical property becomes dislocation source limited[24]. Overall, the HEAs feature unique atomic-scale stresses and internal dislocation sources, which made our observations possible. HEA nanopillars can serve as a model system to study the underlying mechanisms of large scale events, due to its simplicity in the interpretation of dislocation slip behaviors, large scale spanning of slip avalanche size, and experimental repeatability.

5.5. References

[1] Taylor GI. The Mechanism of Plastic Deformation of Crystals. Part I. Theoretical. Proceedings of the Royal Society of London Series A 1934;145:362-87.

[2] Orowan E. Zur Kristallplastizität. III. Zeitschrift für Physik 1934;89:634-59.

[3] Polanyi M. Über eine Art Gitterstörung, die einen Kristall plastisch machen könnte. Zeitschrift für Physik 1934;89:660-4.

[4] Orowan E. Zur Kristallplastizität. I. Zeitschrift für Physik 1934;89:605-13.

[5] Orowan E. Zur Kristallplastizität. II. Zeitschrift für Physik 1934;89:614-33.

[6] Hirsch PB, Horne RW, Whelan MJ. Direct observations of the arrangement and motion of dislocations in aluminium. Philos Mag 2006;86:4553-72.

[7] Bollmann W. Interference Effects in the Electron Microscopy of Thin Crystal Foils. Phys Rev 1956;103:1588-9.

[8] Hirsch PB, Howie A, Whelan MJ. A Kinematical Theory of Diffraction Contrast of Electron Transmission Microscope Images of Dislocations and Other Defects. Philos Tr R Soc S-A 1960;252:499-&.

[9] Messerschmidt U, Appel F. Quantitative Tensile-Tilting Stages for High-Voltage Electron-Microscope. Ultramicroscopy 1976;1:223-30.

[10] Martin JL, Kubin LP. Optimum Conditions for Straining Experiments in the Hvem. Ultramicroscopy 1979;4:257-.

[11] Fujita H. Ultra‐high voltage electron microscopy: Past, present, and future. Journal of

electron microscopy technique 1986;3:243-304.

[12] Imura T, Saka H. In-situ dynamic observations of dislocation behaviour in metals and alloys by high voltage electron microscopy. Nagoya University, Faculty of Engineering, Memoirs 1976;28:54-112.

[13] Oliver WC, Pharr GM. An Improved Technique for Determining Hardness and Elastic-Modulus Using Load and Displacement Sensing Indentation Experiments. J Mater Res 1992;7:1564-83.

[14] Oliver WC, Pharr GM. Measurement of hardness and elastic modulus by instrumented indentation: Advances in understanding and refinements to methodology. J Mater Res 2004;19:3-20.

[15] Antonaglia J, Xie X, Tang Z, Tsai CW, Qiao JW, Zhang Y, et al. Temperature Effects on Deformation and Serration Behavior of High-Entropy Alloys (HEAs). Jom 2014;66:2002-8.

[16] Carroll R, Lee C, Tsai C-W, Yeh J-W, Antonaglia J, Brinkman BAW, et al. Experiments and Model for Serration Statistics in Low-Entropy, Medium-Entropy, and High-Entropy Alloys. Scientific Reports 2015;5:16997.

[17] Komarasamy M, Kumar N, Mishra RS, Liaw PK. Anomalies in the deformation mechanism and kinetics of coarse-grained high entropy alloy. Mat Sci Eng a-Struct 2016;654:256-63.

[18] Kiener D, Minor AM. Source-controlled yield and hardening of Cu(100) studied by in situ transmission electron microscopy. Acta Mater 2011;59:1328-37.

[19] Kim KH, Xing H, Zuo JM, Zhang P, Wang HF. TEM based high resolution and low-dose

scanning electron nanodiffraction technique for nanostructure imaging and analysis. Micron 2015;71:39-45.

[20] Courtney TH. Mechanical behavior of materials. 2nd ed. Boston: McGraw Hill; 2000.

[21] Brown LM. Constant intermittent flow of dislocations: central problems in plasticity. Mater Sci Tech-Lond 2012;28:1209-32.

[22] Clouet E, Caillard D, Chaari N, Onimus F, Rodney D. Dislocation locking versus easy glide in titanium and zirconium. Nat Mater 2015;14:931-+.

[23] Kiener D, Hosemann P, Maloy SA, Minor AM. In situ nanocompression testing of irradiated copper. Nat Mater 2011;10:608-13.

[24] Shan ZW, Mishra RK, Asif SAS, Warren OL, Minor AM. Mechanical annealing and source-limited deformation in submicrometre-diameter Ni crystals. Nat Mater 2008;7:115-9.

CHAPTER 6

TUNED CRITICALITY OF SLIP AVALANCHES IN HIGH-ENTROPY ALLOY NANOPILLARS

6.1. Introduction

HEAs, composed of five or more elements of a near-equal molar percentage in random solutions[1, 2], have excellent thermomechanical properties[3-5]. However, HEAs exhibit complex, and unexplained mechanical behaviors[6, 7]. In a certain temperature and strain-rate regime, HEAs deform via sudden slips that are visible as stress drops or "serrations" in the stress-strain curve[7, 8]. Caroll et al.[7] presented a series of tensile-deformation experiments performed at slow strain rates on metals, including both conventional alloys and HEAs. The serration phenomena are found in medium-entropy alloys (CoFeNi and CoCrFeNi) and HEA (CoCrFeMnNi), not in low-entropy alloys (Ni and CoNi). The cause of serrations was previously unknown; ex-situ experiments suggest large crystal slips[7]. Crystal slip in general is poorly understood, despite of many past attempts[9].

Using in situ TEM, we carried out nanopillar compression experiments on the $Al_{0.1}CoCrFeNi$ HEA. Large and discrete slips are observed with the pillar sheared on the slip plane (Fig. 6.1), which resembles the shear bands of bulk metallic glass (BMG)[10]. We consistently observed that the slips are localized to a limited set of slip planes among nanopillars of 160 nm to 700 nm in

diameters and different crystal orientations, including single slip, double slip, and multiple slip orientations [Fig. 6.1(a, b)]. This phenomenon is very different from the deformation of single crystal Cu or Au nanopillars[11], where many slips are observed over a broad sheared region, as shown in Fig. 6.1(c). The few slips in HEAs indicate that the dislocation glide on few planes dominated the deformation, while dislocations easily cross-slip and glide on multiple slip planes in Cu or Au to form broad sheared regions. Diffraction analysis shows that the slip planes in HEAs are perfectly along the crystallographic plane of the FCC crystal. Because we change a 3 dimensional problem where dislocations can move along multiple slip planes to a 2 dimensional problem where dislocations are confined to limited set of slip planes, the interpretation of the results is significantly simplified. This feature of HEA makes it an ideal system to study dislocation dynamics and thus makes the results easy to transfer to large scale systems, like earthquakes.

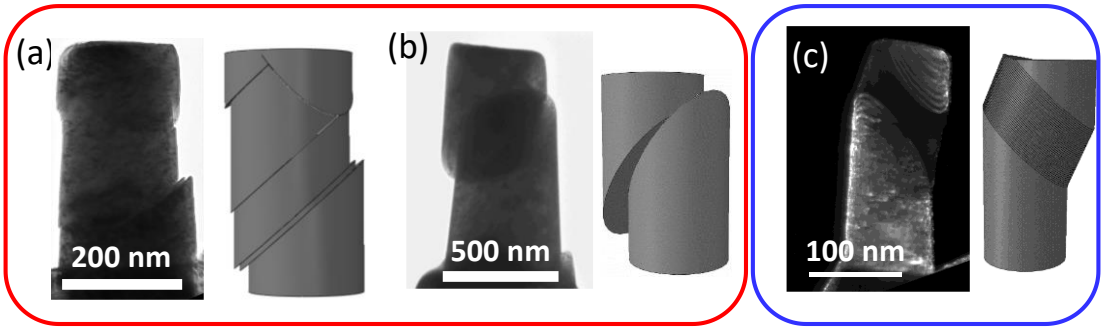

Figure 6.1. *Comparison of slip behaviors between HEA and pure Cu pillars. HEA pillars (a-b) show planar-slip behaviors and formation of sharp slip steps, while pure copper pillars (c) exhibit slip bands and multiple slip planes.*

Previous studies[12, 13] have reported that solid materials, whose size scale ranges from nanopillars to the earth, all show the same scaling behavior for their slip-size distributions and other statistical properties. The scaling is predicted by the simple coarse-grained mean field theory (MFT) model[14], that weak spots, which slip along slip planes (when a sufficiently-large shear stress is applied) trigger other weak spots to slip, resulting in slip avalanches typically detected as sudden stress drops and displacement jumps. The stress drops and displacement jumps can be measured mechanically. Figure 6.2(a) shows examples of the measured engineering stress-time curve and displacement-time curves from a [647]-oriented nanopillar of the $Al_{0.1}$CoCrFeNi HEA.

6.2. Analysis Method

For the statistical analysis, a slip event is characterized by a starting time t_{start}, an ending time t_{end} and a slip velocity. The compression starts when the indenter is set to move at a constant displacement rate set manually as threshold velocity V_{thr}. When a slip event happens, the displacement signal measured from the indenter experiences a sudden increase on the magnitude from $V_{thr}\times t_{start}$ and later recovers back to $V_{thr}\times t_{end}$ after an avalanche is completely over. From time from t_{start} to t_{end}, $V(t)$ exceeds V_{thr} and such jump in displacement signal indicates a slip on the sample and is defined as one slip avalanche. A time derivative signal is calculated by numerically differentiating the displacement signal with respective to time signal. A threshold value on the slip velocity is set to capture a slip event's beginning and ending when the

velocity exceeds and falls below such threshold. The difference between the beginning and ending points in the displacement signal stands for one displacement jump, or as one slip event. Another threshold value on the extracted slip size is also set in order to filter out the events calculated due to the machine noise. The stress level for each slip event is also found by extracting the index of the beginning of each slip avalanche and traversing the stress signal until the corresponding index. The critical ("failure") stress, is then found by looking for the maximum value in stress signal.

Due to the sensitivity of the indenter to its background noise, the displacement versus time curve experiences fluctuations due to noise during the time when no slip events happened. Consequently, the raw displacement signal's time derivative is under the influence of noise during each slip event. Therefore, a smooth window on both displacement signal and again on its time derivative are employed to average out the effect of noise. By using the window size of 30 on displacement signal and 5 on its time derivative, we can roughly extract multiple time periods when slip events occurred by locating the sudden jump on smoothed displacement time derivative plot shown as peaks compared to fluctuations around zero while the signal is dominated by noise without any slip event.

Since each slip event happens suddenly, we see the displacement signal's monotonic increase on its magnitude between t_{start} and t_{end} , which also results in a series of discrete positive time derivative values. After extracting the rough time period from the smoothing method mentioned above, we again extracted all time index of the monotonic increase on displacement signal by transversing the time derivative during each rough periods we found above. While we are still

under the influence of noise which also might have monotonic increase on displacement, each slip event's magnitude is much higher compared to that of noise. Therefore, a slip size is found by looking for the difference in displacement signal of the last time index and the first time index during each monotonic increase period and the largest size is what we found for the slip size during that period. We then plot the time signal and its corresponding displacement signal on the raw data using marker (triangle or circle) shown in Fig. 6.2, which again shows the accuracy of this method used above.

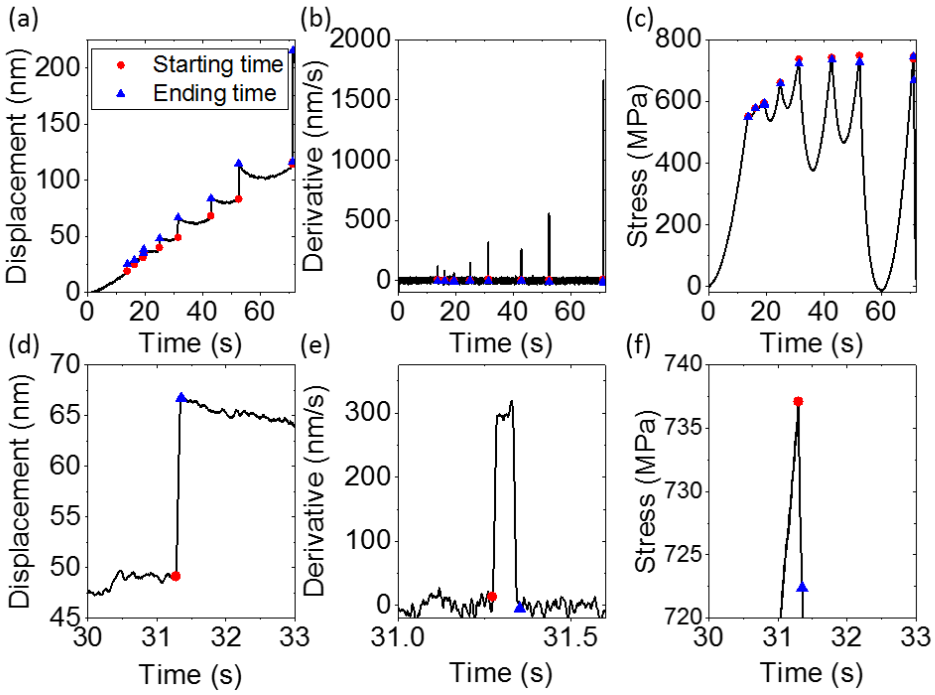

Figure 6.2. *(a-c) show the displacement-time, derivative of displacement-time, and stress-time curves. The red circle and blue square show the position of slip start time and slip end time. (d-f) are the magnified view of displacement-time, derivative of displacement-time, and stress-time curves for one slip event.*

In the MFT model, in the absence of hardening and weakening, at a certain level of applied stress, τ, the stress-binned slip-density distribution follows a power law with an exponentially decaying function introducing stress as a tuning parameter but limited by the cut-off size, $S_{max} \sim (\tau_c - \tau)^{-\frac{1}{\sigma}}$.

$$D(S,\tau) \sim S^{-\kappa} f_s[S(\tau_c - \tau)^{\frac{1}{\sigma}}] \tag{6.1}$$

Here S is the magnitude of the displacement jump as one slip avalanche. The MFT model predicts that κ = 1.5 and σ = 0.5. τ_c is the failure stress, also called a critical stress. A Complementary Cumulative Distribution Function (CCDF), $C(S,\tau)$, is plotted in Fig. 6.2(b) for analysis, which shows the probability of finding the size of a slip event is larger than a specific value.

$$C(S,\tau) \sim \int_S^\infty D(S',\tau)\mathrm{d}S' \sim S^{-(\kappa-1)} g(S(\tau_c - \tau)^{\frac{1}{\sigma}}) \tag{6.2}$$

where $g(x) \equiv \int_x^\infty e^{-At} t^{-\kappa} \mathrm{d}t$ is the universal scaling function[14]. The stress-integrated slip-size distribution is calculated by integrating over all stress as

$$D_{int}(S) \equiv \int D(S,\tau)\mathrm{d}\tau \sim S^{-(\kappa+\sigma)} \tag{6.3}$$

The stress-integrated CCDF takes the form as

$$C(S) \sim \int_S^\infty D_{int}(S')\mathrm{d}S' \sim S^{-(\kappa+\sigma-1)} \tag{6.4}$$

Since the MFT model predicts that κ = 1.5 and σ = 0.5, the stress-integrated CCDF then scales as $C(S) \sim S^{-1}$.

6.3. Results

The log-log scaled CCDF for 145 slip events from seven HEA nanopillars of [647] pillar orientation and approximate diameter 530 nm is plotted in Fig. 6.3(b) as well as the -1 predicted slope line, which shows the consistency between our model and the experimental result. For the analysis, displacement jumps were extracted directly from the displacement-time signal [see Fig. 6.3(a) for an example] obtained during nanopillar compression to plot the CCDF. In Fig. 6.3(b), two orders of magnitude of slip avalanche sizes from 1 nm to 100 nm can be observed from our experiment. Moreover, in situ TEM imaging provides us with single dislocation resolution. When a single dislocation slips out of the pillar, the pillar will slip by 0.28 nm. Thus, the combination of in situ TEM imaging with the mechanical testing offers an unprecedented 3 orders magnitude observation capabilities of slip avalanches behaviors, which in turn provides us the possibility to predict the behavior of earthquake spanning 3 Richter magnitude scale.

Similarly, the distribution of displacement jumps during slip is predicted to follow a modified power law as a function of applied stress. The distribution form is

$$D(S,f) \sim S^{-\kappa} f_s(Sf^{\frac{1}{\sigma}}) \tag{6.5}$$

where f_s is a universal scaling function with an exponential decay, and $f \equiv 1 - \tau/\tau_m$, where τ_m is taken to be the maximum observed stress[7, 14]. A CCDF is evaluated as

$$C(S,f) \sim \int_S^{\infty} D(S',f)\mathrm{d}S' \sim f^{-\frac{\kappa-1}{\sigma}} g(Sf^{\frac{1}{\sigma}}) \tag{6.6}$$

where g is a universal scaling function. With this explicit function for the slip-size distribution, a scaling collapse of the experimental slip avalanche can verify exponent values calculated using

the MFT model. In the inset of Fig. 6.3(c), we plot $C(S,f)f^{-\frac{\kappa-1}{\sigma}}$ versus $Sf^{\frac{1}{\sigma}}$ and we should expect CCDF binned over all stress levels to collapse together and yield exponent values in consistency with model predictions. The critical exponents (τ_m, σ, and κ) shown in the figure are tuned until all curves lie on top of each other, which yields the correct values, κ = 1.5 and σ = 0.5[15]. The collapse itself follows a universal scaling *function* as $g(x) \equiv \int_s^\infty e^{-At}t^{-\kappa}\mathrm{d}t$ (here A is a non-universal constant, A = 1.2), whose shape is also predicted by MFT.

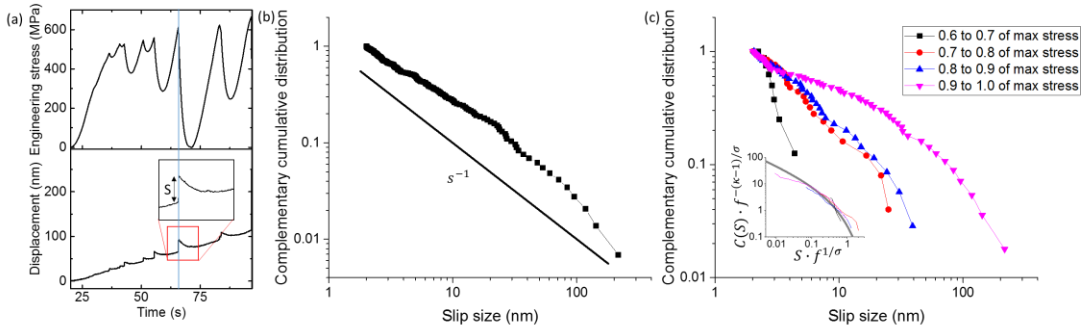

Figure 6.3. *Measurement and statistical analysis of slip jumps. a) The characteristic stress- and displacement-time curve for the in-situ compression experiment and for a [647]-oriented nanopillar. b) Stress-integrated complementary cumulative distribution, C(S), of slip sizes, S, over all stress levels for HEA pillars using events from seven [647]-oriented samples of an approximate diameter, 530 nm, compressed at strain rate* 1×10^{-3} */s with a -1 slope line as predicted by MFT. 145 slip events were detected in total. (c) Main figure: Stress-binned complementary cumulative distribution,C(S, τ), of slip sizes as a function of the stress level over the maximum stress using the same events as in (b). Inset: Scaling collapse of the same data as well as the predicted scaling*

(Fig. 6.3 cont.) function, $g(x) \equiv \int_s^\infty e^{-At} t^{-\kappa} dt$ *(A is a non-universal constant, A = 1.2),* $f \equiv 1 - \frac{\tau}{\tau_m}$*, (see Ref. 16);* $\kappa = 1.5 \pm 0.10$ *and* $\sigma = 0.5 \pm 0.055$ *(as predicted by MFT).*

The above statistical analysis shows the slip avalanche's dependence on the stress level, which indicates that the applied stress is a critical tuning parameter. The deformation of HEAs thus exhibits the tuned critical behavior rather than self-organized criticality. This trend agrees with recent analyses on BMGs[10, 16, 17] and nanocrystals[15], and prior MFT-model predictions[7, 14].

Both the dislocation jumps and large slip avalanches are accompanied by stress drops. As shown in Fig. 6.5(a), the stress drop has a linear relationship with the observed displacement jump. The same is true in the MFT model mentioned above. Since we include both small stress drops (corresponding to collective dislocation jumps) and large stress drops (corresponding to slip avalanches), the universal linear relationship between the stress drop and displacement jump indicates that they all obey the same physical rule. To further examine this rule, the relationship between the dislocation swept area and stress drop is investigated in Fig. 6.5(b). Figure 6.4 shows two examples of the method used to measure dislocation swept area. The dislocation swept area was measured using difference map between successive frames. The difference map gives clear contrast of dislocation new position and old position. The area between them was measured as the dislocation swept area after taking consideration of geometric relationship between slip plane and projection plane in TEM. If multiple dislocations moved together, the swept area is taken as the

sum of individual dislocation swept area.

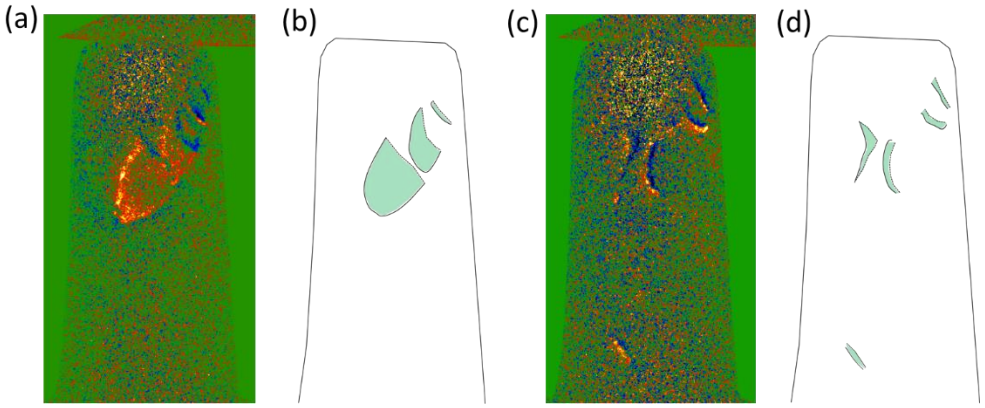

Figure 6.4. *Two examples of dislocation swept area measurement. (a) and (c) show the original difference images. (b) and (d) show the schematics of dislocation swept areas in shaded pattern.*

The swept area vs. displacement jump shows a linear relationship in the log-log scale plot with a slope of 1. This observation provides a direct support for the MFT, which predicts that for the slip avalanches in the scaling regime, the dislocation swept area should scale linearly with the stress drop during the avalanche[14, 18]. The same relationship is also expected in conventional FCC metals, which however cannot be experimentally verified because of the fast dislocation motion in these materials.

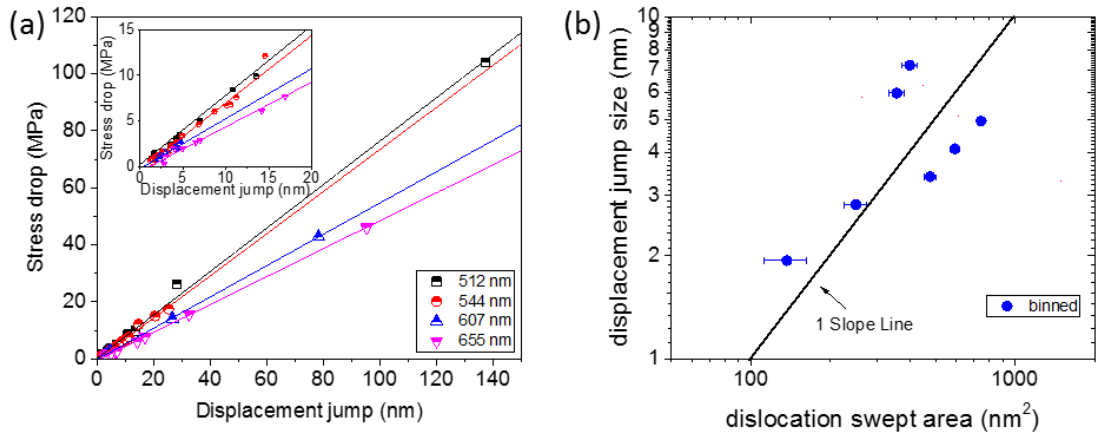

Figure 6.5. *Correlation between stress drops and displacement jumps and dislocation motion. (a) Stress drop versus displacement jump shows a linear relationship. Inset figure is magnified plot in the small stress-drop region. (b) shows a linear relationship between the dislocation swept area versus displacement-jump size.*

6.4. Discussion

The above experimental results show that there were a series of yielding events, which can be related to the basic assumptions in the MFT. In the MFT model, during slip avalanches, reminiscent of the Portevin LeChatellier Effect, the participating weak spots are weakened from their original strength to a lower strength, but they are re-strengthened during the time intervals between slip avalanches. The weak spots are dislocations in the $Al_{0.1}CoCrFeNi$ HEA at room temperature and the strain rate of 10^{-3}/s. The slip jumps from small dislocation slips is too small to be detected, only intermittent motion of dislocation arrays and slip avalanches result in significant slip jumps. The

MFT analysis results show that these two types of activities follow the same physical model. The intermittent dislocation motion demonstrates that the dislocations are pinned by obstacles in the sample, requiring the activation of further motion with sequentially higher stresses. The obstacles impeding dislocation movement include atomic stresses in HEAs[19, 20], inhomogeneous strain field, and immobile jogs produced by dislocation interactions. Low-angle grain boundaries are also detected in the sample, which provide strong resistance to dislocation motion as well as dislocation sources. Large atomic stresses have been suggested in HEAs from the atomic-size variations of the constituent elements[19, 21, 22] and the variations in chemical bonds between atom pairs[19, 20, 23]. Such resistance is expected to play a role in the early stage of deformation when dislocations in HEA move in a slow and jerky way and some parts of a dislocation line are moving faster than others. The atomic stresses and high density low-angle grain boundaries distinguish HEAs from elemental metals.

The variation in slip behaviors between HEAs and copper can be attributed to the stacking-fault-energy (SFE) difference. HEAs have been reported to have low SFE. Zaddach et al.[24] studied the SFE in the NiFeCrCoMn HEA system and found that its SFE is ~20 - 25 mJ/m^2, while Cu has ~70 - 78 mJ/m^2. The SFE controls the ease of cross slip in FCC metals. In FCC metals, screw dislocations can cross slip. However, if the FCC metal has a low SFE, a perfect screw dislocation tends to dissociate into two partial dislocations. The lower the SFE, the larger the distance between two partials. In order to cross slip, two partial dislocations need to recombine with each other since the partial dislocation contains an edge component that cannot cross slip.

The more widely-separated the partials, the more difficult the recombination process. The FCC metals with low SFE cannot easily cross slip and hence the slip is localized on a limited set of slip planes.

6.5. Conclusion

The experimentally-obtained stress-dependent slip-size distributions and the spatial properties of the slips in the HEA nanopillars agree with the MFT-model predictions. We obtained a scaling collapse of the slip-avalanche size distributions as function of applied stress and dislocation activities that confirm MFT-scaling predictions and indicate that the applied stress is a critical tuning parameter. It shows that the deformation of HEAs is a tuned critical phenomenon rather than a self-organized critical one. The approximately-linear growth of the dislocation swept area with the stress drop confirms previously untested MFT predictions for spatial correlations of slip avalanches, and constitutes the first test of the spatial scaling behavior in these systems. HEA nanopillars can serve as a model system to study the underlying mechanisms of large scale events, due to its simplicity in the interpretation of dislocation slip behaviors, large scale spanning of slip avalanche size, and experimental repeatability. It thus provides an unprecedented possibility for hazard prediction studies of earthquakes events, which can be rarely observed.

6.6. References

[1] J.W. Yeh, S.K. Chen, S.J. Lin, J.Y. Gan, T.S. Chin, T.T. Shun, C.H. Tsau, S.Y. Chang. Nanostructured high-entropy alloys with multiple principal elements: Novel alloy design concepts and outcomes, Adv Eng Mater 6 (2004) 299-303.

[2] B. Cantor, I.T.H. Chang, P. Knight, A.J.B. Vincent. Microstructural development in equiatomic multicomponent alloys, Mat Sci Eng a-Struct 375 (2004) 213-218.

[3] Z. Li, K.G. Pradeep, Y. Deng, D. Raabe, C.C. Tasan. Metastable high-entropy dual-phase alloys overcome the strength–ductility trade-off, Nature advance online publication (2016).

[4] B. Gludovatz, A. Hohenwarter, D. Catoor, E.H. Chang, E.P. George, R.O. Ritchie. A fracture-resistant high-entropy alloy for cryogenic applications, Science 345 (2014) 1153-1158.

[5] M.A. Hemphill, T. Yuan, G.Y. Wang, J.W. Yeh, C.W. Tsai, A. Chuang, P.K. Liaw. Fatigue behavior of Al0.5CoCrCuFeNi high entropy alloys, Acta Mater 60 (2012) 5723-5734.

[6] J. Antonaglia, X. Xie, Z. Tang, C.W. Tsai, J.W. Qiao, Y. Zhang, M.O. Laktionova, E.D. Tabachnikova, J.W. Yeh, O.N. Senkov, M.C. Gao, J.T. Uhl, P.K. Liaw, K.A. Dahmen. Temperature Effects on Deformation and Serration Behavior of High-Entropy Alloys (HEAs), Jom 66 (2014) 2002-2008.

[7] R. Carroll, C. Lee, C.-W. Tsai, J.-W. Yeh, J. Antonaglia, B.A.W. Brinkman, M. LeBlanc, X. Xie, S. Chen, P.K. Liaw, K.A. Dahmen. Experiments and Model for Serration Statistics in Low-Entropy, Medium-Entropy, and High-Entropy Alloys, Scientific Reports 5 (2015) 16997.

[8] Y. Zhang, T.T. Zuo, Z. Tang, M.C. Gao, K.A. Dahmen, P.K. Liaw, Z.P. Lu. Microstructures

and properties of high-entropy alloys, Prog Mater Sci 61 (2014) 1-93.

[9] L.M. Brown. Constant intermittent flow of dislocations: central problems in plasticity, Mater Sci Tech-Lond 28 (2012) 1209-1232.

[10] J. Antonaglia, X. Xie, G. Schwarz, M. Wraith, J.W. Qiao, Y. Zhang, P.K. Liaw, J.T. Uhl, K.A. Dahmen. Tuned Critical Avalanche Scaling in Bulk Metallic Glasses, Scientific Reports 4 (2014).

[11] J.R. Greer, W.C. Oliver, W.D. Nix. Size dependence in mechanical properties of gold at the micron scale in the absence of strain gradients (vol 53, pg 1821, 2005), Acta Mater 54 (2006) 1705-1705.

[12] M. Zaiser. Scale invariance in plastic flow of crystalline solids, Adv Phys 55 (2006) 185-245.

[13] J.T. Uhl, S. Pathak, D. Schorlemmer, X. Liu, R. Swindeman, B.A.W. Brinkman, M. LeBlanc, G. Tsekenis, N. Friedman, R. Behringer, D. Denisov, P. Schall, X.J. Gu, W.J. Wright, T. Hufnagel, A. Jennings, J.R. Greer, P.K. Liaw, T. Becker, G. Dresen, K.A. Dahmen. Universal Quake Statistics: From Compressed Nanocrystals to Earthquakes, Scientific Reports 5 (2015).

[14] K.A. Dahmen, Y. Ben-Zion, J.T. Uhl. Micromechanical Model for Deformation in Solids with Universal Predictions for Stress-Strain Curves and Slip Avalanches, Phys Rev Lett 102 (2009).

[15] N. Friedman, A.T. Jennings, G. Tsekenis, J.Y. Kim, M.L. Tao, J.T. Uhl, J.R. Greer, K.A. Dahmen. Statistics of Dislocation Slip Avalanches in Nanosized Single Crystals Show Tuned Critical Behavior Predicted by a Simple Mean Field Model, Phys Rev Lett 109 (2012).

[16] J. Antonaglia, W.J. Wright, X.J. Gu, R.R. Byer, T.C. Hufnagel, M. LeBlanc, J.T. Uhl, K.A. Dahmen. Bulk Metallic Glasses Deform via Slip Avalanches, Phys Rev Lett 112 (2014).

[17] B.A. Sun, H.B. Yu, W. Jiao, H.Y. Bai, D.Q. Zhao, W.H. Wang. Plasticity of Ductile Metallic Glasses: A Self-Organized Critical State (vol 105, 035501, 2010), Phys Rev Lett 109 (2012).

[18] D.S. Fisher, K. Dahmen, S. Ramanathan, Y. Ben-Zion. Statistics of earthquakes in simple models of heterogeneous faults, Phys Rev Lett 78 (1997) 4885-4888.

[19] W. Guo, W. Dmowski, J.Y. Noh, P. Rack, P.K. Liaw, T. Egami. Local Atomic Structure of a High-Entropy Alloy: An X-Ray and Neutron Scattering Study, Metall Mater Trans A 44A (2013) 1994-1997.

[20] T. Egami, M. Ojha, O. Khorgolkhuu, D.M. Nicholson, G.M. Stocks. Local Electronic Effects and Irradiation Resistance in High-Entropy Alloys, Jom 67 (2015) 2345-2349.

[21] R.S. Mishra, N. Kumar, M. Komarasamy. Lattice strain framework for plastic deformation in complex concentrated alloys including high entropy alloys, Mater Sci Tech-Lond 31 (2015) 1259-1263.

[22] M. Komarasamy, N. Kumar, R.S. Mishra, P.K. Liaw. Anomalies in the deformation mechanism and kinetics of coarse-grained high entropy alloy, Mat Sci Eng a-Struct 654 (2016) 256-263.

[23] C. Niu, A.J. Zaddach, A.A. Oni, X. Sang, J.W. Hurt, J.M. LeBeau, C.C. Koch, D.L. Irving. Spin-driven ordering of Cr in the equiatomic high entropy alloy NiFeCrCo, Appl Phys Lett 106 (2015).

[24] A.J. Zaddach, C. Niu, C.C. Koch, D.L. Irving. Mechanical Properties and Stacking Fault Energies of NiFeCrCoMn High-Entropy Alloy, Jom 65 (2013) 1780-1789.

CHAPTER 7

PROPAGATION OF SOLITON-LIKE DISLOCATION WAVES AND DISLOCATION HARDENING IN COMPRESSED ALLOY NANOPILLARS

7.1. Introduction

Dislocations are one-dimensional defects in materials, consisting of an extra crystal plane or shear which terminated inside the crystal along a line of atoms. Under applied stress, crystalline materials exhibit irreversible and plastic deformation resulted from the dislocation motion. At the mesoscopic scale, experiments on pillars of hundreds of nm to microns have indicated that plastic flow in crystalline materials is not smooth, but characterized by multiple strain burst or stress drops[1-3]. The measured stress-strain curves are serrated under displacement control or contain strain bursts under load control. These features are shared by other slow-stressed physical systems as well, including metallic glasses, granular materials, rocks and earth, spanning 12 decades in length scale[4]. The intermittent plastic flow makes it difficult to control the deformation, which could have disastrous effects on materials applications.

Extensive research efforts have been devoted to understand and predict the intermittency in plastic flow, both computationally and experimentally[3, 5-12]. Dislocation dynamics (DD) is an example. It simulates dislocation activities and interactions and provides detailed mesoscopic information from the simulations. The DD based simulation studies have suggested that the intermittency during deformation is caused by collective dislocation avalanches, involving

successive bursts of multiple dislocations. Miguel et al.[5] performed 2D DD simulation on an ice crystal under creep deformation. They found that dislocations move in a scale-free intermittent fashion. The 3D DD simulations on a FCC crystal by Csikor et al.[13] successfully reproduced the characteristic deformation curve of fcc crystals. They also observed intermittent plastic flow, which can be well correlated with collective dislocation bursts. However, the applied strain rate is orders of magnitude higher than experimental conditions. Experimental insights of dislocation avalanche behaviors came from the detection of acoustic emission[5] and compression tests[14] on bulk or micro-sized specimens. For example, strain bursts detected in compression mechanical test experiments and acoustic emission energies show power-law distribution. However, these are indirect measurements of dislocation activities and thus these measurements alone do not provide a complete dynamical picture of intermittent plastic flow.

Dislocations, in principle, can be observed using transmission electron microscopy (TEM). Electron atomic resolution imaging in principle provides details of dislocation structure, including the dislocation core, but the stringent imaging conditions (e.g. the use of thin samples) make it unsuitable for in-situ study of mesoscopic collective dislocation dynamics. Diffraction contrast imaging at nm-resolution has been employed, instead, for imaging dislocations[15-18]. However, direct observation of dislocation behaviors during deformation still requires small samples, such as thin-films[19, 20] or nanopillars[21, 22]. Previous experiments have shown that the nanopillars of simple metals behave mechanically very differently from bulk metals, which are dominated by

the size effect[1, 2]. On the other hand, Kiener et al.[23] demonstrated in situ TEM nanocompression tests display bulk-like deformation behavior in irradiated copper nanopillars.

Our study focuses on high-entropy alloys (HEAs), a new alloy composed of five or more elements of a near-equal molar percentage in random solutions[24, 25] with excellent thermomechanical properties[26-28]. The HEA of $Al_{0.1}CoCrFeNi$ we studied here has the simple FCC structure, but because of the difference in atomic radii, the material exhibit complex and unexplained mechanical behaviors[29, 30], including sudden slips that are visible as stress drops or "serrations" in the stress-strain curve[30, 31].

7.2. Experimental Methods

To identify the orientation of grains in the polycrystalline HEA sample, electron backscattered diffraction (EBSD) was performed in a SEM (JEOL 7000F Analytical SEM, JEOL). As shown in Fig. 7.1(a), three grains with the pillar axis along [116], [103], and [647] were identified by EBSD, and they give rise to multiple slip, double-slip, and single-slip planes, respectively. After EBSD characterization, the grain with single slip orientation [647] was selected to produce HEA nanopillars (for details of orientation selection, see Section 5.2). Focused ion beam (FIB) (Helios 600i, FEI) was used to fabricate nanopillars. Nanopillar samples were milled using annular milling method with 30 keV and 7.7 pA to reduce the surface damage. Further details on sample preparation and characterization can be found in Chapter 2 and Chapter 5.

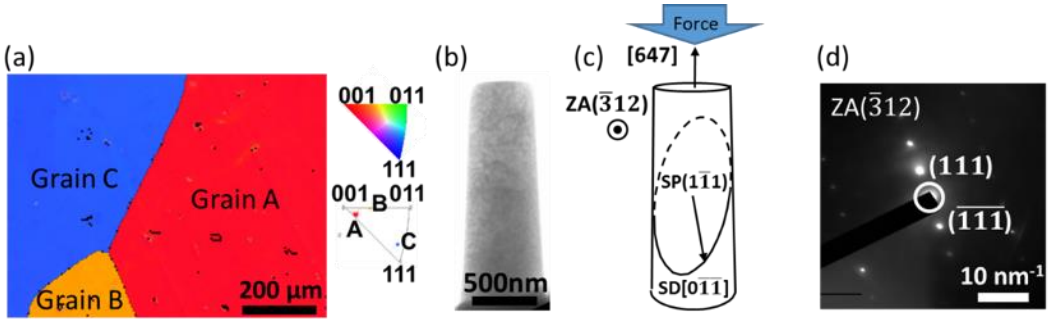

Figure 7.1. *Geometry of HEA nanopillar. (a) An EBSD orientation map obtained from the polycrystalline HEA sample with three grains, marked as A, B, and C corresponding to the [116], [103], and [647] grain orientations. The inverse pole figure and color map for orientation are shown in the inset of a). b) shows a bright field TEM image of a 512 nm nanopillar. A large amount of defects exist before compression. c) A schematic showing the geometry between compression axis [647], zone axis [-312], slip plane (1-11), and slip direction [0-1-1]. Slip plane and slip direction are abbreviated as SP and SD in the figure. The diffraction pattern is shown in (d). The (111) diffraction spot is excited. The center diffraction spot marked by white circle is selected to form the bright-field image.*

In situ compression tests of the HEA nanopillars were performed using a Hysitron picoindenter (Hysitron PI95 TEM holder, Hysitron) equipped with a 2 μm flat punch diamond indenter in a JEOL 2010 LaB6 TEM (JEOLUSA, Boston) operated at 200 keV. The compression tests were performed in the displacement-controlled mode with the displacement rates of 0.5 - 1.5 nm/s, resulting in a strain rate of ~ 1×10^{-3} /s. The load, displacement, and time data were read

out at 500 Hz. A video of each test was recorded using a charge-coupled device (CCD) camera (Gatan Orius, Gatan) with a resolution of 720×480 pixels and readout at 10 frames per second.

7.3. Results and Discussion

To investigate the underlying deformation mechanism of the HEA nanopillars, we followed the dislocation motion by simultaneous measurements of stress and displacement under compression and video recording of dislocations and crystal-slip events. Figure 7.2 shows an example of the simultaneous measurements The [647] orientation has a single slip plane, which we observed using the bright-field (BF) TEM with the incident beam near the zone axis of [-312]. As the stress increased, the pillar began to deform plastically. The deformation process can be divided into the following three stages based on the engineering stress and time curve: a region with I) little or no stress drops, II) small stress drops, and III) large stress drops.

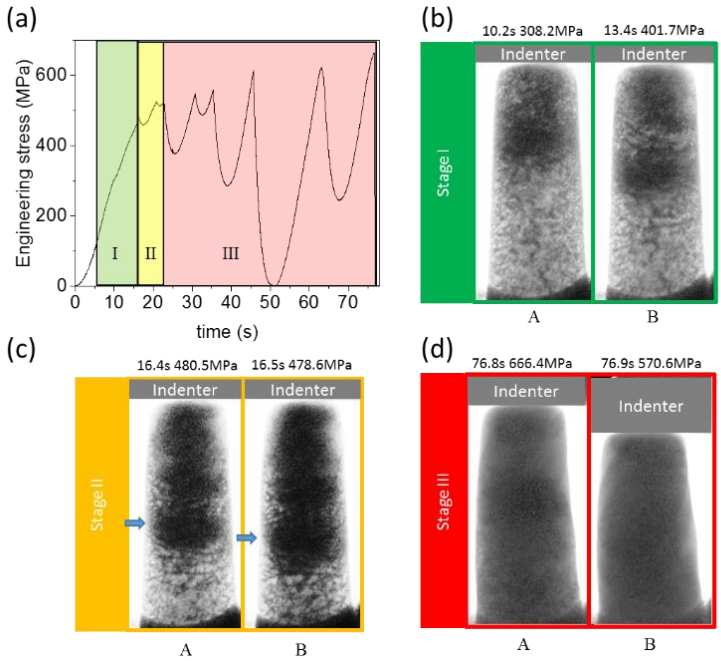

Figure 7.2. *Simultaneous nanocompression testing and TEM observations of a [647]-oriented HEA pillar and 512 nm in diameter. a) the measured stress-time curve with color-coded deformation stages. The images in b)-d) are captured from the video. Representative events in each deformation stage are chosen. b) shows the dislocation array flowing through nanopillar. c) shows the collective movement of group of dislocations resulting in a small stress drop. d) shows the crystal slip event.*

In stage I, dislocations nucleated from the pillar top and propagated toward the pillar bottom as shown by the two representative images at t=10.2 and 13.4 s in Fig. 7.2(b). The dislocation density continued to increase during stage I. Dislocations moved intermittently and followed each other and travelled in an array. The intermittent dislocation motion resembles a pinning-depinning motion of dislocations between obstacles[32-34]. In stage II, we observed the collective motion of

groups of dislocations. The density of dislocations is high enough that discrete dislocation dynamics (DDD) simulation can no longer be applied in this case. Figure 7.2(c) show a representative event, where groups of dislocations (marked by the arrows) jumped towards the pillar bottom, resulting in stress drop from 480.5 MPa to 478.6 MPa. In stage III, dislocation avalanches occurred resulting in large crystal slip. The contour of the slip plane is visible in Fig. 7.2(d-B).

To examine dislocation dynamics during the three stages of deformation leading to large slip avalanches, we measured the dislocation activities during the compression by quantifying the dislocation line contrast in the recorded images. A line detection algorithm was used to transform the recorded images into binary images, where the contrast of a dislocation yields a line pixel with value of 1 (see Fig. 7.3). By counting the number of line pixels, we can obtain the total number of the line pixels, as well as the density of line pixels within the nanopillar. Using this method, we can monitor the dislocation activities through the evolution of line pixel density and the total number of line pixels.

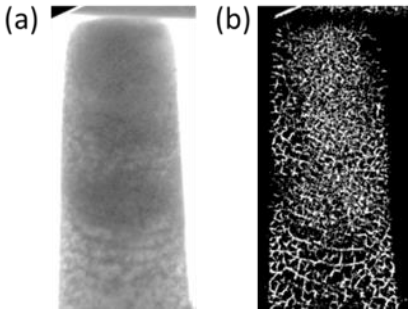

Figure 7.3. *An example of the original (a) and line-detection-program-processed image (b).*

Fig. 7.4 show the evolution of line pixel density distribution during compression for a nanopillar of 512 nm in diameter and [647] orientation. Multiple soliton-like waves of dislocations propagate within the nanopillar. The high density area within the density wave is caused by dislocation entanglement and interactions. To obtain quantitative information of soliton-like dislocation wave, the intensity profile of wave is fitted to a Gaussian function. As the density wave propagates, the width kept reducing.

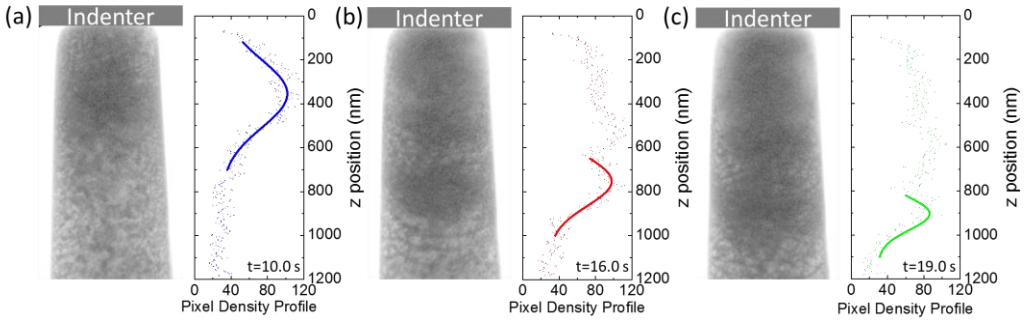

Figure 7.4. *Dislocation-pixel density detection and dislocation flow in HEA nanopillar. a-c) The profiles of line pixel density distribution at 10.0 s, 16.0 s, and 19.0 s is shown in dots. Gaussian function is used to fit the first density wave. The fitted curve is shown in solid lines.*

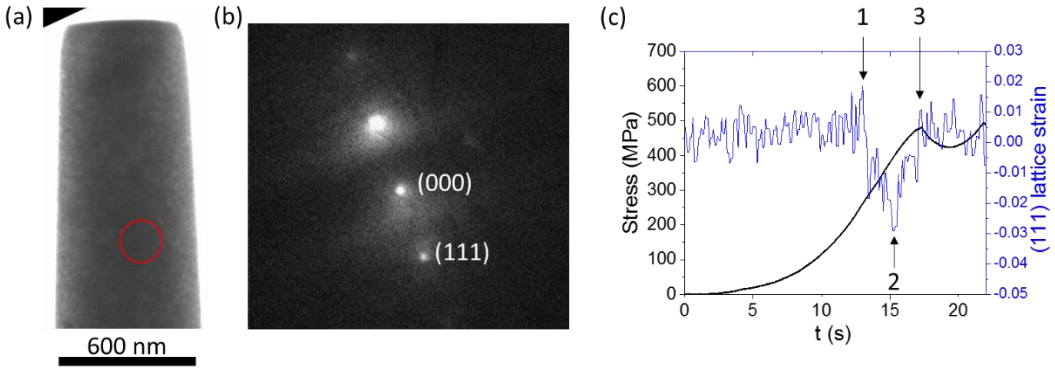

Figure 7.5. *In situ nanobeam diffraction experiment reveals the evolution of lattice strain. a) the bright field image of a 597 nm diameter and [647]-oriented nanopillar. The red circle represents*

(Fig. 7.5 cont.) the electron probe position on nanopillar. b) an example of nanobeam diffraction pattern. The spacing between (000) center spot and (111) diffraction spot are measured to determine the (111) lattice strain. c) The lattice strain and stress vs time curve.

The entanglement of dislocations results in strain localization within nanopillars. To obtain a quantitative knowledge of strain localization, in situ nanobeam diffraction patterns were recorded during compression of a 597 nm diameter and [647]-oriented nanopillar. The electron probe size is ~170 nm in diameter and placed in the middle of the nanopillar (red circle in Fig. 7.5(a)). The center positions of center spot and (111) diffraction spot are tracked by Gaussian curve fitting. The lattice strain is calculated by the change in the spacing between center and (111) diffraction spots. The lattice strain ϵ can be calculated by $\epsilon = \frac{d_{hkl} - d_0}{d_0}$ where the lattice spacing *d* can be obtained using $d = \frac{\lambda l}{r}$, λ is wavelength of incident electron beam, *l* is the camera length and *r* is the distance between the central spot and the diffraction spot. By tracking *r*, the lattice strain along certain (hkl) crystallographic direction thus can be monitored.

By continuously probing a volume of ~170 nm in diameter, the local lattice strain can be traced. The result is shown in Fig. 7.5(c) with the stress-time curve. Strong correlation between stress-time and lattice strain can be observed. Initially, the lattice strain maintains the same. After point 1 (see Fig. 7.5(c)), the compressive stress increases and there is a slope change in the stress-time curve. This is a result from the formation of 1st soliton-like dislocation wave creating a high-strained area. When the first stress drop occurred at point 3, the compressive strain is completely released by crystal slip. The detected sudden increase or decrease of lattice strain is a direct result

of dislocation wave traveling along the nanopillar, which modifies the spatial distribution of lattice strain as the deformation progresses.

7.4. Conclusion

In this chapter, we report direct observations of dislocation flow in slowly-compressed high-entropy alloy (HEA) nanopillars using in situ transmission electron microscopy (TEM). Further, we correlated the flow with the measured stress-strain curve. Surprisingly, multiple soliton-like waves of dislocations are observed during nanopillar compression. The waves propagate initially smoothly with rise and falls in the wave width, followed by intermittent jumps. We show that the waves were formed by activation/deactivation of Frank-Read dislocation sources. The propagation of dislocation waves is accompanied by intermittent bursts of dislocation activities over a large area of the nanopillars.

7.5. References

[1] M.D. Uchic, D.M. Dimiduk, J.N. Florando, W.D. Nix, Sample dimensions influence strength and crystal plasticity, Science 305(5686) (2004) 986-989.

[2] J.R. Greer, W.C. Oliver, W.D. Nix, Size dependence of mechanical properties of gold at the micron scale in the absence of strain gradients, Acta Mater 53(6) (2005) 1821-1830.

[3] D.M. Dimiduk, C. Woodward, R. LeSar, M.D. Uchic, Scale-free intermittent flow in crystal plasticity, Science 312(5777) (2006) 1188-1190.

[4] J.T. Uhl, S. Pathak, D. Schorlemmer, X. Liu, R. Swindeman, B.A.W. Brinkman, M. LeBlanc, G. Tsekenis, N. Friedman, R. Behringer, D. Denisov, P. Schall, X.J. Gu, W.J. Wright, T. Hufnagel, A. Jennings, J.R. Greer, P.K. Liaw, T. Becker, G. Dresen, K.A. Dahmen, Universal Quake Statistics: From Compressed Nanocrystals to Earthquakes, Scientific Reports 5 (2015).

[5] M.C. Miguel, A. Vespignani, S. Zapperi, J. Weiss, J.R. Grasso, Intermittent dislocation flow in viscoplastic deformation, Nature 410(6829) (2001) 667-671.

[6] B. Devincre, T. Hoc, L. Kubin, Dislocation mean free paths and strain hardening of crystals, Science 320(5884) (2008) 1745-1748.

[7] K.A. Dahmen, Y. Ben-Zion, J.T. Uhl, A simple analytic theory for the statistics of avalanches in sheared granular materials, Nat Phys 7(7) (2011) 554-557.

[8] T. Richeton, J. Weiss, F. Louchet, Breakdown of avalanche critical behaviour in polycrystalline plasticity, Nat Mater 4(6) (2005) 465-469.

[9] S. Papanikolaou, D.M. Dimiduk, W. Choi, J.P. Sethna, M.D. Uchic, C.F. Woodward, S. Zapperi, Quasi-periodic events in crystal plasticity and the self-organized avalanche oscillator, Nature 490(7421) (2012) 517-+.

[10] J. Weiss, D. Marsan, Three-dimensional mapping of dislocation avalanches: Clustering and space/time coupling, Science 299(5603) (2003) 89-92.

[11] J. Antonaglia, X. Xie, G. Schwarz, M. Wraith, J.W. Qiao, Y. Zhang, P.K. Liaw, J.T. Uhl, K.A. Dahmen, Tuned Critical Avalanche Scaling in Bulk Metallic Glasses, Sci Rep-Uk 4 (2014).

[12] R. Carroll, C. Lee, C.W. Tsai, J.W. Yeh, J. Antonaglia, B.A.W. Brinkman, M. LeBlanc, X. Xie, S.Y. Chen, P.K. Liaw, K.A. Dahmen, Experiments and Model for Serration Statistics in Low-Entropy, Medium-Entropy, and High-Entropy Alloys, Sci Rep-Uk 5 (2015).

[13] F.F. Csikor, C. Motz, D. Weygand, M. Zaiser, S. Zapperi, Dislocation avalanches, strain bursts, and the problem of plastic forming at the micrometer scale, Science 318(5848) (2007) 251-254.

[14] N. Friedman, A.T. Jennings, G. Tsekenis, J.Y. Kim, M.L. Tao, J.T. Uhl, J.R. Greer, K.A. Dahmen, Statistics of Dislocation Slip Avalanches in Nanosized Single Crystals Show Tuned Critical Behavior Predicted by a Simple Mean Field Model, Phys Rev Lett 109(9) (2012).

[15] P.B. Hirsch, R.W. Horne, M.J. Whelan, Direct observations of the arrangement and motion of dislocations in aluminium, Philos Mag 86(29-31) (2006) 4553-4572.

[16] W. Bollmann, Interference Effects in the Electron Microscopy of Thin Crystal Foils, Phys Rev 103(5) (1956) 1588-1589.

[17] P.B. Hirsch, A. Howie, M.J. Whelan, A Kinematical Theory of Diffraction Contrast of Electron Transmission Microscope Images of Dislocations and Other Defects, Philos Tr R Soc S-A 252(1017) (1960) 499-&.

[18] J.M. Zuo, J.C.H. Spence, Imaging and Characterization of Crystal Defects, Advanced Transmission Electron Microscopy: Imaging and Diffraction in Nanoscience, Springer New York, New York, NY, 2017, pp. 501-552.

[19] J. Kacher, B.P. Eftink, B. Cui, I.M. Robertson, Dislocation interactions with grain boundaries, Curr. Opin. Solid State Mat. Sci. 18(4) (2014) 227-243.

[20] I.M. Robertson, C.A. Schuh, J.S. Vetrano, N.D. Browning, D.P. Field, D.J. Jensen, M.K. Miller, I. Baker, D.C. Dunand, R. Dunin-Borkowski, B. Kabius, T. Kelly, S. Lozano-Perez, A. Misra, G.S. Rohrer, A.D. Rollett, M.L. Taheri, G.B. Thompson, M. Uchic, X.L. Wang, G. Was, Towards an integrated materials characterization toolbox, J. Mater. Res. 26(11) (2011) 1341-1383.

[21] Z. Shan, R.K. Mishra, S.S. Asif, O.L. Warren, A.M. Minor, Mechanical annealing and source-limited deformation in submicrometre-diameter Ni crystals, Nat Mater 7(2) (2008) 115-119.

[22] D. Kiener, P. Hosemann, S. Maloy, A. Minor, In situ nanocompression testing of irradiated copper, Nat Mater 10(8) (2011) 608-613.

[23] D. Kiener, P. Hosemann, S.A. Maloy, A.M. Minor, In situ nanocompression testing of irradiated copper, Nat Mater 10(8) (2011) 608-613.

[24] J.W. Yeh, S.K. Chen, S.J. Lin, J.Y. Gan, T.S. Chin, T.T. Shun, C.H. Tsau, S.Y. Chang, Nanostructured high-entropy alloys with multiple principal elements: Novel alloy design concepts and outcomes, Adv Eng Mater 6(5) (2004) 299-303.

[25] B. Cantor, I.T.H. Chang, P. Knight, A.J.B. Vincent, Microstructural development in equiatomic multicomponent alloys, Mat Sci Eng a-Struct 375 (2004) 213-218.

[26] Z. Li, K.G. Pradeep, Y. Deng, D. Raabe, C.C. Tasan, Metastable high-entropy dual-phase alloys overcome the strength–ductility trade-off, Nature advance online publication (2016).

[27] B. Gludovatz, A. Hohenwarter, D. Catoor, E.H. Chang, E.P. George, R.O. Ritchie, A fracture-resistant high-entropy alloy for cryogenic applications, Science 345(6201) (2014) 1153-1158.

[28] M.A. Hemphill, T. Yuan, G.Y. Wang, J.W. Yeh, C.W. Tsai, A. Chuang, P.K. Liaw, Fatigue behavior of Al0.5CoCrCuFeNi high entropy alloys, Acta Mater 60(16) (2012) 5723-5734.

[29] J. Antonaglia, X. Xie, Z. Tang, C.W. Tsai, J.W. Qiao, Y. Zhang, M.O. Laktionova, E.D. Tabachnikova, J.W. Yeh, O.N. Senkov, M.C. Gao, J.T. Uhl, P.K. Liaw, K.A. Dahmen, Temperature Effects on Deformation and Serration Behavior of High-Entropy Alloys (HEAs), Jom 66(10) (2014) 2002-2008.

[30] R. Carroll, C. Lee, C.-W. Tsai, J.-W. Yeh, J. Antonaglia, B.A.W. Brinkman, M. LeBlanc, X. Xie, S. Chen, P.K. Liaw, K.A. Dahmen, Experiments and Model for Serration Statistics in Low-Entropy, Medium-Entropy, and High-Entropy Alloys, Scientific Reports 5 (2015) 16997.

[31] Y. Zhang, T.T. Zuo, Z. Tang, M.C. Gao, K.A. Dahmen, P.K. Liaw, Z.P. Lu, Microstructures and properties of high-entropy alloys, Prog Mater Sci 61 (2014) 1-93.

[32] A.M. Minor, METALLURGY Starting and stopping dislocations, Nat. Mater. 14(9) (2015) 866-867.

[33] E. Clouet, D. Caillard, N. Chaari, F. Onimus, D. Rodney, Dislocation locking versus easy glide in titanium and zirconium, Nat Mater 14(9) (2015) 931-+.

[34] M. Ovaska, L. Laurson, M.J. Alava, Quenched pinning and collective dislocation dynamics, Scientific Reports 5 (2015).

CHAPTER 8

CONCLUSIONS AND FUTURE PERSPECTIVES

8.1. Conclusions

This thesis is a systematic study of deformation and fracture mechanisms of nanocrystalline TiN thin film and high-entropy alloys (HEAs) using in situ TEM. Our study provides new insights into the relationship between macroscopic mechanical response with the microscopic defect interactions.

With the help of in situ TEM mechanical testing holders and focused ion beam sample fabrications, we have demonstrated the following:

1) We demonstrated a novel method to evaluate the fracture toughness of nanocrystalline TiN thin films and to correlate with in-situ study of fracture mechanisms. In-situ TEM bright field imaging reveals three crack propagation pathways, namely bridging, intergranular fracture and a mixed mode of transgranular and intergranular fracture. Also, grain rotation or bending and dislocation sliding contribute to the deformation of nanocrystalline TiN. By comparing the crack propagation speed, it can be concluded that bridging and GB deflection act as toughening mechanisms for nanocrystalline TiN thin films.

2) We provide direct evidence of grain rotations in the nanocrystalline TiN nanopillar under compression using electron diffraction. In-situ electron diffraction experiments were performed in a TEM. Diffraction pattern indexing and nanograin identification were helped by the technique of scanning electron nanobeam diffraction (SEND). The

diffraction experiments were further complemented by in-situ TEM imaging. Together, the experiments reported here provide insights into the mechanism of grain rotation with the help of a classical crystal rotation model.

3) The deformation mechanism of HEA nanopillar is revealed by simultaneous measurement of mechanical response and dislocation dynamics. Systematic study is conducted to find the optimal experimental condition for dislocation imaging. The plasticity of HEA is first carried by the operation of new dislocation sources. As the dislocation density continues to rise, dislocations entangle with each other during propagation and cease to move. The entangled dislocation structure collectively jumps when the stress is high enough. At last, the large crystal slip happens. This pattern repeats itself under the applied stress.

4) We obtained a scaling collapse of the slip-avalanche size distributions as function of applied stress and dislocation activities of HEAs that confirm MFT-scaling predictions and indicate that the applied stress is a critical tuning parameter. It shows that the deformation of HEAs is a tuned critical phenomenon rather than a self-organized critical one. The approximately-linear growth of the dislocation swept area with the stress drop confirms previously untested MFT predictions for spatial correlations of slip avalanches, and constitutes the first test of the spatial scaling behavior in these systems.

5) Multiple soliton-like waves of dislocations are observed during HEA nanopillar compression. The waves propagate initially smoothly with rise and falls in the wave width, followed by intermittent jumps. We show that the waves were formed by activation/deactivation of Frank-Read dislocation sources. The propagation of dislocation waves is accompanied by intermittent bursts of dislocation activities over a large area of the nanopillars. Thus, the correlation study of mesoscopic mechanic testing and nm-scale dislocation imaging here provides unprecedented insights into the less observable dislocation processes during the quiescent periods between large avalanches and collective dislocation dynamics.

Thus, our results in the study of nanocrystalline ceramics and alloys show that the correlation study between electron imaging and diffraction with mechanical testing provides informative results on revealing the deformation and fracture mechanisms, especially at high spatial resolution exceeding other available techniques.

8.2. Future Perspectives

In situ TEM deformation study of BCC or dual-phase high-entropy alloys

In our study, it is shown that in situ TEM nanopillar compression can provides detailed dislocation dynamics and reflects bulk-like mechanical behaviors. Our study is focused on FCC-phase HEAs which have good ductility but relatively low yield strength. Reports[1] have shown that BCC phase

HEAs processes high strength, but limited ductility. Understanding the fracture mechanisms would help to solve this problem. Further, there have been extensive research efforts to combine the advantage of both phases by forming dual-phase HEAs to break the tradeoff between strength and ductility. Recent report on CoCrFeNiMn HEA[2] showed that by forming a HCP-FCC dual-phase HEAs, the ductility and strength can be improved simultaneously. In situ TEM deformation study brings promising opportunity in revealing the underlying mechanisms, such as dislocation-grain boundary interactions, and guiding material design.

In situ TEM compression of ferroelectric materials

Ferroelectric materials have drawn significant interest for their applications including microelectromechanical systems (MEMS), sensors and nanogenerator[3, 4]. Under electric field or stress, local polarization transformed to same preferred orientation and such uniform polarizations form ferroelectric domains. Understanding the mechanism of ferroelectric domain switching under compression is of crucial importance for optimizing the performance of ferroelectric devices. Our preliminary study on $BaTiO_3$ single crystal using in situ TEM nanopillar compression testing showed clear domain switching, which can be well-correlated with the stress-strain deformation curve. The leaf-like 90-degree domains nucleate and expand with increasing stress. Observing the domain-switching under stress could thus provide critical insights in revealing the domain switching mechanisms.

8.3. References

[1] Kao Y-F, Chen T-J, Chen S-K, Yeh J-W. Microstructure and mechanical property of as-cast, -homogenized, and -deformed AlxCoCrFeNi ($0 \leq x \leq 2$) high-entropy alloys. Journal of Alloys and Compounds 2009;488:57-64.

[2] Li Z, Pradeep KG, Deng Y, Raabe D, Tasan CC. Metastable high-entropy dual-phase alloys overcome the strength–ductility trade-off. Nature 2016;534:227-30.

[3] Biernacki J, Juhasz J, Sadler G. Application of Enhanced Modern Structured Analysis Techniques to Space Station Freedom Electric-Power System Requirements. Proceedings of the 26th Intersociety Energy Conversion Engineering Conference, Vols 1-6 1991:B44-B9.

[4] Wang XD, Song JH, Liu J, Wang ZL. Direct-current nanogenerator driven by ultrasonic waves. Science 2007;316:102-5.